SD 68-442

MISSION EVALUATION 101
PRESIMULATION REPORT
Part II
Simulator Description

June 1968

Contract NAS9-150, SA 300, Exhibit I, Paragraph 5.1.1.2

SPACE DIVISION
NORTH AMERICAN ROCKWELL CORPORATION

ENC 3

SD 68-442

MISSION EVALUATION 101
PRESIMULATION REPORT
Part II
Simulator Description

June 1968

Contract NAS9-150, SA 300, Exhibit I, Paragraph 5. 1. 1. 2

SPACE DIVISION
NORTH AMERICAN ROCKWELL CORPORATION

CONTENTS

Section Page

ILLUSTRATIONS

TABLES

1.0 INTRODUCTION

1.1 SIMULATION FACILITY

A layout diagram of the Flight Simulation Laboratory at the Space Division of North American Rockwell Corporation, Downey, California, is presented in Figure 1-1. Photographs of various simulation hardware and computation facilities are shown in Figures 1-2 through 1-5.

1.2 SIMULATION CONFIGURATION

The simulation configuration described in this document consists of five major portions the analog and digital computation facilities, the SCS and GNCS prototype hardware, an instrumented command module mockup, external visual display mechanisms, and special purpose electronic interfacing apparatus. Each area is defined in detail in the following sections.

For easy reference, a total simulation flow diagram is presented in Figure 1-6. The sections labeled 2 through 8 correspond to the sectional breakdown of the document, and the numbers in the boxes correspond to the numbering of the paragraphs within the sections.

1.3 OBJECTIVES AND CONTENTS

This document describes in detail all analytical models of those spacecraft systems for which prototype hardware was not available or whose use was not feasible. It expresses the analytical models used to represent all real world phenomena affecting spacecraft dynamic motion and spacecraft instrumentation.

Some spacecraft hardware operations were duplicated by special purpose electronic equipment specifically designed and constructed for simulation use. Exhaustive checkout has shown this equipment to respond identically to the specifications of the actual hardware; therefore, detailed descriptions are not considered necessary. This substitution includes SCS moding logic circuitry, reaction jet priority switching, and various discretes logic, as well as the program analyzer console (PAC), a taped program for duplicating the operation of the CMC memory that is primarily hard wired in the actual spacecraft hardware. In cases where this substitution occurs, reference will be made to those specification documents upon which the design of the special purpose articles was based.

The actual prototype hardware incorporated in these simulation studies will be identified only. Further discussion of the hardware mentioned herein is not considered necessary.

This document does not include information concerning derivations of analytical models, descriptions and data pertaining to specific missions, study objectives, schedules, and run descriptions, or flight analysis of any kind.

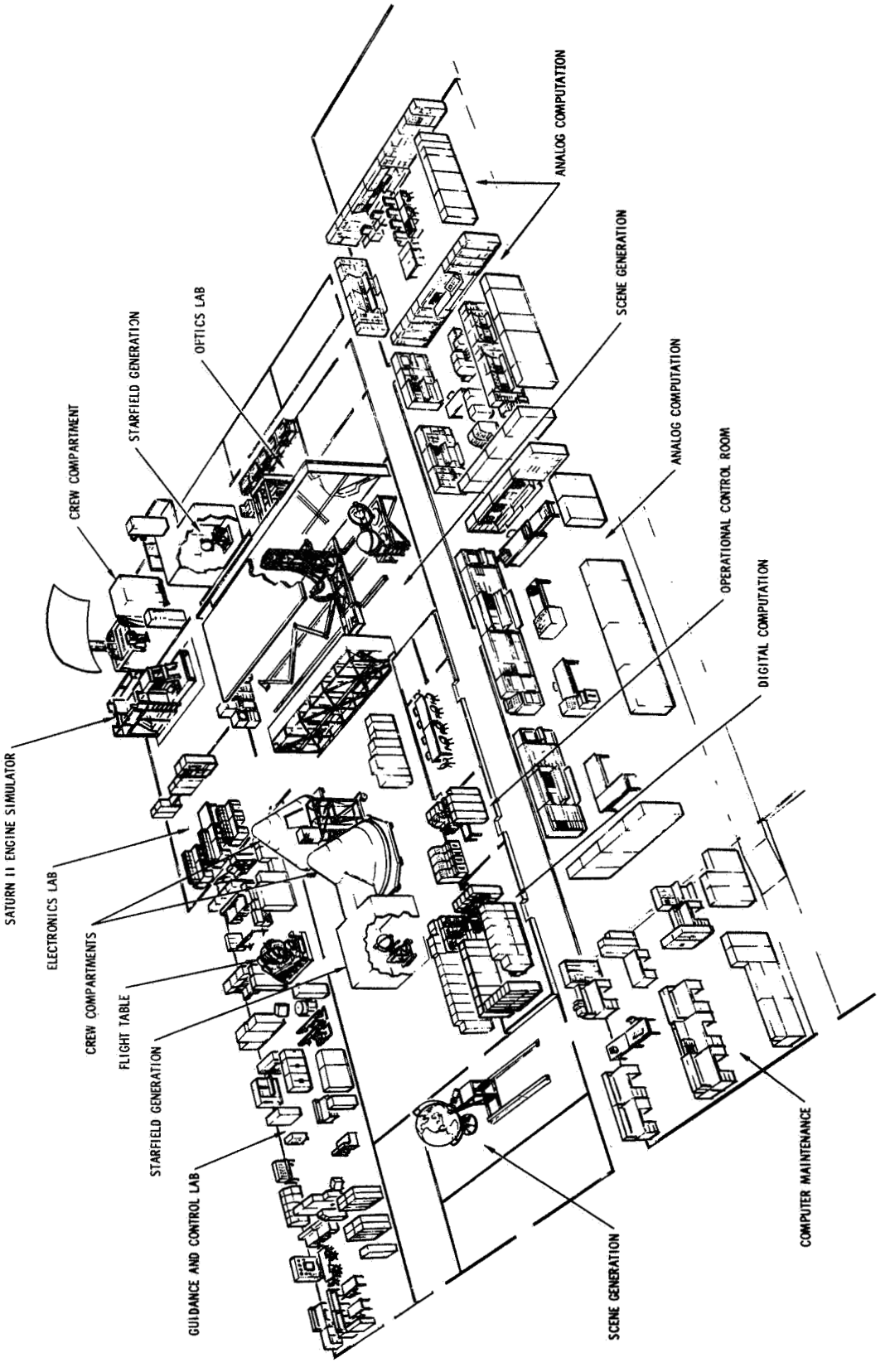

Figure 1-1. Flight Simulation Laboratory

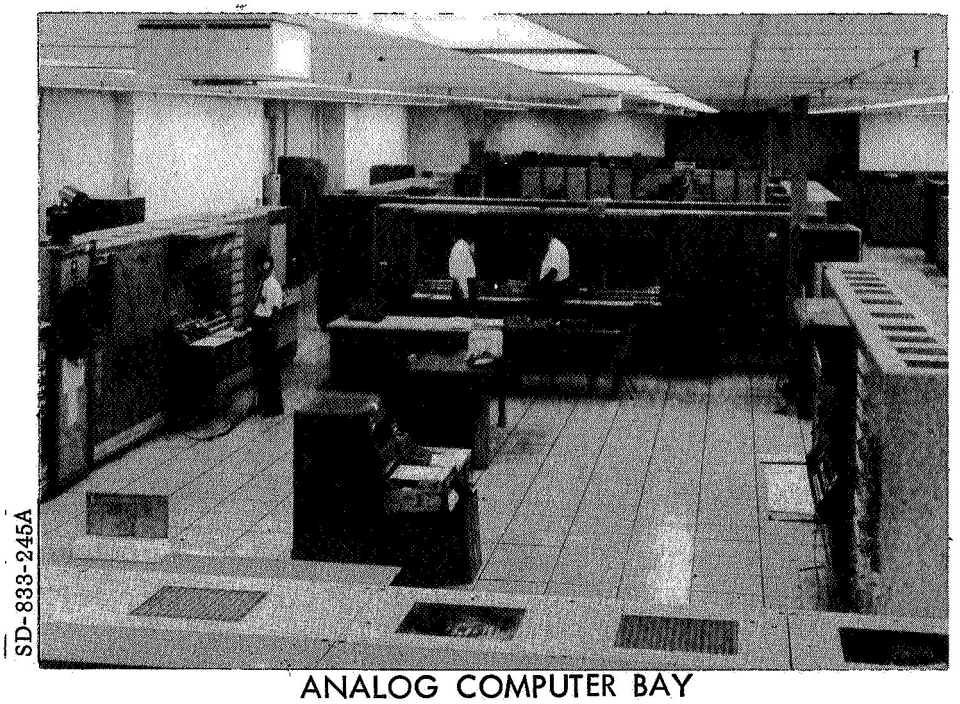

SD-833-245A

ANALOG COMPUTER BAY

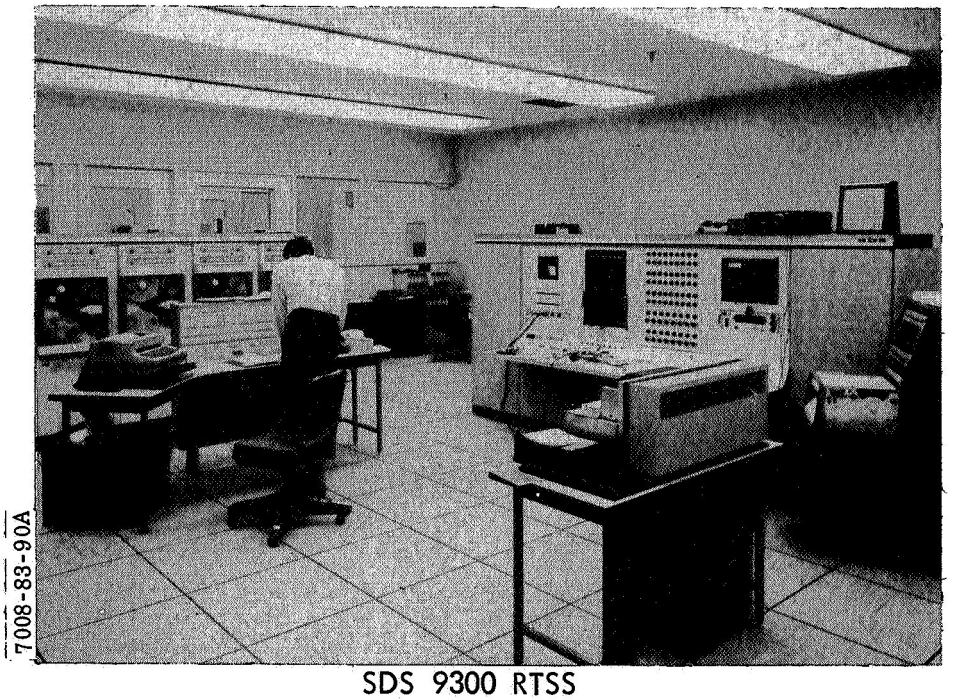

7008-88-90A

SDS 9300 RTSS

Figure 1-2. Computation Facility

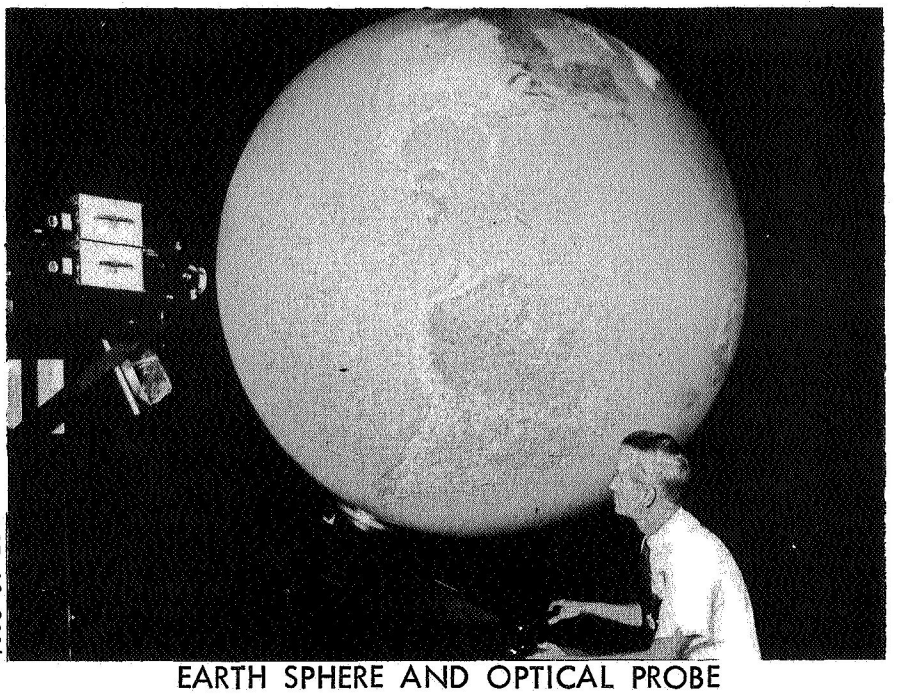

7008-60-13B

EARTH SPHERE AND OPTICAL PROBE

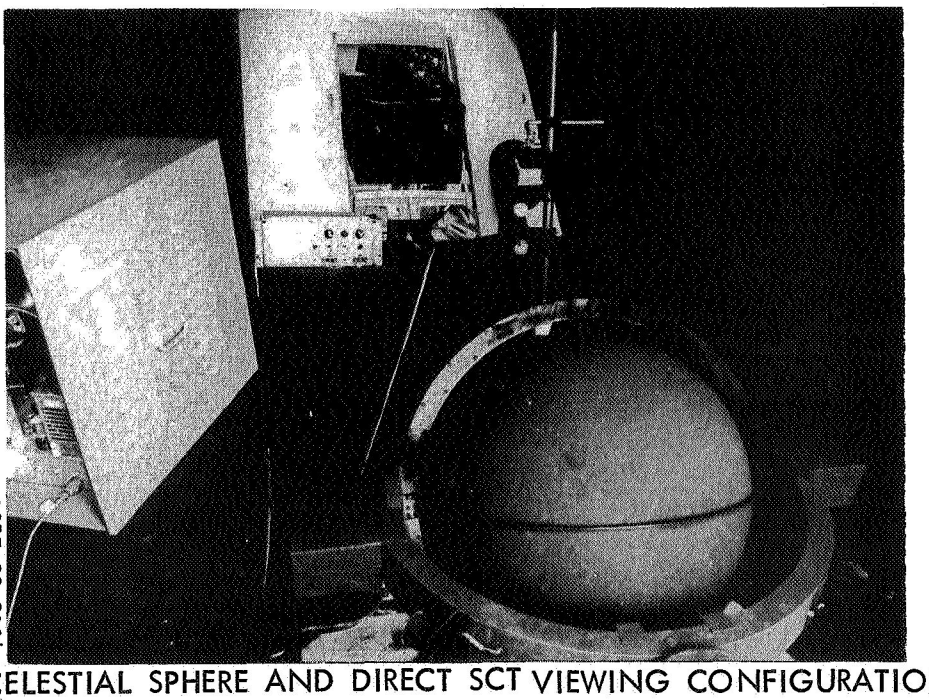

7008-83-143C

CELESTIAL SPHERE AND DIRECT SCT VIEWING CONFIGURATION

Figure 1-3. External Visual Display Mechanisms

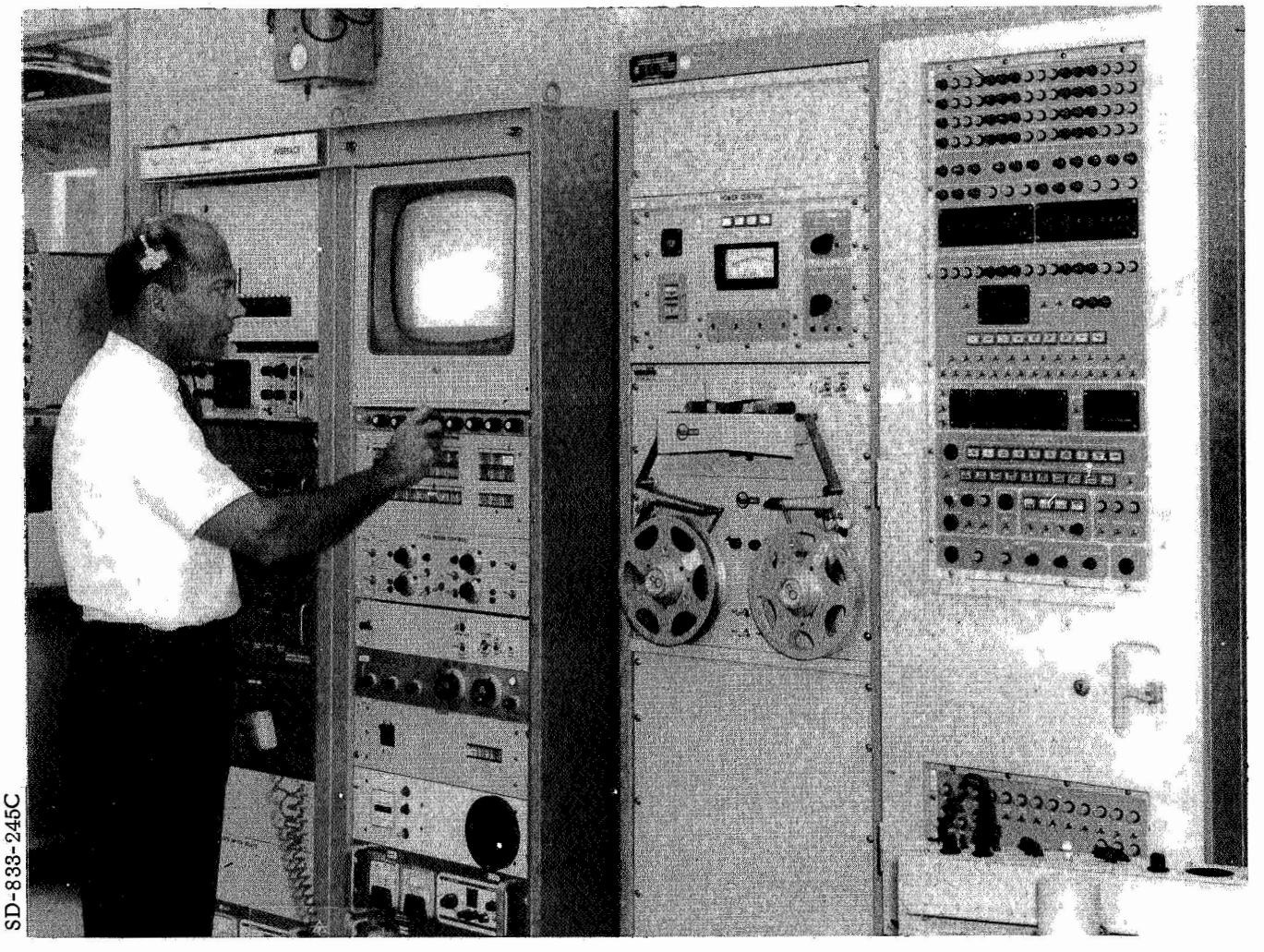

Figure 1-4. Interface Electronics

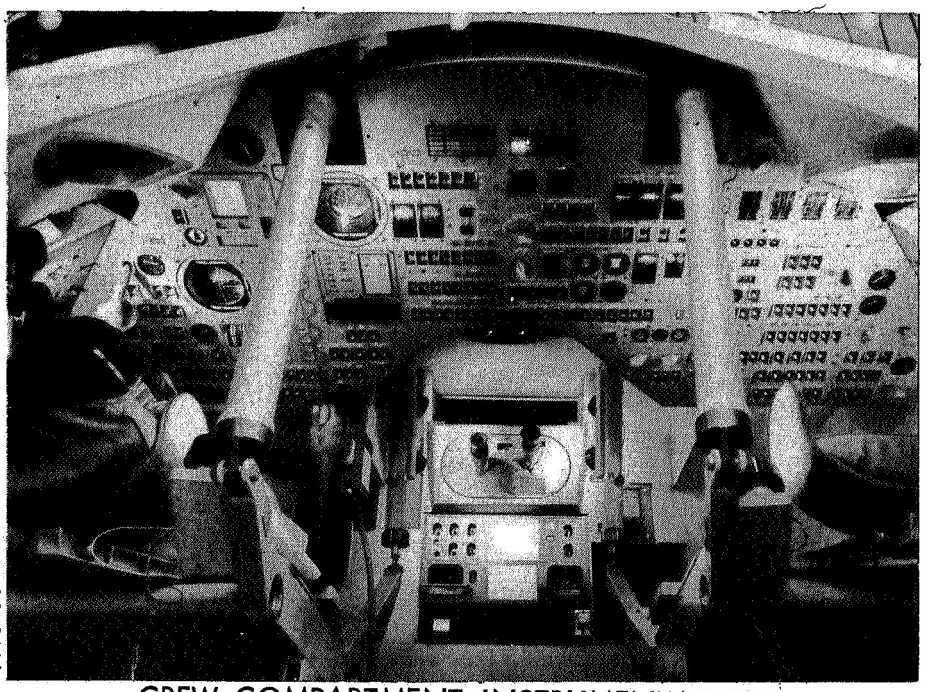

7008-83-403

CREW COMPARTMENT INSTRUMENTATION

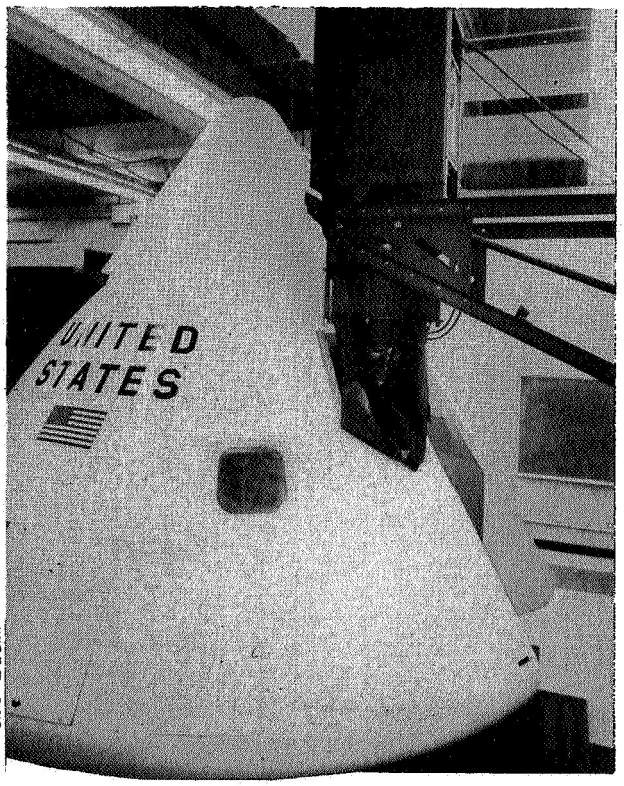

SD-833-245H

EVALUATOR EXTERIOR WITH EXTERNAL OPTICAL DISPLAY DEVICE MOUNTED OVER LEFT RENDEZVOUS WINDOW

Figure 1-5. Command Module Evaluator

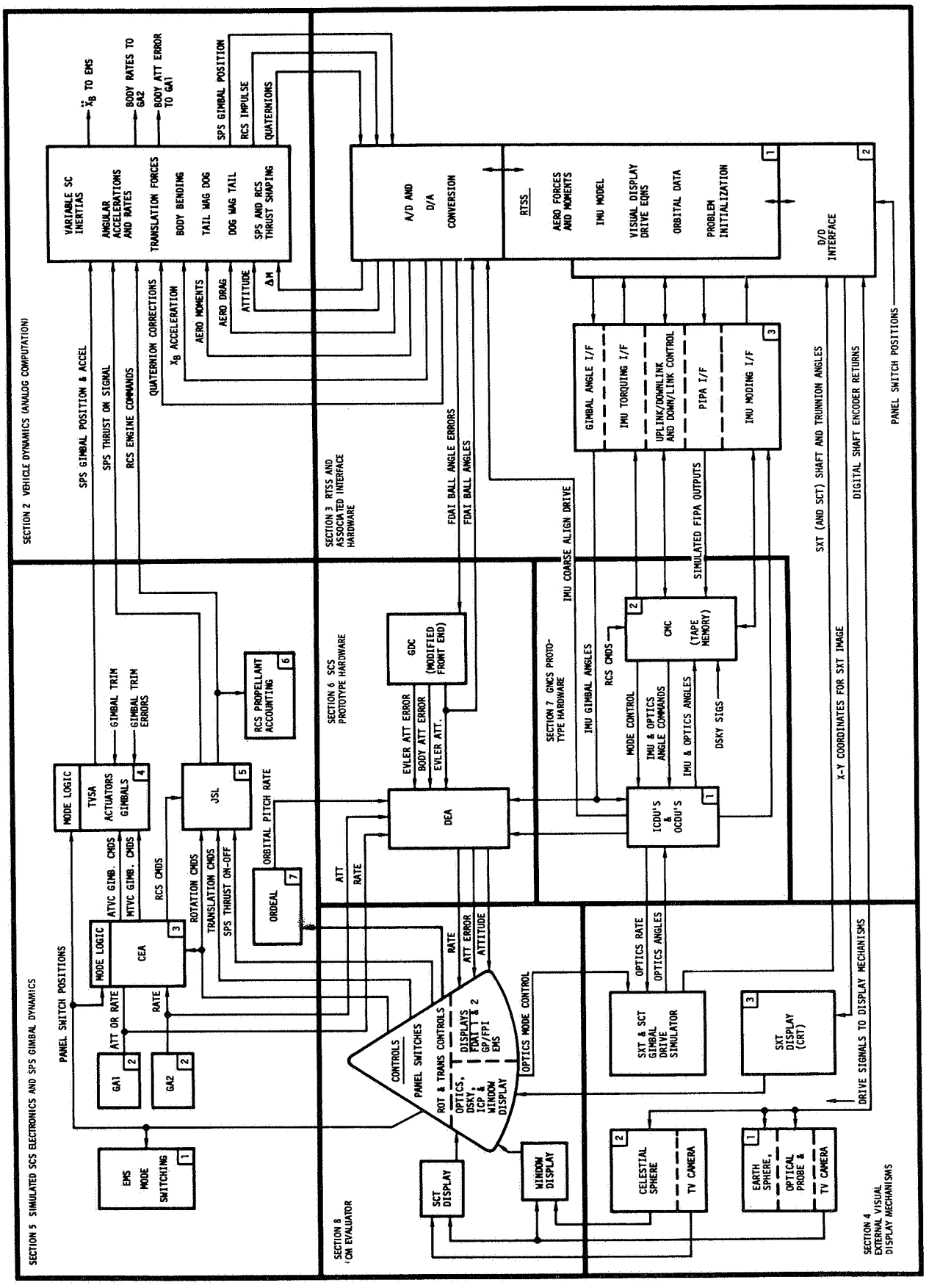

Figure 1-6. Simulation Configuration Flow Diagram

2.0 VEHICLE DYNAMICS (ANALOG COMPUTATION)

This section presents all equations of motion requiring analog computation. Included are those functions which tend to vary rapidly or which require only approximate solution. Analog-to-digital and digital-to-analog conversion is not always indicated because it is generally understood that such conversion must take place between the analog and digital computers. The analog-to-digital converters are made by Scientific Data Systems and convert analog signals ranging from -100 volts to +100 volts into 13-bit parallel words.

The analog computation employs the following computing hardware:

500	Operational amplifiers (EAI 231R's)
59	Multipliers
3	Resolvers
20	Diode function generators
1	30- by 30-inch X-Y plotter
8	8-channel strip chart recorders (time synchronized)

Refer to Figure 2-1 for a breakdown of analog computation by computer section. Figure 2-2 shows the interrelationship of the various computations performed on the analog computers; the numbers in the blocks refer to paragraphs in this section which describe in detail those computations. A complete list of constants is contained in Table 2-1, and all variables are listed in Table 2-2.

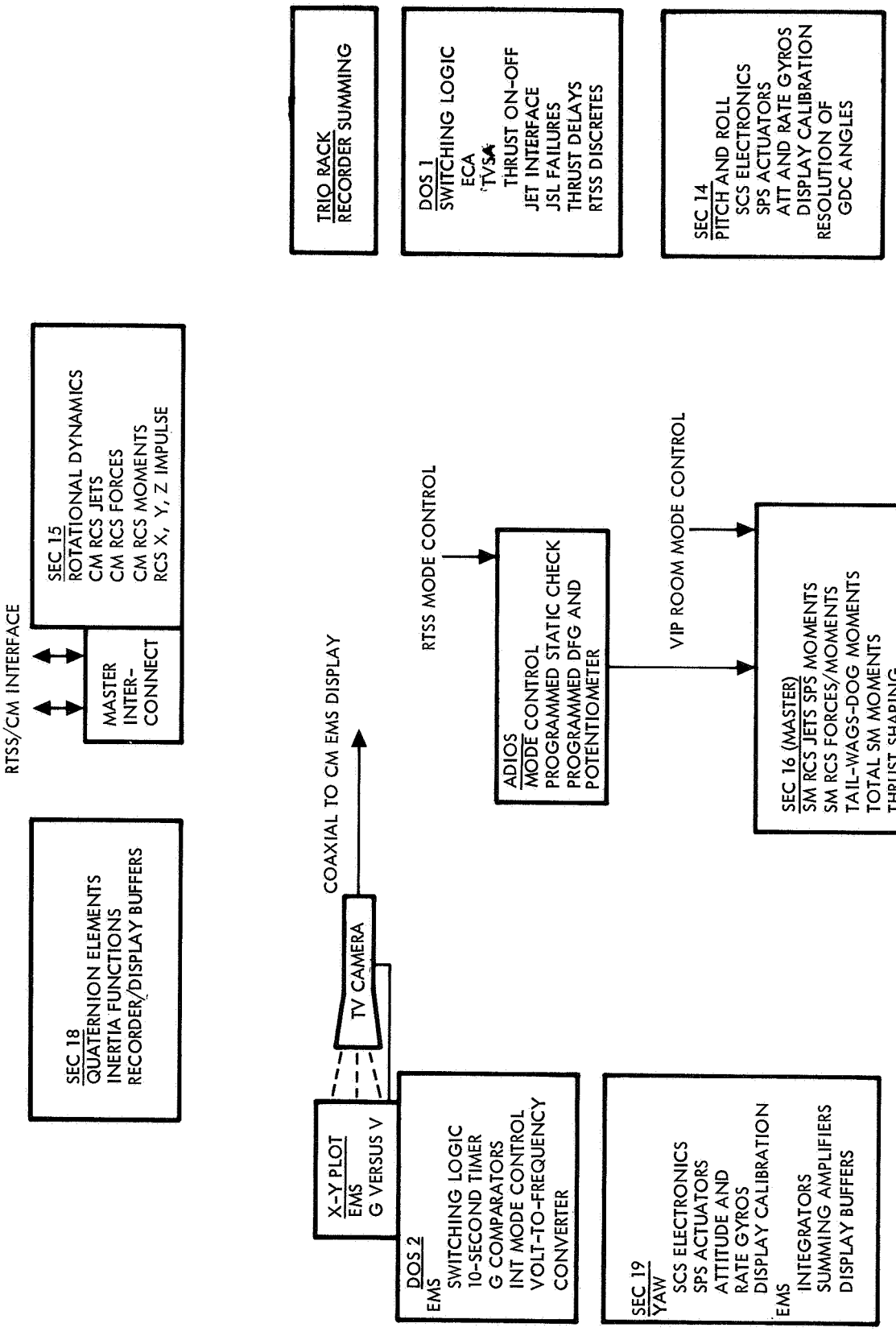

Figure 2-1. Analog Complex—Apollo ME101

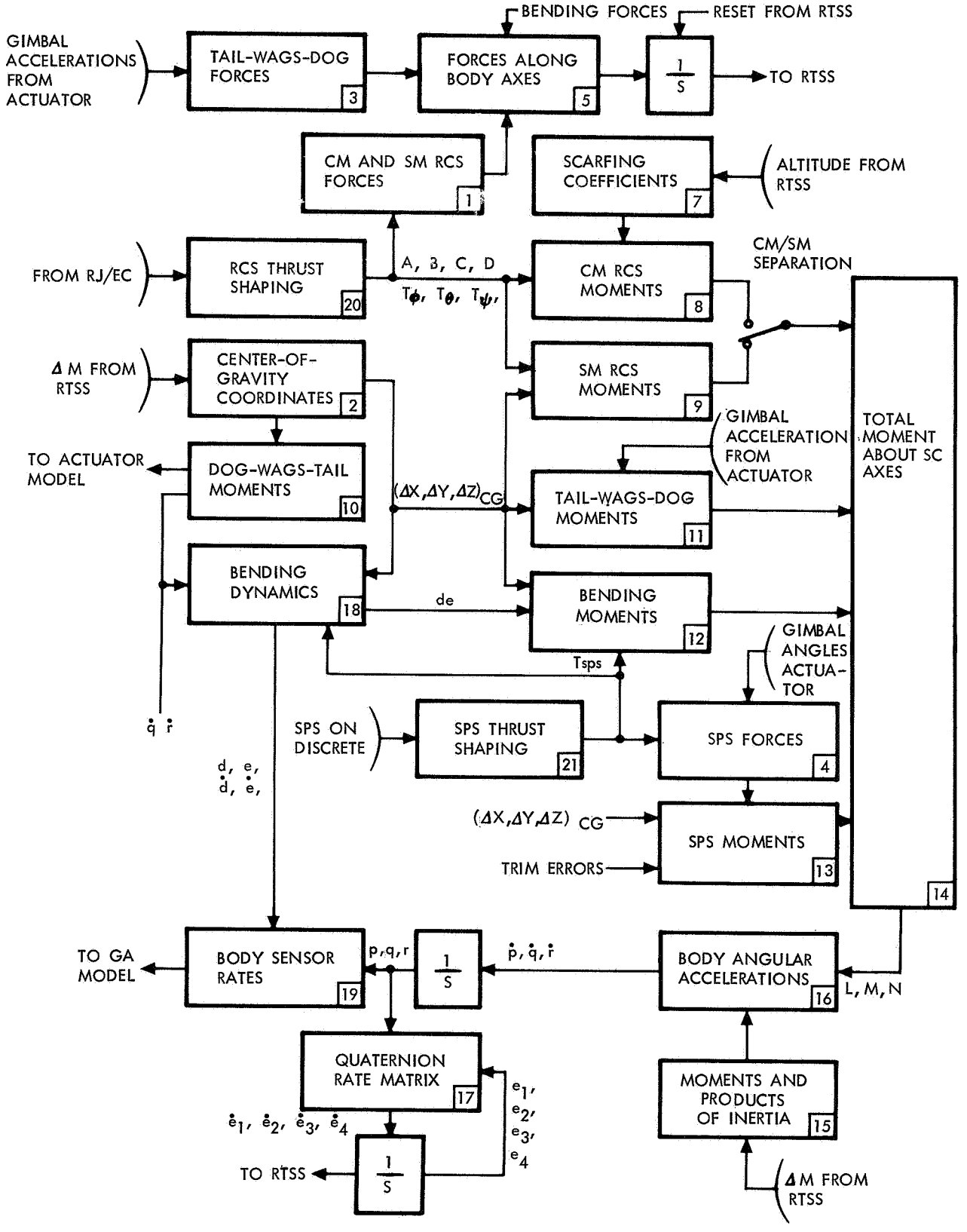

Figure 2-2. Flow Diagram of Analog Computation of Vehicle Dynamics

Table 2-1. Mathematical Model Constants

Symbol	Magnitude	Units	Description
D_j	0 005	ND	Damping of the j-th free-free mode
M_j	1 0	lb-sec^2/in.	Generalized mass for the j-th mode
m_e	27 8	slugs	SPS engine mass
$I_{e\theta}$, $I_{e\psi}$	304. 0, 313 0	slug-ft^2	SPS engine pitch, yaw moments of inertia
$(\ell_\theta, \ell_\psi)_e$	0. 342, 0 200	ft	Pitch, yaw distance from engine gimbal point to engine center of gravity
ℓ_g	10.56	ft	Distance between gimbal point and X_{REF}
$(\Delta X, Y, Z)_{CG}$	1040. 8, -0. 4, 6. 8	inches	Command module center of gravity
X_{REF}	959 9	inches	Reference X center of gravity
I_{XX}, I_{YY}, I_{ZZ}	5599, 5067, 4707	slug-ft^2	Command module moments of inertia
I_{XY}, I_{XZ}, I_{YZ}	0, 0, 0	slug-ft^2	Command module products of inertia
$K_1 \rightarrow K_7$	See Table 2-3	ND	Service module RCS force coefficients
$K_8 \rightarrow K_{27}$	See Table 2-3	ft	Service module RCS moment coefficients
$K28 \rightarrow K_{63}$	See Table 2-3	ND	Command module RCS force coefficients
C_{iA} $i = 1 \rightarrow 36$	See Table 2-3	ft	Command module RCS jet scarfing moment coefficients
C_i $i = 1 \rightarrow 36$	See Table 2-3	ft	Command module RCS jet moment coefficients
$(A, B, C, D)_1$	100	lb	Service module jet 1 of Quads A, B, C, and D
$(A, B, C, D)_2$	100	lb	Service module jet 2 of Quads A, B, C, and D
$(A, B, C, D)_3$	100	lb	Service module jet 3 of Quads A, B, C, and D
$(A, B, C, D)_4$	100	lb	Service module jet 4 of Quads A, B, C, and D
$F_1 \rightarrow F_{12}$	+1	lb	Command module RCS jet ON-signals (Figure 2-2)
$(T_\phi, T_\theta, T_\psi)_A$	+1	lb	Command module RCS System A positive roll (9), pitch (1), yaw (5) jet ON-signals
$(-T_\phi, -T_\theta, -T_\psi)_A$	-1	lb	Command module RCS System A negative roll (12), pitch (2), yaw (8) jet ON-signals
$(T_\phi, T_\theta, T_\psi)_B$	+1	lb	Command module RCS System B positive roll (11), pitch (3), yaw (7) jet ON-signals

Table 2-1. Mathematical Model Constants (Cont)

Symbol	Magnitude	Units	Description
$(-T_\phi, -T_\theta, -T_\psi)_B$	-1	lb	Command module RCS System B negative roll (10), pitch (4), yaw (6) jet ON-signals
T_{RATED}	21,900	lb	Maximum rated SPS engine thrust
D_{10}	0.6	ND	SPS thrust-on damping ratio
ω_{10}	35.68	rad/sec	SPS thrust-on natural frequency
ω_{11}	28.54	rad/sec	SPS thrust-on shaping angular rate
ψ	0.926	rad	SPS thrust-on shaping phase angle
K_1	9.7	sec^{-1}	SPS thrust-off shaping coefficient
K_2	2.3	sec^{-1}	SPS thrust-off (tail-off) shaping coefficient
τ_{14}	See paragraph 2.20	sec	Jet thrust-on delay
τ_{15}	See paragraph 2.20	sec	Jet thrust-off delay
τ_{16}	0.390	sec	SPS thrust-on delay
τ_{17}	0.260	sec	SPS thrust-off delay
τ_{18}	0.420	sec	SPS thrust-off shaping time constant
τ_{19}	1.60	sec	SPS thrust-off shaping time constant
$(\epsilon_\phi, \epsilon_\theta, \epsilon_\psi)_T$		rad	Roll, pitch, yaw thrust misalignments
$(L, M, N)_\epsilon$	30, 4350, 4350	ft-lb	Thrust misalignment moments about X, Y, Z body axes
K_f	8.080808/50	sec^{-1}	Quaternion error corrector gain

Table 2-2. Mathematical Model Variables

Symbol	Description	Units
$(F_X, F_Y, F_Y)_{TWD}$	Tail-wags-dog forces along body axes	lb
$(F_X, F_Y, F_Z)_T$	SPS thrust forces along body axes	lb
$(F_X, F_Y, F_Z)_{RCS}$	RCS (CM or SM) forces along body axes	lb
$(F_X, F_Y, F_Z)_{SUM}$	Summation of forces along body axes, excluding SPS force	lb
$(L, M, N)_T$	SPS thrust moments about body axes	ft-lb
$(L, M, N)_{TWD}$	Tail-wags-dog moments about body axes	ft-lb
$(L, M, N)_{BN}$	Bending moments about body axes	ft-lb
$(L, M, N)_{RCS}$	RCS (CM or SM) moments about body axes	ft-lb
$(L, M, N)_A$	Aerodynamic moments about body axes	ft-lb
L, M, N	Total moments about X, Y, Z body axes	ft-lb
p, q, r	Roll, pitch, yaw angular rates (rigid body)	sec^{-1}
$(p, q, r)_F$	Roll, pitch, yaw sensed angular rates (free-free bending)	sec^{-1}
$\dot{p}, \dot{q}, \dot{r}$	Roll, pitch, yaw angular accelerations (rigid body)	sec^{-2}
e_1, e_2, e_3, e_4	Quaternion elements	ND
h	Spacecraft altitude	ft
P_1, P_2	CM RCS jet scrafing coefficients	ND
$(Y, Z)_{CG}$	Coordinates of spacecraft center of gravity in spacecraft body frame	inches

Table 2-2. Mathematical Model Variables (Cont)

Symbol	Description	Units
ΔX_{CG}	Deviation of spacecraft center of gravity along X-axis from reference point (-959.9 inches)	inches
I_{XX}, I_{YY}, I_{ZZ}	Moments of inertia	slug-ft^2
I_{XY}, I_{XZ}, I_{YZ}	Products of inertia	slug-ft^2
d_j $j = 1, 2, 3$	Generalized displacement of j-th free-free mode	inches
ϕ_{ij}	Normalized displacement (translation) of the j-th free-free mode (i-th axis), at the engine gimbal point	ND
σ_{ij}, λ_{ij}	Normalized displacement (rotation) of the j-th free-free mode (i-th axis), at the engine gimbal point and sensor mount point, respectively	(inches)$^{-1}$
ℓ_X	X distance from engine gimbal point to spacecraft center of gravity	inches
ω_j	Natural frequency of the j-th free-free	sec^{-1}
$\delta_\theta, \delta_\psi$	Engine pitch, yaw gimbal angles	rad
$(T_P, T_Y)_{DWT}$	Dog-wags-tail pitch, yaw torque about the engine gimbal point	ft-lb
T_{SPS}	SPS engine thrust	lb
t_1	Time elapsed from CM reaction jet electrical ON-command	sec
t_2	Time elapsed from SM reaction jet electrical ON-command	sec
t_3	Time elapsed from SPS engine electrical ON-command	sec
t_4	Time elapsed from SPS engine electrical OFF-command	sec

2 1 COMMAND MODULE AND SERVICE MODULE RCS FORCES

$$\begin{Bmatrix} F_X \\ F_Y \\ F_Z \end{Bmatrix}_{CM\ RCS} = \begin{bmatrix} -K_{28} & 0 & -K_{46} \\ -K_{29} & K_{32} & K47 \\ K_{30} & K_{33} & K_{48} \end{bmatrix} \cdot \begin{Bmatrix} F_1 \\ F2 \\ F_3 \end{Bmatrix}$$

$$+ \begin{bmatrix} 0 & -K_{34} & -K_{55} \\ -K_{50} & -K_{35} & K_{56} \\ K_{51} & K_{36} & K_{57} \end{bmatrix} \cdot \begin{Bmatrix} F_4 \\ F_5 \\ F_6 \end{Bmatrix}$$

$$+ \begin{bmatrix} -K_{52} & -K_{37} & 0 \\ -K_{53} & K_{38} & K_{41} \\ -K_{54} & -K_{39} & K_{42} \end{bmatrix} \cdot \begin{Bmatrix} F_7 \\ F_8 \\ F_9 \end{Bmatrix}$$

$$+ \begin{bmatrix} 0 & 0 & 0 \\ -K_{62} & K_{59} & -K_{44} \\ K_{63} & -K_{60} & -K_{45} \end{bmatrix} \cdot \begin{Bmatrix} F_{10} \\ F_{11} \\ F_{12} \end{Bmatrix}$$

$$\begin{Bmatrix} F_X \\ F_Y \\ F_Z \end{Bmatrix}_{SM\ RCS} = \left\{ \begin{matrix} K_1 (A + B + C + D)_3 - K_1 (A + B + C + D)_1 \\ \begin{bmatrix} K_2 & -K_3 \\ K_3 & K_2 \end{bmatrix} \cdot \begin{Bmatrix} A - C \\ B - D \end{Bmatrix}_1 + \begin{bmatrix} K_2 & -K_3 \\ K_3 & K_2 \end{bmatrix} \cdot \begin{Bmatrix} A - C \\ B - D \end{Bmatrix}_3 \end{matrix} \right\} \cdot$$

$$+ \left\{ \begin{matrix} 0 \\ \begin{bmatrix} -K_4 & -K_5 \\ K_5 & -K_4 \end{bmatrix} \cdot \begin{Bmatrix} A - C \\ B - D \end{Bmatrix}_2 + \begin{bmatrix} K_6 & -K_7 \\ K_7 & K_6 \end{bmatrix} \cdot \begin{Bmatrix} A - C \\ B - D \end{Bmatrix}_4 \end{matrix} \right\}$$

where

F_i (i = 1 - 12) represents forces from each of the 12 command module jets. See Figure 2-3.

A_i, B_i, C_i, and D_i (i = 1 - 4) represent forces from each of the 16 service module jets, where A, B, C, and D represent each of four quads. See Figure 2-4.

K_i (i = 1 - 7 and 28 - 63) represents the various service module and command module RCS force coefficients. See Table 2-3.

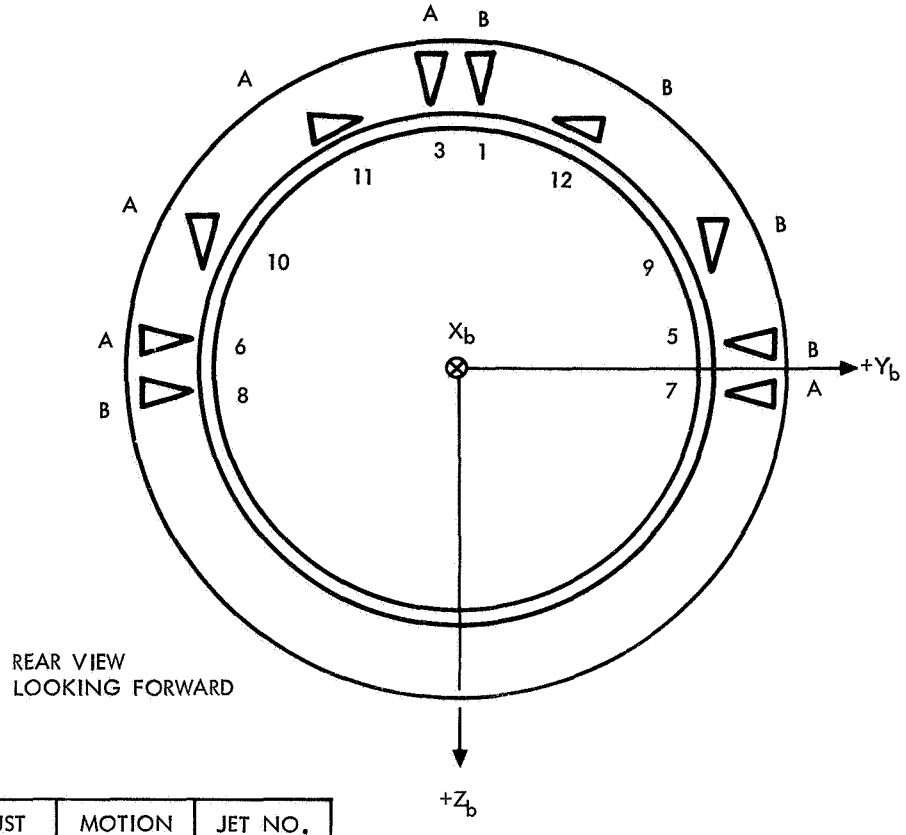

THRUST	MOTION	JET NO.
+TϕA	+ ROLL	11
-TϕA	- ROLL	10
+TθA	+ PITCH	3
-TθA	- PITCH	2
+TψA	+ YAW	7
-TψA	- YAW	6
+TϕB	+ ROLL	9
-TϕB	- ROLL	12
+TθB	+ PITCH	1
-TθB	- PITCH	4
+TψB	+ YAW	5
-TψB	- YAW	8

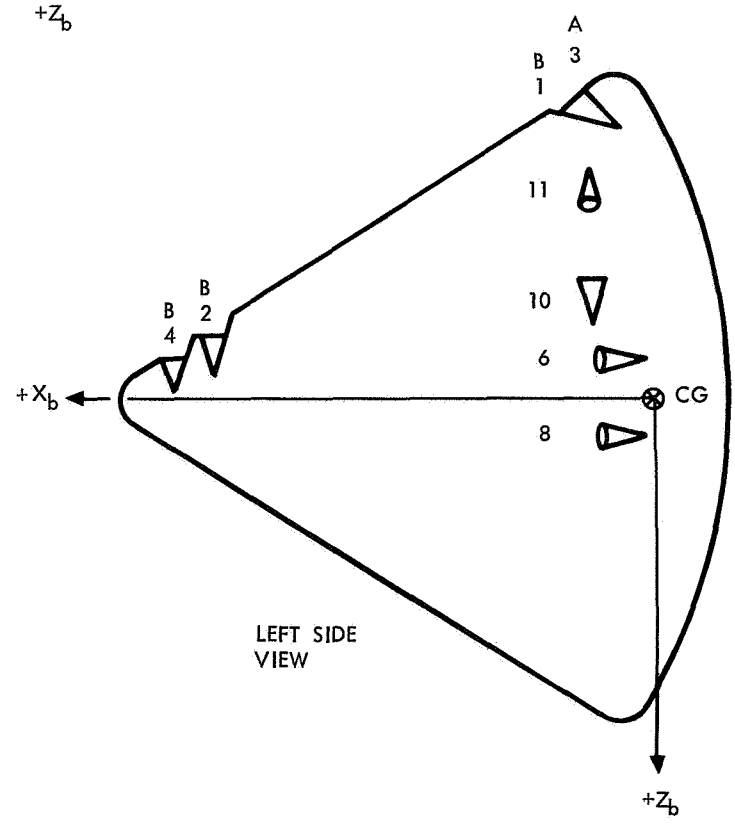

Figure 2-3. Command Module Reaction Jet Configuration, Systems A and B

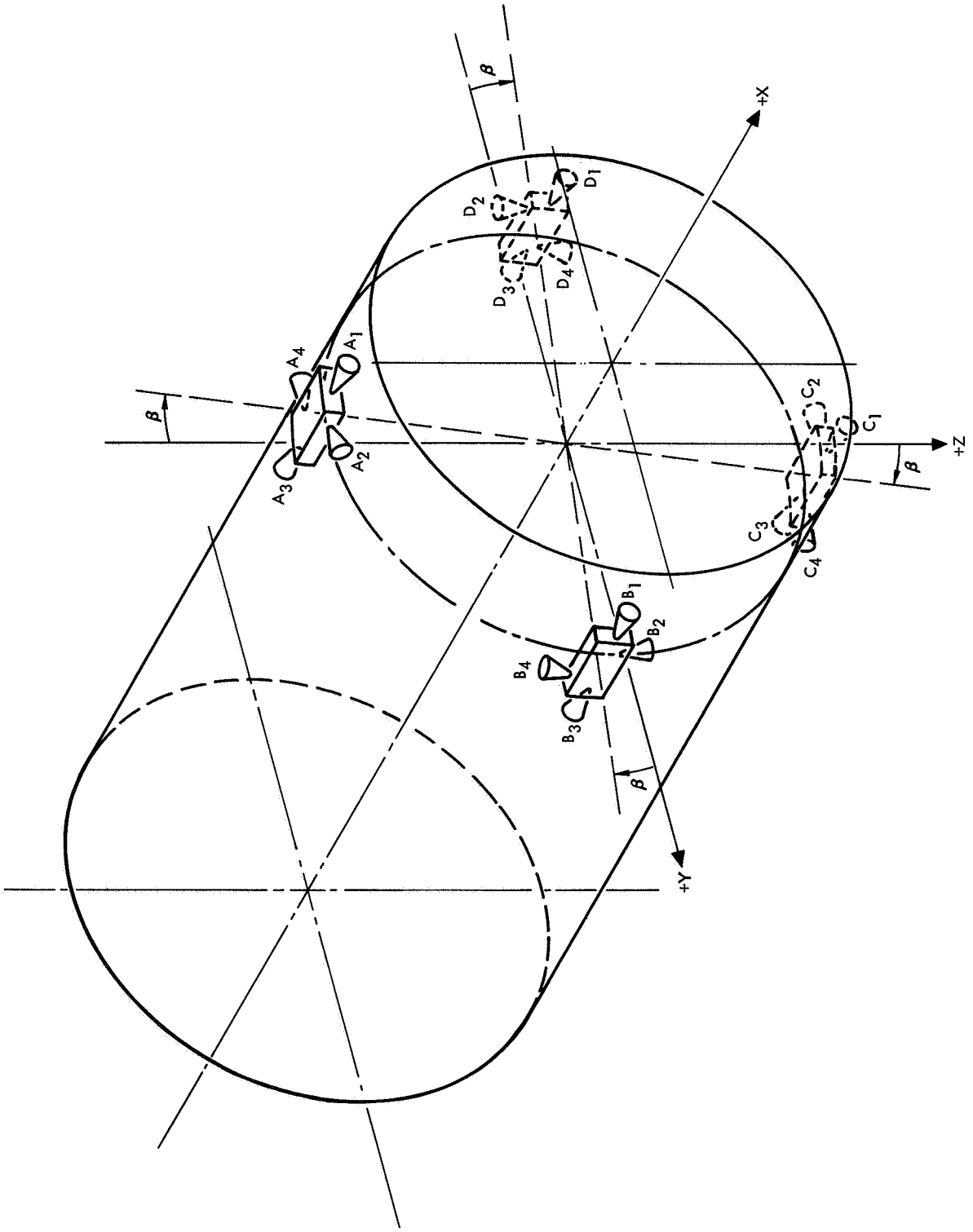

Figure 2-4. Service Module RCS Jet Designations

Table 2-3. RCS Force and Moment Coefficients

Symbol	Magnitude	Symbol	Magnitude
K_1	0.9848	K_{41}	40.0
K_2	0.0219	K_{42}	88.3
K_3	0.1723	K_{43}	0.0
K_4	0.9550	K_{44}	-93.6
K_5	0.2965	K_{45}	3.5
K_6	0.9989	K_{46}	-66.8
K_7	0.0480	K_{47}	4.1
K_8	6.8133	K_{48}	66.7
K_9	6.8133	K_{49}	0.0
K_{20}	6.72055	K_{50}	10.3
K_{21}	6.69098	K_{51}	93.0
K_{22}	0.7609	K_{52}	-67.0
K_{23}	0.7233	K_{53}	-64.8
K_{24}	0.00224	K_{54}	-4.0
K_{25}	0.00788	K_{55}	-67.0
K_{26}	0.00716	K_{56}	64.8
K_{27}	0.1640	K_{57}	4.0
K_{28}	-68.3	K_{58}	0.0
K_{29}	-4.1	K_{59}	93.6
K_{30}	66.7	K_{60}	3.5
K_{31}	0.0	K_{61}	0.0
K_{32}	-10.3	K_{62}	-40.0
K_{33}	93.0	K_{63}	88.3
K_{34}	-67.0	C_1	462 (+roll A)
K_{35}	-64.8	C_2	-481 (-roll A)
K_{36}	4.0	C_3	-2 (+roll A)
K_{37}	-67.0	C_4	59 (-roll A)
K_{38}	64.8	C_5	-60 (+roll A)
K_{39}	-4.0	C_6	11 (-roll A)
K_{40}	0.0	C_7	1 (+pitch A)

Table 2-3. RCS Force and Moment Coefficients (Cont.)

Symbol	Magnitude	Symbol	Magnitude
C_8	7 (-pitch A)	C_{29}	-28 (+pitch B)
C_9	517 (+pitch A)	C_{30}	-39 (-pitch B)
C_{10}	-350 (-pitch A)	C_{31}	-37 (+yaw B)
C_{11}	30 (+pitch A)	C_{32}	37 (-yaw B)
C_{12}	39 (pitch A)	C_{33}	10 (+yaw B)
C_{13}	-36 (+yaw A)	C_{34}	69 (-yaw B)
C_{14}	36 (-yaw A)	C_{35}	517 (+yaw B)
C_{15}	69 (+yaw A)	C_{36}	-438 (-yaw B)
C_{16}	10 (-yaw A)	C_{1A}	65 (+roll A)
C_{17}	517 (+yaw A)	C_{2A}	26 (-roll A)
C_{18}	-438 (-yaw A)	C_{9A}	72 (+pitch A)
C_{19}	478 (+roll B)	C_{10A}	55.5 (-pitch A)
C_{20}	-463 (-roll B)	C_{17A}	82 (+yaw A)
C_{21}	51 (+roll B)	C_{18A}	82 (-yaw A)
C_{22}	-2 (-roll B)	C_{19A}	65 (+roll B)
C_{23}	-11 (+roll B)	C_{20A}	26 (-roll B)
C_{24}	60 (-roll B)	C_{27A}	72 (+pitch B)
C_{25}	1 (+pitch B)	C_{28A}	55.5 (-pitch B)
C_{26}	-4 (-pitch B)	C_{35A}	82 (+yaw B)
C_{27}	517 (+pitch B)	C_{36A}	82 (-yaw B)
C_{28}	-350 (-pitch B)		

2.2 CENTER-OF-GRAVITY COORDINATES

For spacecraft axes designations, see Figure 2-5.

1. LM-on[1]

   ΔX is variable function of mass.
   Z_{CG} and Y_{CG} are constants.

[1] No LM-on studies were made.

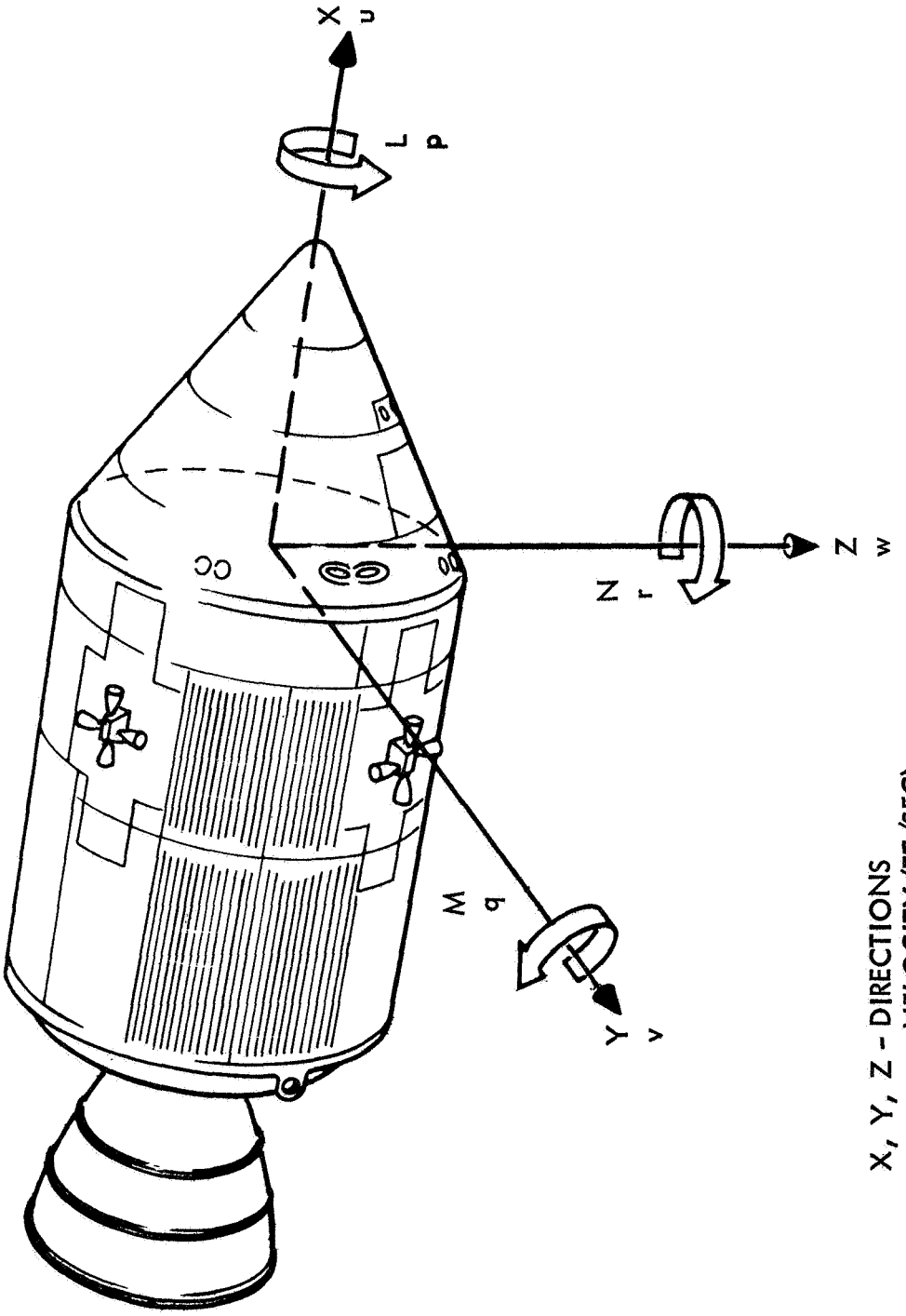

X, Y, Z - DIRECTIONS
u, v, w - VELOCITY (FT/SEC)
L, M, N - MOMENTS (FT/LB)
p, q, r - RATES (RAD/SEC)

Figure 2-5. Spacecraft Body Axes Designations

2. CSM/LM-off

ΔX_{CG}, Z_{CG}, and Y_{CG} are variable functions of mass. (See Figures 2-6, 2-7, and 2-8.)

3. CM

ΔX_{CG}, Y_{CG}, and Z_{CG} are constants.

In all cases, $\Delta X_{CG} = X_{CG_{ACT}} - X_{CG_{REF}}$

$$\ell_X = X_{CG_{REF}} - X_T + \Delta X_{CG}$$

2.3 TAIL-WAGS-DOG FORCES

$$\begin{Bmatrix} F_X \\ F_Y \\ F_Z \end{Bmatrix}_{TWD} = \begin{bmatrix} 0 & 0 & 0 \\ 0 & M_e \ell_{e_\psi} & 0 \\ 0 & 0 & -M_e \ell_{e_\theta} \end{bmatrix} \cdot \begin{Bmatrix} 0 \\ \ddot{\delta}_\psi \\ \delta_\theta \end{Bmatrix}$$

2.4 SPS FORCES ALONG SPACECRAFT AXES

$$\begin{Bmatrix} F_X \\ F_Y \\ F_Z \end{Bmatrix}_T = T_{SPS} \begin{Bmatrix} 1 \\ \delta_\psi \\ -\delta_\theta \end{Bmatrix}$$

2.5 FORCES ALONG BODY AXES (NOT INCLUDING SPS)

$$\left|F\right|_{SUM} = \left|F\right|_{TWD} + \left|F\right|_{RCS}$$

2.6 ALTIMETER DRIVE SIGNAL

This signal is produced from the altitude h by a diode function generator. See Figure 2-9.

2.7 SCARFING COEFFICIENTS

$$P_1 = 1 - \exp\left[\frac{h - 25,000}{28,000}\right]$$

$$P_2 = 1 - \exp\left[\frac{h - 25,000}{21,000}\right]$$

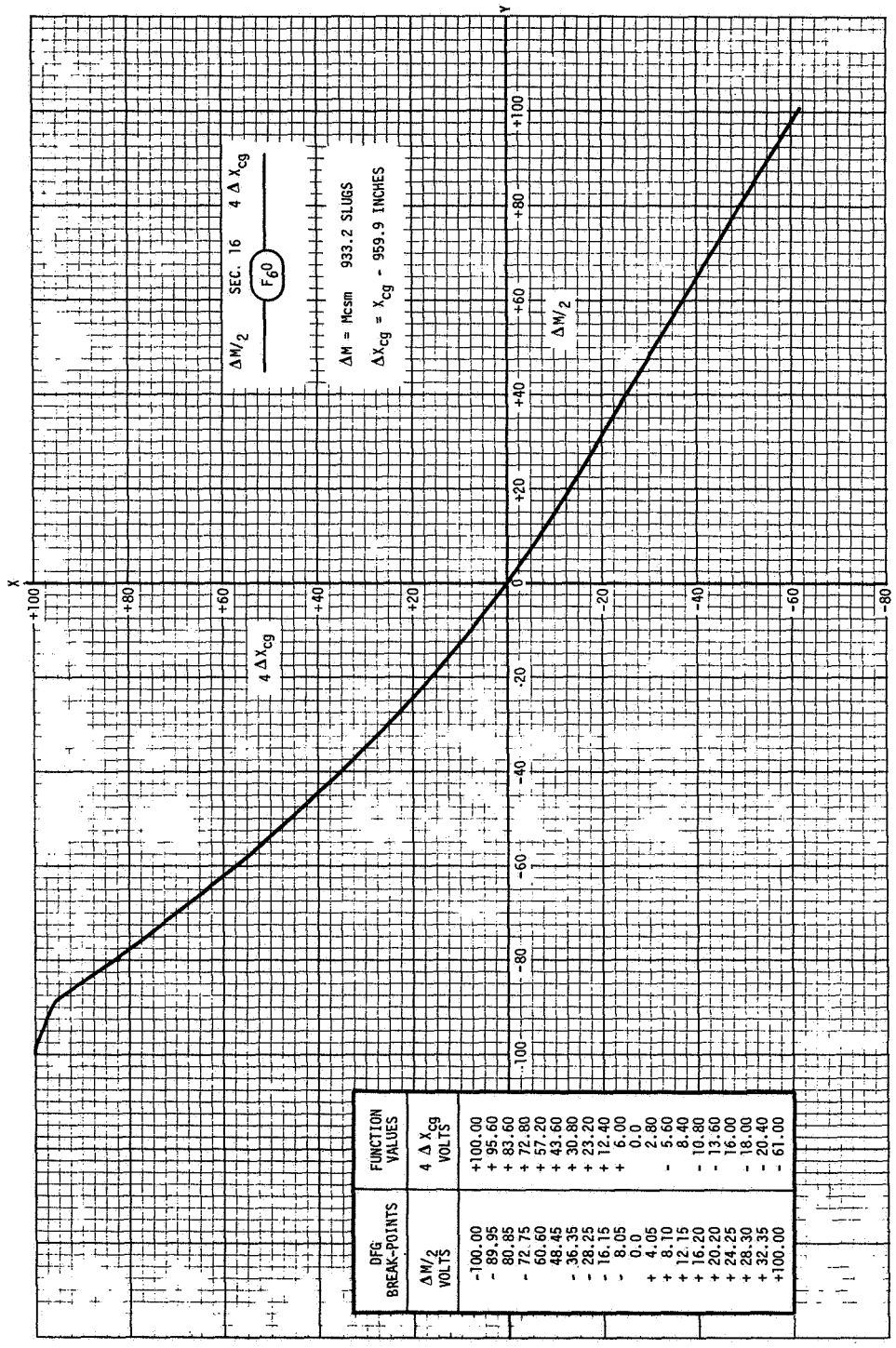

DFG BREAK-POINTS ΔM/2 VOLTS	FUNCTION VALUES 4 Δ Xcg VOLTS
-100.00	+100.00
- 89.95	+ 95.60
- 80.85	+ 83.60
- 72.75	+ 72.80
- 60.60	+ 57.20
- 48.45	+ 43.60
- 36.35	+ 30.80
- 28.25	+ 23.20
- 16.15	+ 12.40
- 8.05	+ 6.00
0.0	0.0
+ 4.05	- 2.80
+ 8.10	- 5.60
+ 12.15	- 8.40
+ 16.20	- 10.80
+ 20.20	- 13.60
+ 24.25	- 16.00
+ 28.30	- 18.00
+ 32.35	- 20.40
+100.00	- 61.00

Figure 2-6. DFG Output Versus Δ M for CSM X Center-of-Gravity Coordinate

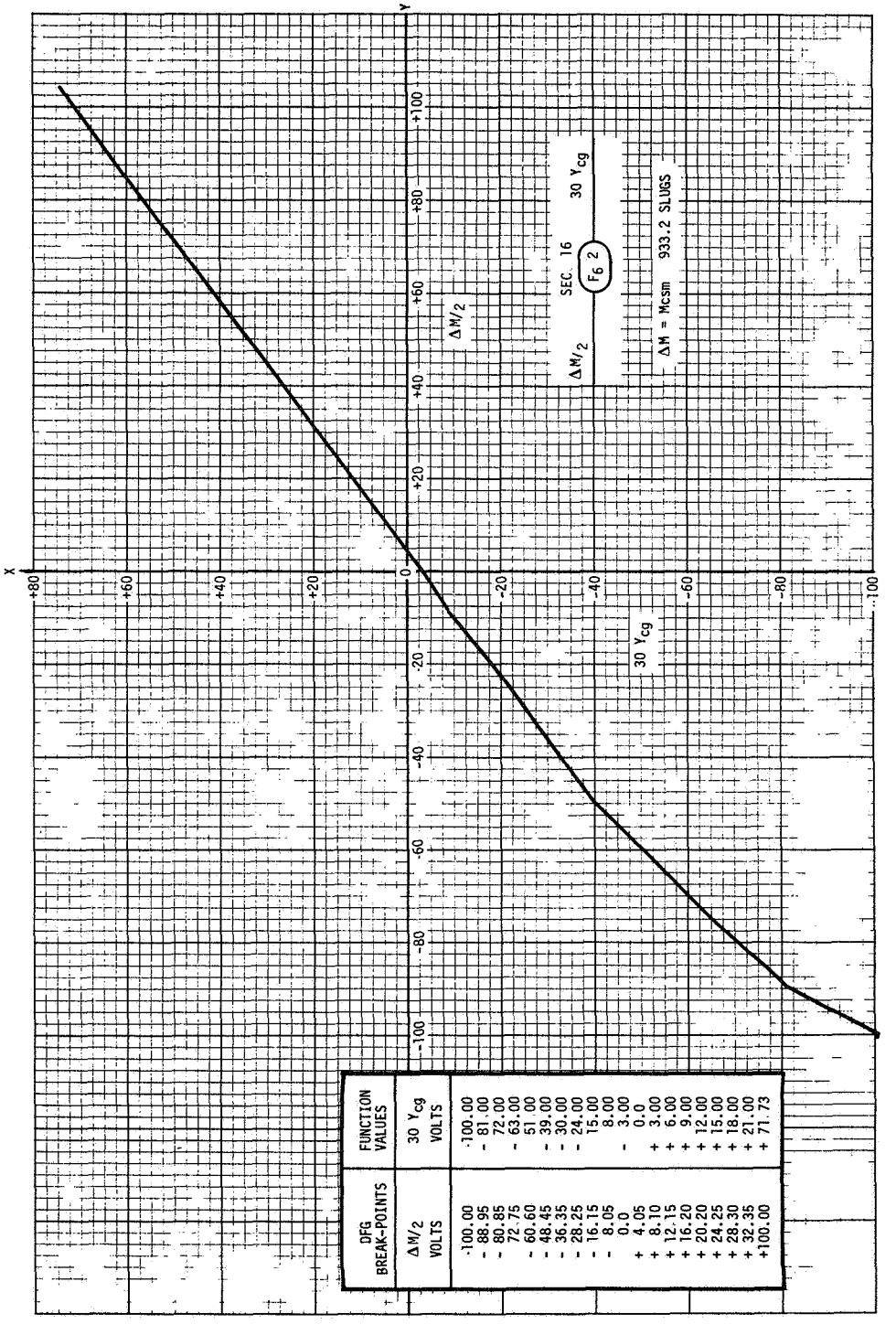

Figure 2-7. DFG Output Versus ΔM for CSM Y Center-of-Gravity Coordinate

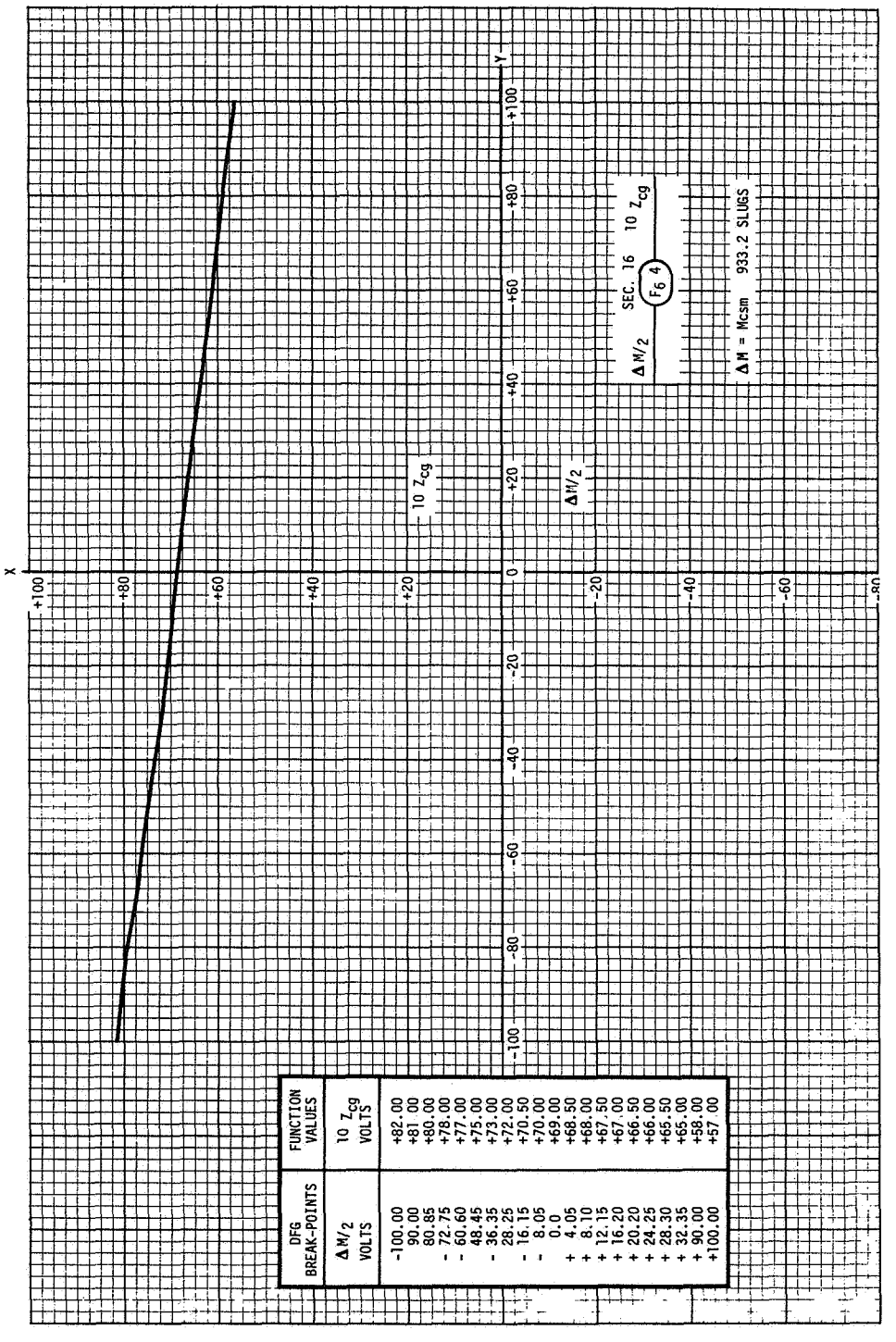

DFG BREAK-POINTS	FUNCTION VALUES
ΔM/2 VOLTS	10 Z_{cg} VOLTS
-100.00	+82.00
90.00	+81.00
80.85	+80.00
- 72.75	+78.00
- 60.60	+77.00
- 48.45	+75.00
- 36.35	+73.00
- 28.25	+72.00
- 16.15	+70.50
- 8.05	+70.00
0.0	+69.00
+ 4.05	+68.50
+ 8.10	+68.00
+ 12.15	+67.50
+ 16.20	+67.00
+ 20.20	+66.50
+ 24.25	+66.00
+ 28.30	+65.50
+ 32.35	+65.00
+ 90.00	+58.00
+100.00	+57.00

Figure 2-8. DFG Output Versus ΔM for CSM Z Center-of-Gravity Coordinate

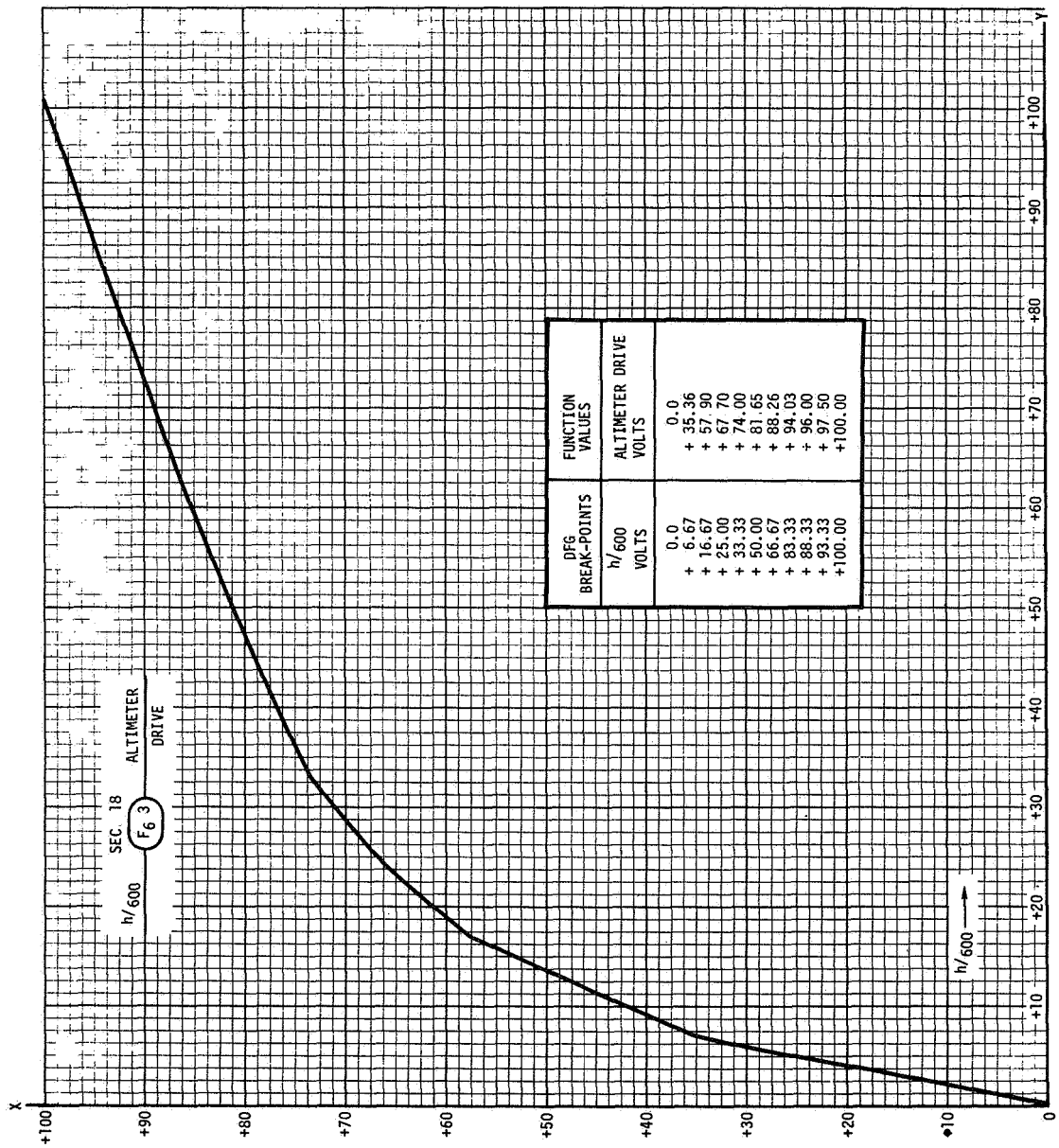

Figure 2-9. DFG Output Versus h for Altimeter Drive

These functions are produced by diode function generators. See Figures 2-10 and 2-11.

2.8 COMMAND MODULE RCS MOMENTS

$$\begin{Bmatrix} L \\ M \\ N \end{Bmatrix}_{CM\ RCS} = \begin{bmatrix} G_1^1 & C_7 & C_{13} \\ C_3 & H_9^2 & C_{15} \\ C_5 & C_{11} & H_{17}^2 \end{bmatrix} \cdot \begin{Bmatrix} T_\phi \\ T_\theta \\ T_\psi \end{Bmatrix}_A$$

$$+ \begin{bmatrix} H_2^1 & C_8 & C_{14} \\ C_4 & G_{10}^2 & C_{16} \\ C_6 & C_{12} & G_{18}^2 \end{bmatrix} \cdot \begin{Bmatrix} -T_\phi \\ -T_\theta \\ -T_\psi \end{Bmatrix}_A$$

$$+ \begin{bmatrix} 0 & G_{19}^1 + C_{25} & C_{31} \\ C_{21} & H_{27}^2 & C_{33} \\ C_{23} & C_{29} & H_{35}^2 \end{bmatrix} \cdot \begin{Bmatrix} T_\phi \\ T_\theta \\ T_\psi \end{Bmatrix}_B$$

$$+ \begin{bmatrix} 0 & C_{26} & H_{20}^1 + C_{32} \\ 0 & G_{28}^2 + C_{22} & C_{44} \\ C_{24} & C_{30} & G_{36}^2 \end{bmatrix} \cdot \begin{Bmatrix} -T_\phi \\ -T_\theta \\ -T_\psi \end{Bmatrix}_B$$

where

$$G_i^1 = C_i - |P_1 C_{iA}|$$

$$G_i^2 = C_i - |P_2 C_{iA}|$$

$$H_i^1 = C_i + |P_1 C_{iA}|$$

$$H_i^2 = C_i + |P_2 C_{iA}|$$

Refer to Table 2-3 for RCS moment coefficients.

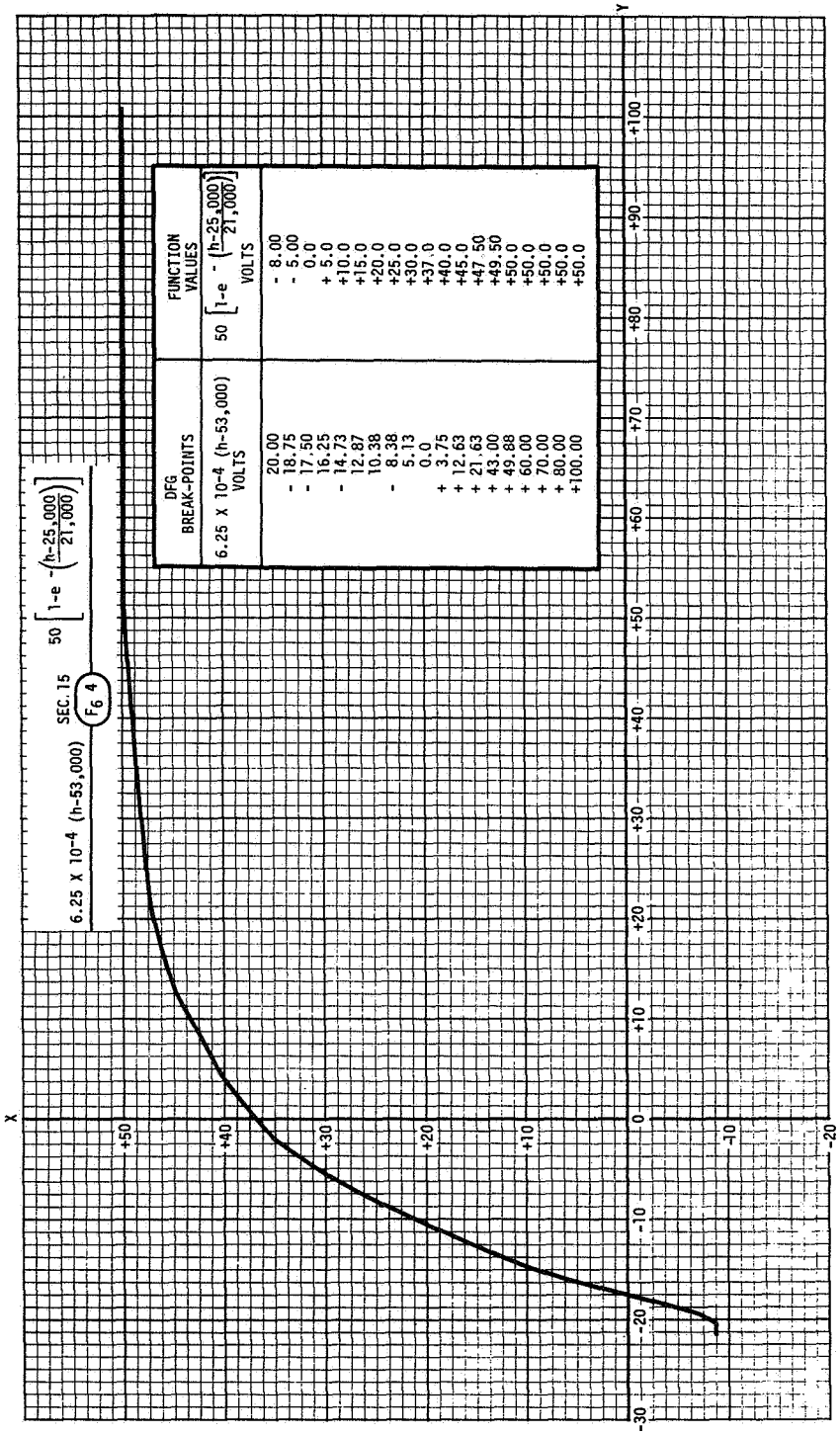

Figure 2-10. DFG Output Versus h for Scarfing Coefficient P_1

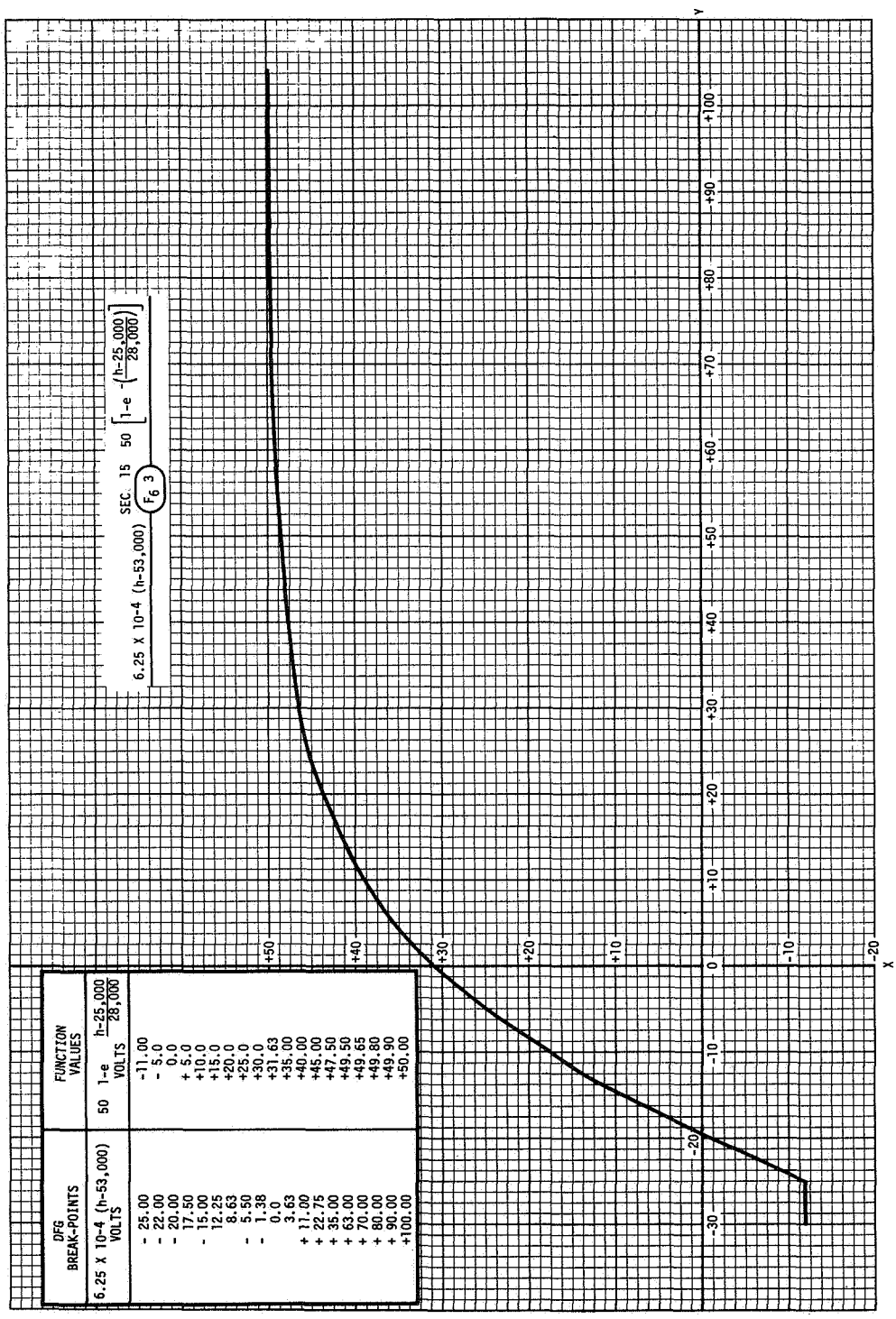

Figure 2-11. DFG Output Versus h for Scarfing Coefficient P_2

2.9 SERVICE MODULE RCS MOMENTS

$$\begin{Bmatrix} L_1 \\ M_1 \\ N_1 \end{Bmatrix}_{SM\ RCS} = \begin{bmatrix} 0 & Z & -Y \\ -Z & 0 & \Delta X \\ Y & -\Delta X & 0 \end{bmatrix}_{CG} \cdot \begin{Bmatrix} F_X \\ F_Y \\ F_Z \end{Bmatrix}_{SM\ RCS}$$

$$\begin{Bmatrix} L_2 \\ M_2 \\ N_2 \end{Bmatrix}_{SM\ RCS} = \begin{Bmatrix} K_8(A+B+C+D)_4 - K_9(A+B+C+D)_2 \\ \begin{bmatrix} K_{20} & K_{22} \\ K_{22} & K_{20} \end{bmatrix} \cdot \begin{Bmatrix} A-C \\ B-D \end{Bmatrix}_1 + \begin{bmatrix} -K_{21} & -K_{23} \\ K_{23} & -K_{21} \end{bmatrix} \cdot \begin{Bmatrix} A-C \\ B-D \end{Bmatrix}_3 \end{Bmatrix}$$

$$+ \begin{Bmatrix} 0 \\ \begin{bmatrix} K_{24} & -K_{26} \\ K_{26} & K_{24} \end{bmatrix} \cdot \begin{Bmatrix} A-C \\ B-D \end{Bmatrix}_2 + \begin{bmatrix} -K_{25} & K_{27} \\ -K_{27} & -K_{25} \end{bmatrix} \cdot \begin{Bmatrix} A-C \\ B-D \end{Bmatrix}_4 \end{Bmatrix}$$

$$\begin{Bmatrix} L \\ M \\ N \end{Bmatrix}_{SM\ RCS} = \begin{Bmatrix} L_1 \\ M_1 \\ N_1 \end{Bmatrix}_{SM\ RCS} + \begin{Bmatrix} L_2 \\ M_2 \\ N_2 \end{Bmatrix}_{SM\ RCS}$$

Refer to Table 2-3 for RCS moment coefficients.

2.10 DOG-WAGS-TAIL MOMENTS

$$\begin{Bmatrix} T_P \\ T_Y \end{Bmatrix}_{DWT} = \begin{bmatrix} \dot{q} & 0 \\ 0 & \dot{r} \end{bmatrix} \cdot \begin{Bmatrix} I_{\bar{e}\theta} + m_e \ell_x \ell_{e\theta} \\ I_{\bar{e}\psi} + m_e \ell_x \ell_{e\psi} \end{Bmatrix}$$

2.11 TAIL-WAGS-DOG MOMENTS

$$\begin{Bmatrix} L \\ M \\ N \end{Bmatrix}_{TWD} = \begin{Bmatrix} 0 \\ +I_{\bar{e}\theta}\ddot{\delta}_\theta \\ +I_{\bar{e}\psi}\ddot{\delta}_\psi \end{Bmatrix} + \begin{bmatrix} 0 & +Z & -Y \\ 0 & 0 & -\ell_X \\ 0 & +\ell_X & 0 \end{bmatrix}_{CG} \cdot \begin{Bmatrix} F_X \\ F_Y \\ F_Z \end{Bmatrix}_{TWD}$$

$$\ell_X = \ell g + \Delta X$$

2.12 BODY BENDING MOMENTS (LM-ON)

$$\begin{Bmatrix} L \\ M \\ N \end{Bmatrix}_{BN} = T_{SPS} \begin{bmatrix} 0 & 0 & 0 \\ \phi_{21} & \phi_{22} & \phi_{23} \\ -\phi_{31} & -\phi_{32} & -\phi_{33} \end{bmatrix} \cdot \begin{Bmatrix} d_1 \\ d_2 \\ d_3 \end{Bmatrix}$$

$$-\ell_X \begin{bmatrix} 0 & 0 & 0 \\ \sigma_{21} & \sigma_{22} & \sigma_{23} \\ \sigma_{31} & \sigma_{32} & \sigma_{33} \end{bmatrix} \cdot \begin{Bmatrix} d_1 \\ d_2 \\ d_3 \end{Bmatrix}$$

2.13 SPS MOMENTS ABOUT SPACECRAFT AXES

$$\begin{Bmatrix} L \\ M \\ N \end{Bmatrix}_T = \begin{bmatrix} 0 & Z & -Y \\ -Z & 0 & \ell_X \\ Y & -\ell_X & 0 \end{bmatrix}_{CG} \cdot \begin{Bmatrix} F_X \\ F_Y \\ F_Z \end{Bmatrix}_T + T_{SPS} \begin{Bmatrix} 0 \\ \epsilon_\theta \\ \epsilon_\psi \end{Bmatrix}_T$$

2.14 TOTAL MOMENT ABOUT SPACECRAFT AXES

$$\begin{Bmatrix} L \\ M \\ N \end{Bmatrix} = \begin{Bmatrix} L \\ M \\ N \end{Bmatrix}_T + \begin{Bmatrix} L \\ M \\ N \end{Bmatrix}_{TWD} + \begin{Bmatrix} L \\ M \\ N \end{Bmatrix}_{BN} + \begin{Bmatrix} L \\ M \\ N \end{Bmatrix}_{RCS} + \begin{Bmatrix} L \\ M \\ N \end{Bmatrix}_A$$

2.15 MOMENTS AND PRODUCTS OF INERTIA

1. LM-on

   I_{XX}, I_{YY}, I_{ZZ}, I_{XY}, I_{XZ}, and I_{YZ} (Values are not available.)

2. CSM

   I_{XX}, I_{YY}, I_{ZZ}, I_{XY}, I_{XZ}, and I_{YZ} are functions of mass. (See Figures 2-12 through 2-17.)

3. CM

   I_{XX}, I_{YY}, I_{ZZ}, I_{XY}, I_{XZ}, and I_{YZ} are constants. (See Table 2-1.)

2.16 BODY ANGULAR ACCELERATIONS

$$\begin{Bmatrix} \dot{p} \\ \dot{q} \\ \dot{r} \end{Bmatrix} = \begin{bmatrix} I \end{bmatrix}^{-1} \cdot \begin{Bmatrix} L \\ M \\ N \end{Bmatrix} - \begin{bmatrix} I \end{bmatrix}^{-1} \cdot \begin{bmatrix} 0 & -r & q \\ r & 0 & q \\ -q & p & 0 \end{bmatrix} \cdot \begin{bmatrix} I \end{bmatrix} \cdot \begin{Bmatrix} p \\ q \\ r \end{Bmatrix}$$

where

$$\begin{bmatrix} I \end{bmatrix} = \begin{bmatrix} I_{XX} & -I_{XY} & -I_{XZ} \\ -I_{XY} & I_{YY} & -I_{YZ} \\ -I_{XY} & -I_{YZ} & I_{ZZ} \end{bmatrix}$$

These moments and products of inertia are variable. See paragraph 2.15

2.17 QUATERNION RATE MATRIX

Figure 2-18 illustrates how the quaternion technique is employed to form the inertial-to-body transformation required in the RTSS.

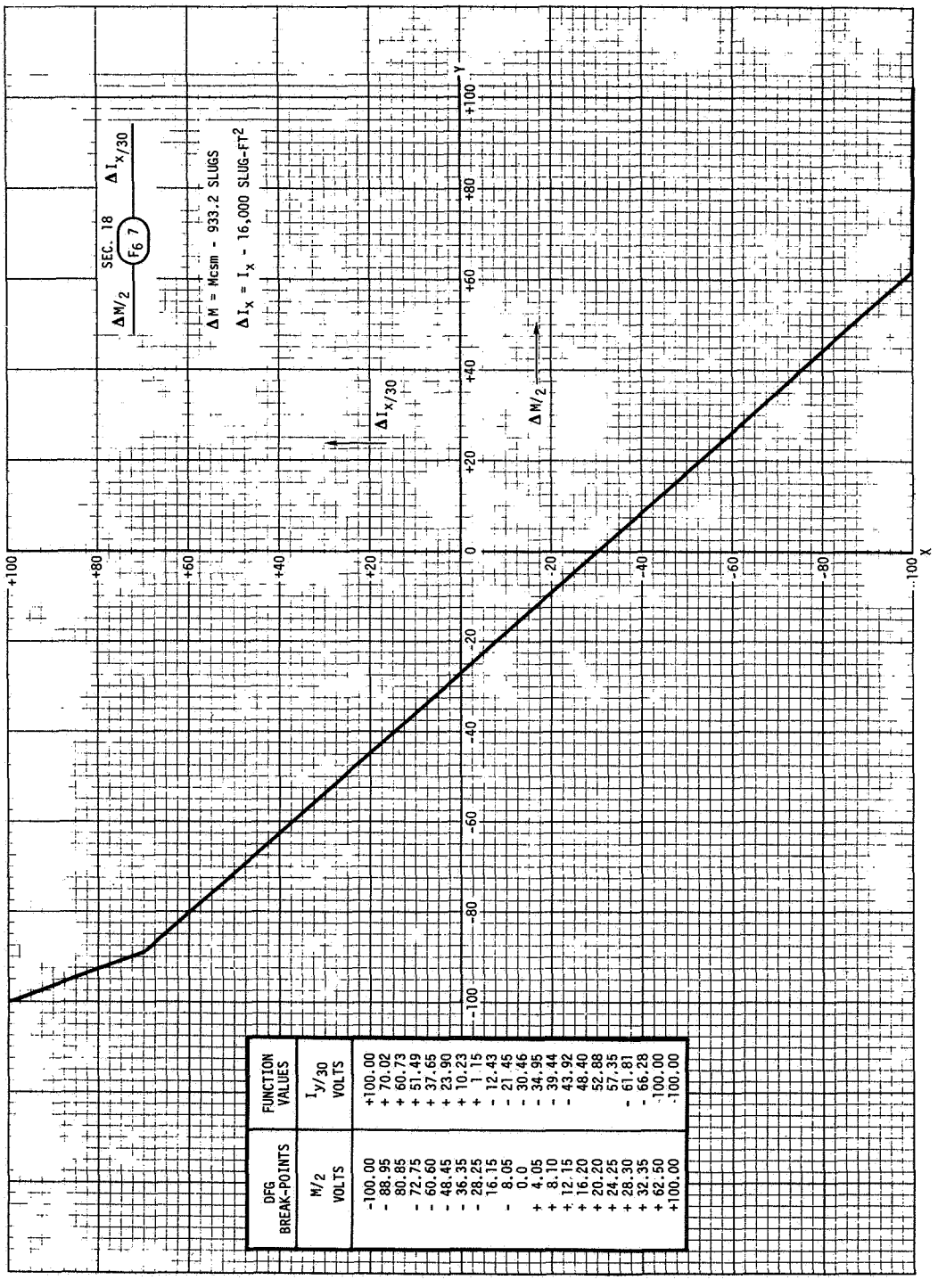

DFG BREAK-POINTS	FUNCTION VALUES
M/2 VOLTS	Iy/30 VOLTS
-100.00	+100.00
- 88.95	+ 70.02
- 80.85	+ 60.73
- 72.75	+ 51.49
- 60.60	+ 37.65
- 48.45	+ 23.90
- 36.35	+ 10.23
- 28.25	+ 1.15
- 16.15	- 12.43
- 8.05	- 21.45
0.0	- 30.46
+ 4.05	- 34.95
+ 8.10	- 39.44
+ 12.15	- 43.92
+ 16.20	48.40
+ 20.20	52.88
+ 24.25	57.35
+ 28.30	- 61.81
+ 32.35	- 66.28
+ 62.50	-100.00
+100.00	-100.00

Figure 2-12. DFG Output Versus ΔM for CSM IXX Moment of Inertia

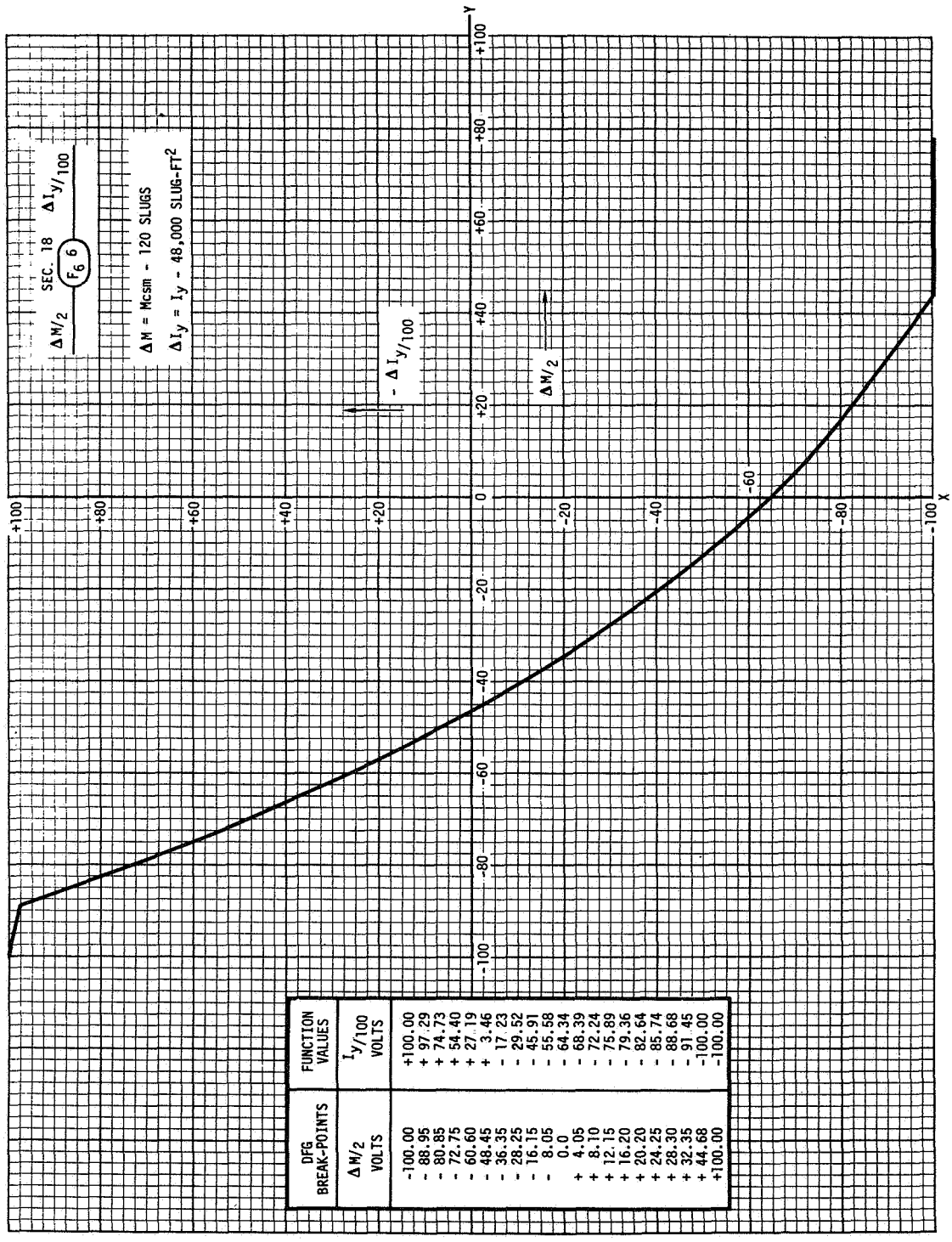

DFG BREAK-POINTS	FUNCTION VALUES
ΔM/2 VOLTS	Iy/100 VOLTS
-100.00	+100.00
- 88.95	+ 97.29
- 80.85	+ 74.73
- 72.75	+ 54.40
- 60.60	+ 27.19
- 48.45	+ 3.46
- 36.35	- 17.23
- 28.25	- 29.52
- 16.15	- 45.91
- 8.05	- 55.58
0.0	- 64.34
+ 4.05	- 68.39
+ 8.10	- 72.24
+ 12.15	- 75.89
+ 16.20	- 79.36
+ 20.20	- 82.64
+ 24.25	- 85.74
+ 28.30	- 88.68
+ 32.35	- 91.45
+ 44.68	-100.00
+100.00	-100.00

Figure 2-13. DFG Output Versus ΔM for CSM Iyy Moment of Inertia

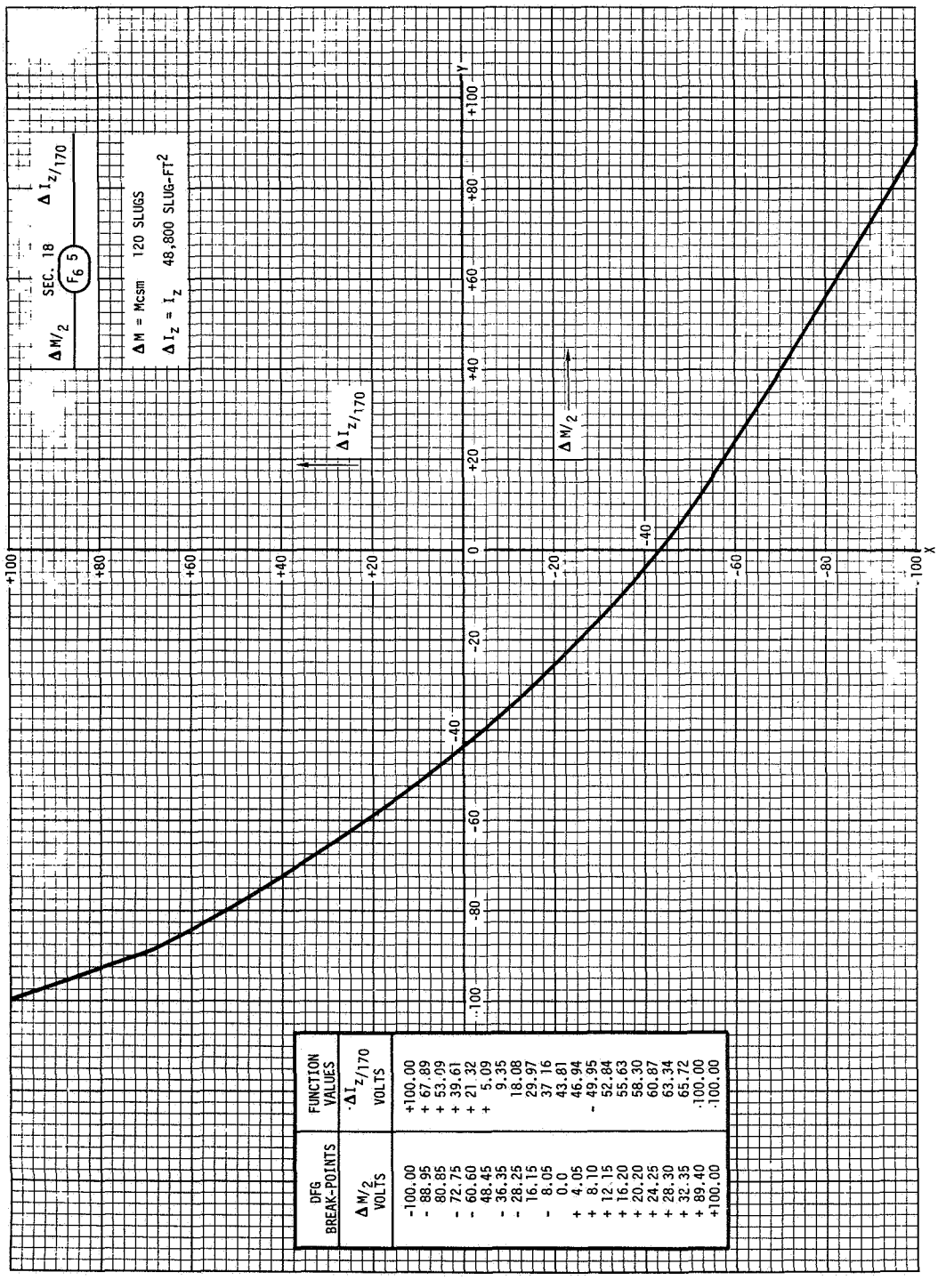

DFG BREAK-POINTS	FUNCTION VALUES
$\Delta M/2$ VOLTS	$\Delta I_{z/170}$ VOLTS
-100.00	+100.00
- 88.95	+ 67.89
- 80.85	+ 53.09
- 72.75	+ 39.61
- 60.60	+ 21.32
- 48.45	+ 5.09
- 36.35	- 9.35
- 28.25	- 18.08
- 16.15	- 29.97
- 8.05	- 37.16
0.0	- 43.81
+ 4.05	- 46.94
+ 8.10	- 49.95
+ 12.15	- 52.84
+ 16.20	- 55.63
+ 20.20	- 58.30
+ 24.25	- 60.87
+ 28.30	- 63.34
+ 32.35	- 65.72
+ 89.40	-100.00
+100.00	-100.00

Figure 2-14. DFG Output Versus ΔM for CSM I_{ZZ} Moment of Inertia

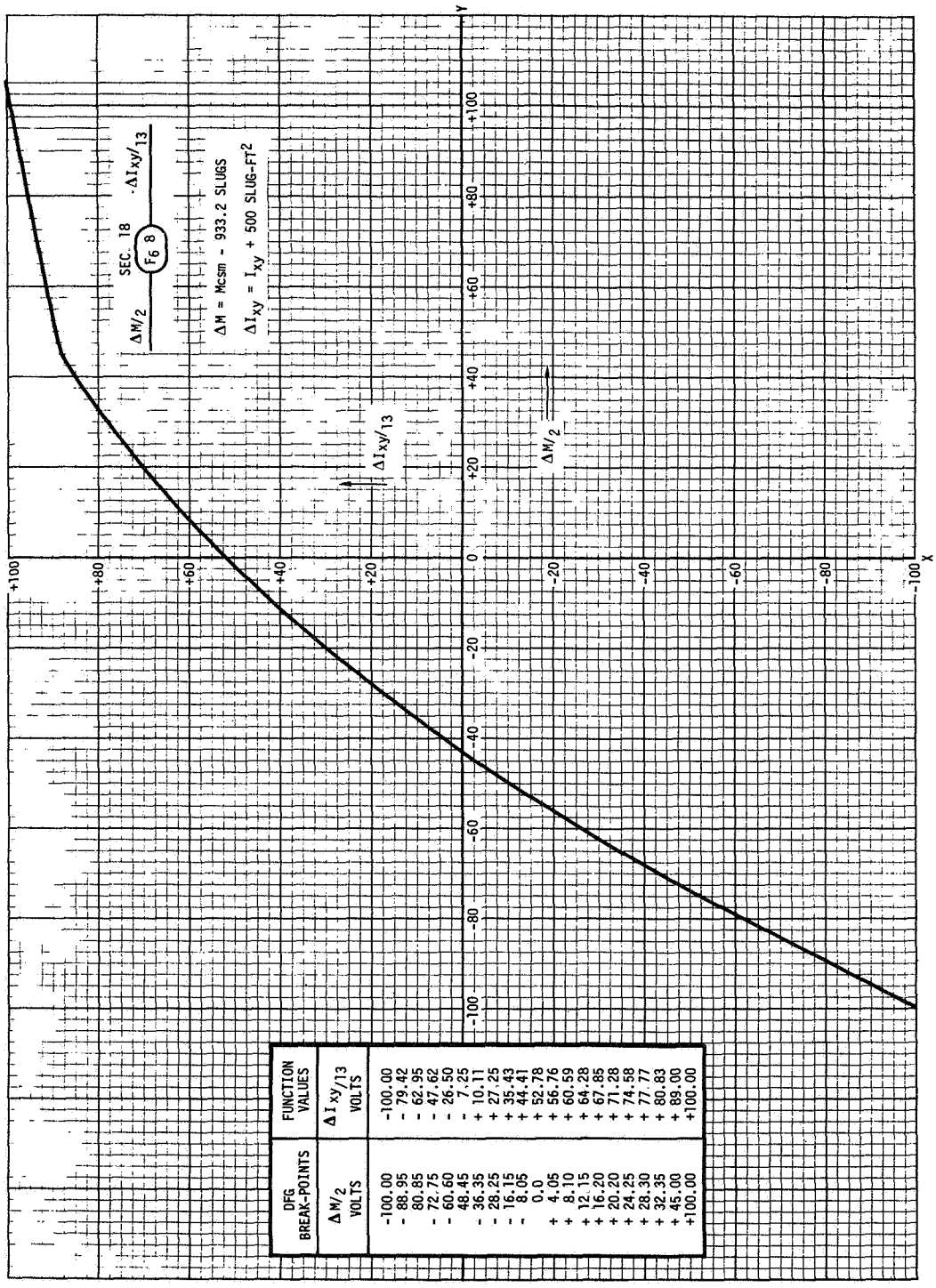

DFG BREAK-POINTS	FUNCTION VALUES
ΔM/2 VOLTS	ΔIxy/13 VOLTS
-100.00	-100.00
- 88.95	- 79.42
- 80.85	- 62.95
- 72.75	- 47.62
- 60.60	- 26.50
- 48.45	- 7.25
- 36.35	+ 10.11
- 28.25	+ 27.25
- 16.15	+ 35.43
- 8.05	+ 44.41
0.0	+ 52.78
+ 4.05	+ 56.76
+ 8.10	+ 60.59
+ 12.15	+ 64.28
+ 16.20	+ 67.85
+ 20.20	+ 71.28
+ 24.25	+ 74.58
+ 28.30	+ 77.77
+ 32.35	+ 80.83
+ 45.00	+ 89.00
+100.00	+100.00

Figure 2-15. DFG Output Versus ΔM for CSM I_{XY} Product of Inertia

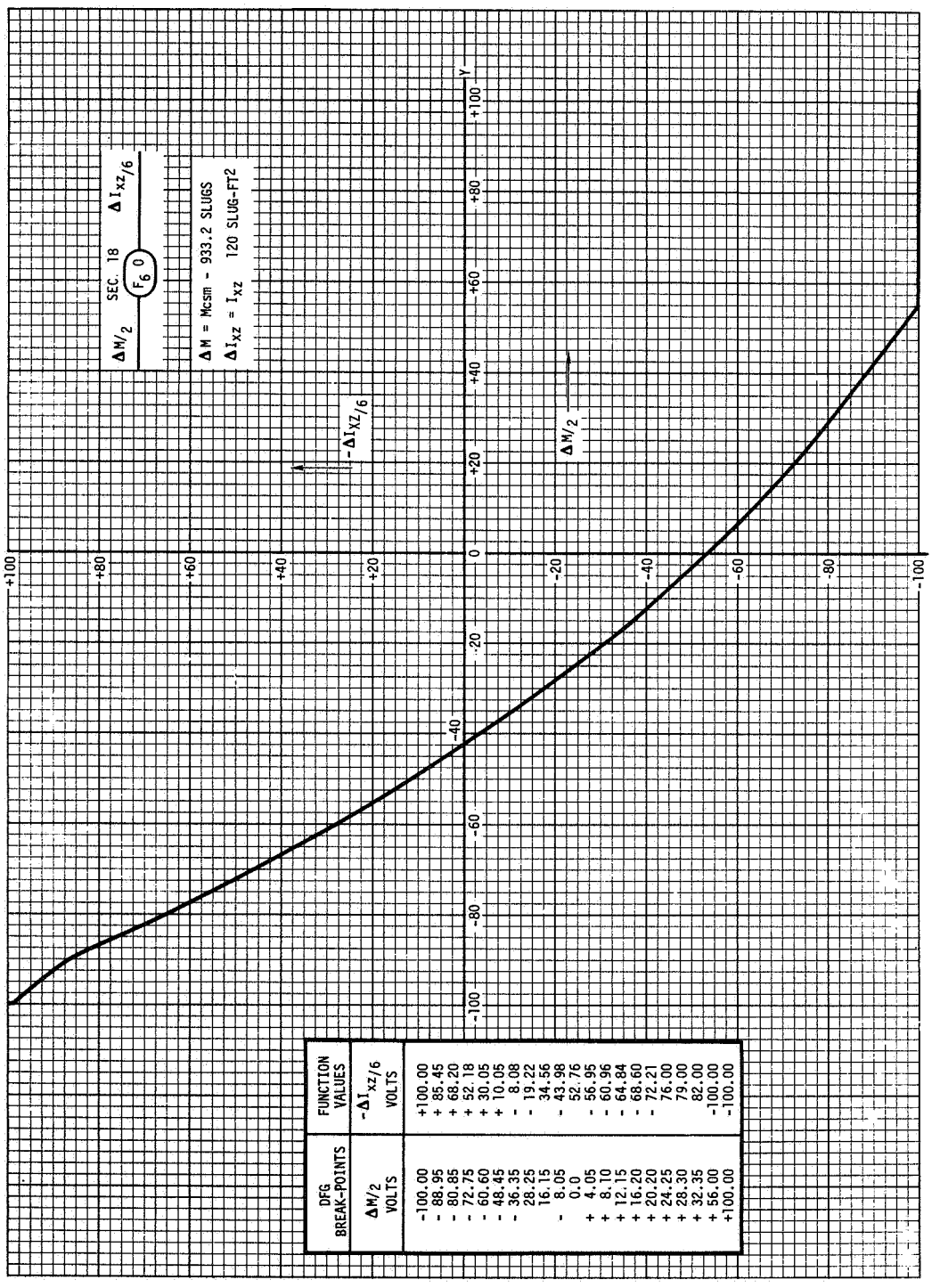

DFG BREAK-POINTS ΔM/2 VOLTS	FUNCTION VALUES -ΔIxz/6 VOLTS
-100.00	+100.00
- 88.95	+ 85.45
- 80.85	+ 68.20
- 72.75	+ 52.18
- 60.60	+ 30.05
- 48.45	+ 10.05
- 36.35	- 8.08
- 28.25	- 19.22
16.15	- 34.56
- 8.05	- 43.98
0.0	52.76
+ 4.05	- 56.95
+ 8.10	- 60.96
+ 12.15	- 64.84
+ 16.20	- 68.60
+ 20.20	- 72.21
+ 24.25	76.00
+ 28.30	79.00
+ 32.35	82.00
+ 56.00	-100.00
+100.00	-100.00

Figure 2-16. DFG Output Versus ΔM for CSM IXZ Product of Inertia

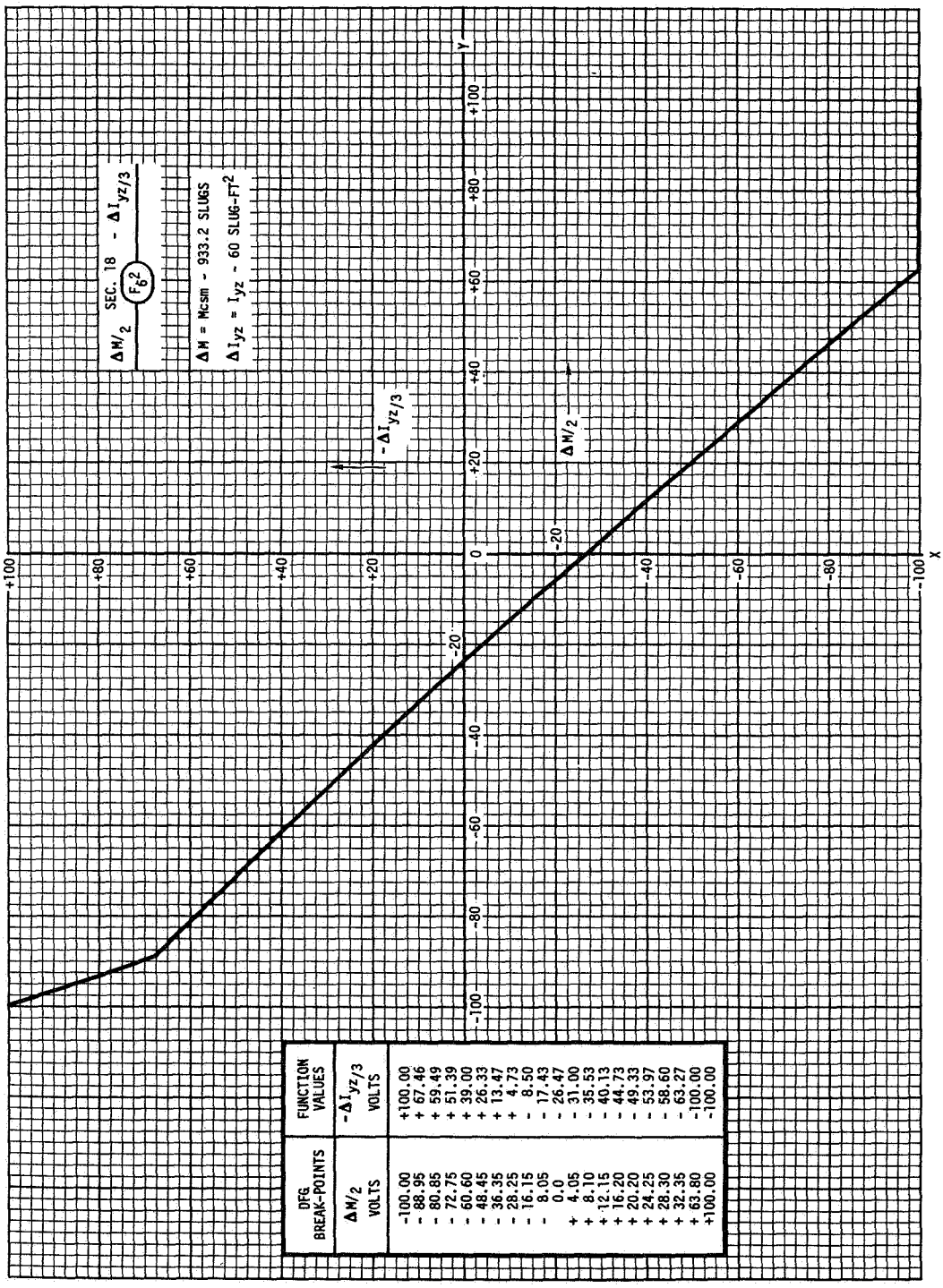

DFG BREAK-POINTS	FUNCTION VALUES
ΔM/2 VOLTS	-ΔIyz/3 VOLTS
-100.00	+100.00
- 88.95	+ 67.46
- 80.85	+ 59.49
- 72.75	+ 51.39
- 60.60	+ 39.00
- 48.45	+ 26.33
- 36.35	+ 13.47
- 28.25	+ 4.73
- 16.15	- 8.50
- 8.05	- 17.43
0.0	- 26.47
+ 4.05	- 31.00
+ 8.10	- 35.53
+ 12.15	- 40.13
+ 16.20	- 44.73
+ 20.20	- 49.33
+ 24.25	- 53.97
+ 28.30	- 58.60
+ 32.35	- 63.27
+ 63.80	-100.00
+100.00	-100.00

Figure 2-17. DFG Output Versus ΔM for CSM Iyz Product of Inertia

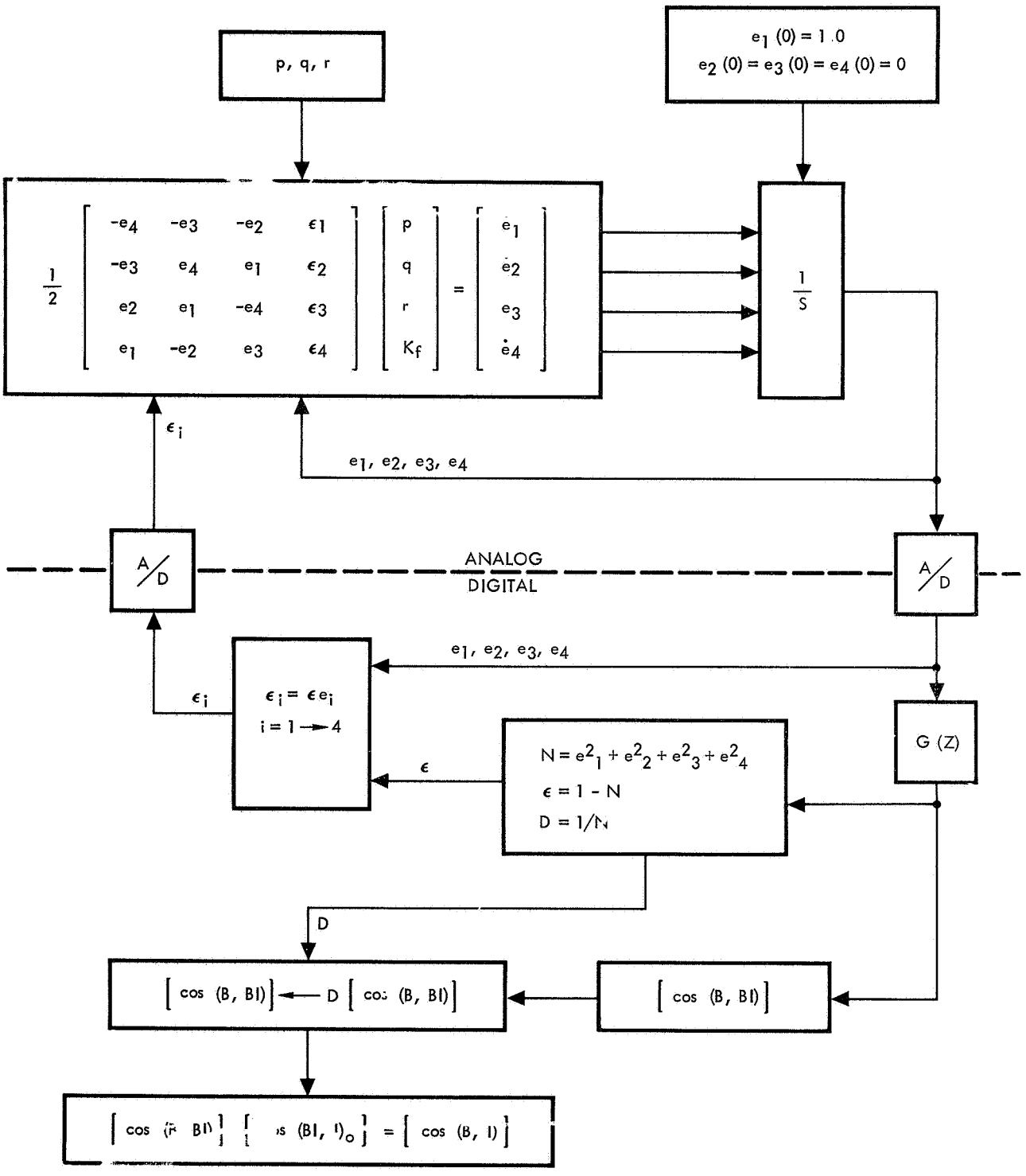

Figure 2-18. Quaternion Rate Matrix

2.18 BENDING DYNAMICS (LM-ON)[1]

$$\begin{Bmatrix} m_1\left[\ddot{d}_1 + 2D_1\,\omega_1\dot{d}_1 + \omega_1 d_1\right] \\ m_2\left[\ddot{d}_2 + 2D_2\,\omega_2\dot{d}_2 + \omega_2 d_2\right] \\ m_3\left[\ddot{d}_3 + 2D_3\,\omega_3\dot{d}_3 + \omega_3 d_3\right] \end{Bmatrix} = (T_{SPS}\delta_\psi + m_e\ell_{e\psi}\ddot{\delta}_\psi)\begin{Bmatrix}\phi_{31}\\ \phi_{32}\\ \phi_{33}\end{Bmatrix}_e$$

$$- (T_{SPS}\delta_\theta + m_e\ell_{e\theta}\ddot{\delta}_\theta)\begin{Bmatrix}\phi_{21}\\ \phi_{22}\\ \phi_{23}\end{Bmatrix}_e$$

$$\frac{-(I_{\bar{e}\,\theta}\ddot{\delta}_\theta)}{12}\begin{Bmatrix}\sigma_{21}\\ \sigma_{22}\\ \sigma_{23}\end{Bmatrix}_e \frac{-(I_{\bar{e}\,\psi}\ddot{\delta}_\psi)}{12}\begin{Bmatrix}\sigma_{31}\\ \sigma_{32}\\ \sigma_{33}\end{Bmatrix}_e$$

Single subscripts 1, 2, and 3 denote bending modes 1, 2, and 3, respectively. Refer to Table 2-4 for LM-on bending coefficients.

2.19 SENSED BODY RATES (LM-ON)

$$\begin{Bmatrix}p\\ q\\ r\end{Bmatrix}_F = \begin{Bmatrix}p\\ q\\ r\end{Bmatrix} + \begin{bmatrix}\lambda_{11} & \lambda_{12} & \lambda_{13}\\ \lambda_{21} & \lambda_{22} & \lambda_{23}\\ \lambda_{31} & \lambda_{32} & \lambda_{33}\end{bmatrix}_S \cdot \begin{Bmatrix}\dot{d}_1\\ \dot{d}_2\\ \dot{d}_3\end{Bmatrix}$$

2.20 COMMAND MODULE AND SERVICE MODULE RCS THRUST SHAPING

Figure 2-19 illustrates RCS thrust shaping.

[1] No LM-on studies were made.

Table 2-4. LM-On Bending Coefficients

CSM/LM Propellant Loading	jth Mode	ω_j	$10 \times \phi_{2j}$	$10 \times \phi_{3j}$	$10^3 \times \sigma_{2j}$	$10^3 \times \sigma_{3j}$	$10^4 \times \lambda_{1j}$	$10^3 \times \lambda_{2j}$	$10^3 \times \lambda_{3j}$
NOMINAL									
Full	1	13.06	0.3294	0.6023	0.6605	-0.3967	0.2486	0.5974	-0.3090
Full	2	14.19	0.5176	-0.3372	-0.3741	-0.6000	0.5304	-0.3347	-0.4559
Full	3	15.32	0.2919	-0.1589	-0.1042	-0.2658	0.9161	-0.05978	-0.2428
1/2 full	1	13.82	-0.5206	-0.6763	-0.6589	0.5334	-0.1059	-0.6028	0.4267
1/2 full	2	14.57	0.5493	-0.4736	-0.5074	-0.5929	0.3473	-0.4462	-0.4399
1/2 full	3	15.51	0.2716	-0.3091	-0.1947	-0.1726	1.4660	-0.1436	-0.2133
1/4 full	1	14.07	0.4405	0.8190	0.7691	-0.4293	0.02244	0.7058	-0.3570
1/4 full	2	14.95	0.7629	-0.4505	-0.4182	-0.7434	0.2632	-0.3618	-0.5890
1/4 full	3	18.65	0.1436	-0.1101	-0.06287	-0.07384	8.182	-0.02469	-0.1058
*WORST CASE									
Full	1	10.45	0.494	0.903	0.991	-0.596	0.373	0.896	-0.463
Full	2	11.35	0.777	-0.506	-0.567	-0.900	0.0796	-0.502	-0.684
Full	3	12.26	0.438	-0.238	-0.156	-0.398	1.370	-0.0898	-0.364
1/2 full	1	11.05	-0.781	-1.014	-0.838	0.800	-0.159	-0.905	0.640
1/2 full	2	11.66	0.824	-0.710	-0.761	-0.890	0.521	-0.670	-0.645
1/2 full	3	12.41	0.407	-0.463	-0.292	-0.269	2.20	-0.215	-0.320
1/4 full	1	11.25	0.6608	1.229	1.154	-0.644	0.03366	1.059	-0.5355
1/4 full	2	11.96	1.144	-0.6758	-0.6273	-1.115	0.3948	-0.5427	-0.8835
1/4 full	3	14.92	0.2154	-0.1652	-0.09431	-0.1108	12.27	-0.03704	-0.1587

*Worst case ≡ +50 percent tolerance on translational and rotational displacement
-20 percent tolerance on frequency

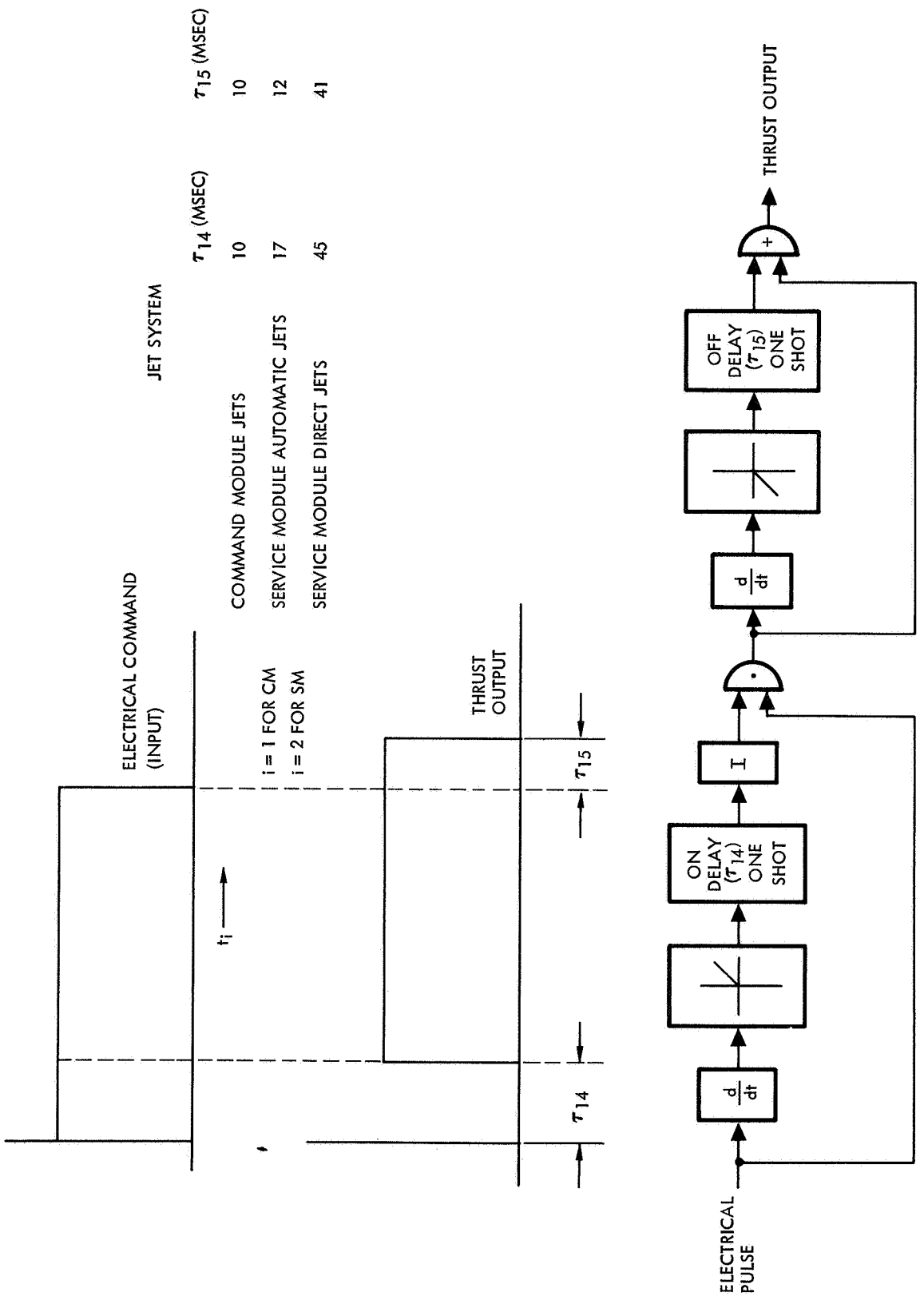

Figure 2-19. RCS Thrust Shaping Diagram

2.21 SPS THRUST SHAPING

1. Thrust-on delay and rise time

$$T_{SPS} = 0.0 \qquad t_3 < \tau_{16}$$

$$T_{SPS} = T_{RATED}\left\{1 - \frac{\exp\left[-D_{10}\omega_{10}(t_3 - \tau_{16})\right]}{\left[1 - D_{10}^2\right]^{1/2}} \sin\left[\omega_{11}(t_3 - \tau_{16}) + \psi\right]\right\} \qquad t_3 \geq \tau_{16}$$

where t_3 is time from thrust-on signal.

2. Thrust-off delay and decay time

$$T_{SPS} = T_{SPS}\Big|_{t = t_3} \qquad t_4 < \tau_{17}$$

$$T_{SPS} = T_{RATED}\exp\left[-K_1(t_4 - \tau_{17})\right] \qquad \tau_{17} \leq t_4 < \tau_{18}$$

$$T_{SPS} = 0.20\, T_{RATED}\exp\left[-K_2(t_4 - \tau_{18})\right] \qquad \tau_{18} \leq t_4 < \tau_{19}$$

where t_4 is time from thrust-off signal.

3.0 RTSS AND ASSOCIATED INTERFACE HARDWARE[1]

This section presents all equations and operations requiring digital operations. Included are those functions which must be calculated very precisely and which may not drift with time. Also included are those functions requiring extensive stored tables of data points.

Special provisions have been made for transmitting data in and out of the core memory without disrupting normal computation. The memory interface connector (MIC) serves this purpose.

The MIC operates between the core memory and another special purpose device known as the digital-to-digital interface. The interfacing device stores data in numerous registers for availability whenever the information is required by external equipment; conversely, it can store information whenever it is available from external equipment.

Other special purpose interfacing hardware is employed between the digital-to-digital interface and the prototype hardware as shown in Figure 3-1. These interfaces serve various purposes as described by later paragraphs in this section. The numbers in the boxes of Figure 3-1 correspond to the defining paragraphs in this section.

The digital computer, an SDS 9300, has a parity word size of 24 bits, a memory cycle of 1.75 microseconds, and two memory banks of 16,000 words each.

Peripheral equipment to the SPS 9300 consists of the following:

4	Magnetic tape units
12	A/D channels
21	D/A channels
1	Printer
1	Card reader
1	Card punch unit
1	Flexi-typewriter

[1] RTSS is the abbreviation for real time simulation system and has become synonymous with the SDS 9300.

The analog-to-digital converters are made by Scientific Data Systems and convert continuous voltages between ±100 volts to 13-bit parallel words. The average error is 2.5 parts in 8000, or approximately 0.031 percent for full-scale input.

3.1 DIGITAL COMPUTATIONS

The computations performed per frame vary according to the segment of the mission under study. The computation flow was therefore described in two ways. (1) those computations made for altitude h above 400,000 feet, including SPS thrusting and rendezvous; (2) those computations made for altitude h below 400,000 feet, including separation and entry. This division is clearly shown in Figures 3-1 and 3-2.

The translational accelerations of the spacecraft are produced by four sources. Because of their dissimilarity, these four accelerations are integrated by four distinct methods, each tailored to the dynamic variations in the source. The sources and their integrators are as follows:

1. Control sets. Analog integrators on a per axis basis
2. Service propulsion system. Calculation of impulse per computation cycle based an analytical thrust profile and time from ignition
3. Gravity. Separate trapezoidal integrators
4. Aerodynamic forces (entry only). Separate trapezoidal integrators

Tables 3-1 through 3-6 will aid in interpreting the equations contained in this subsection by defining the notations and symbols employed.

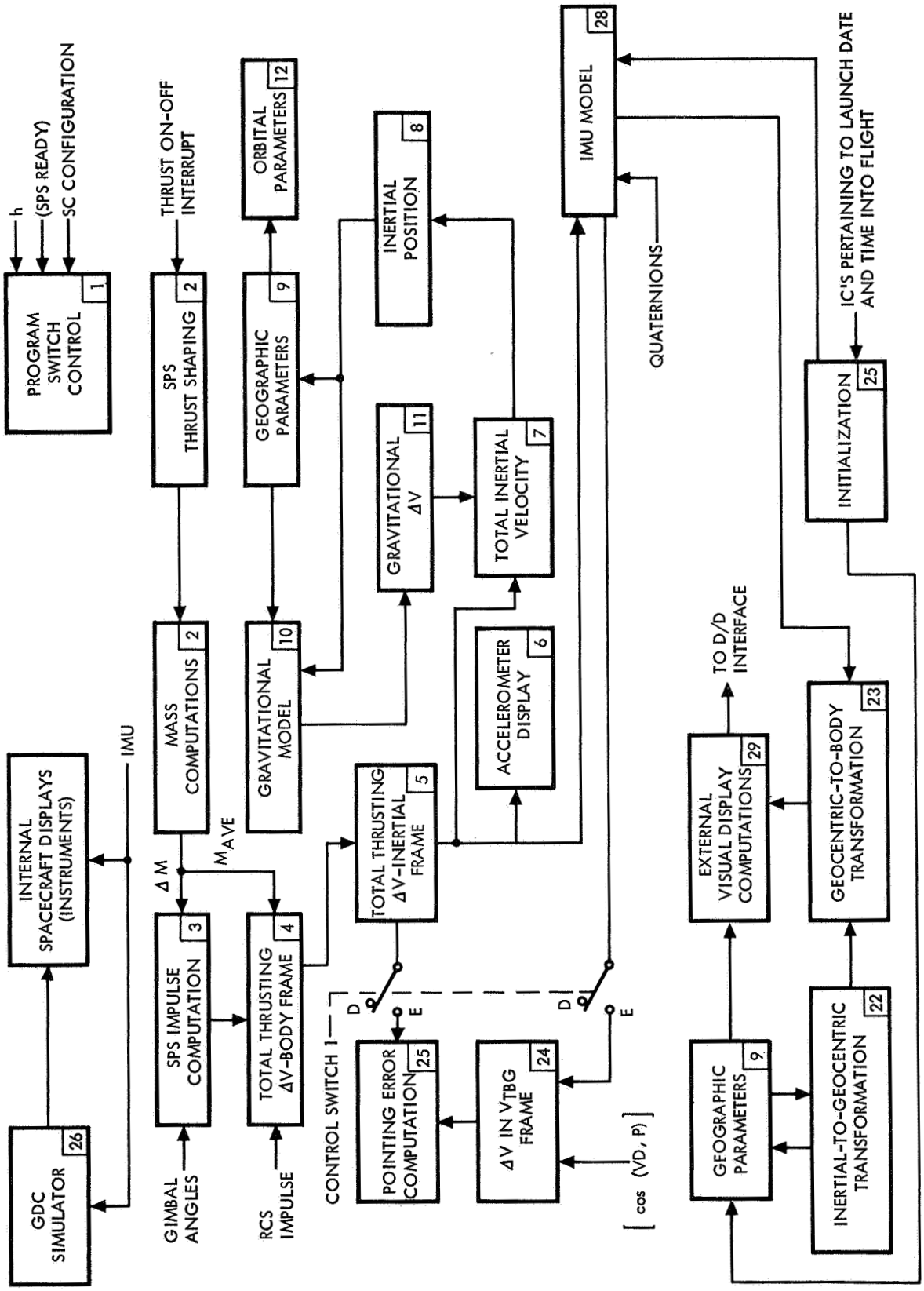

Figure 3-1. Flow Diagram of Digital Computations
(h > 400,000 Feet)

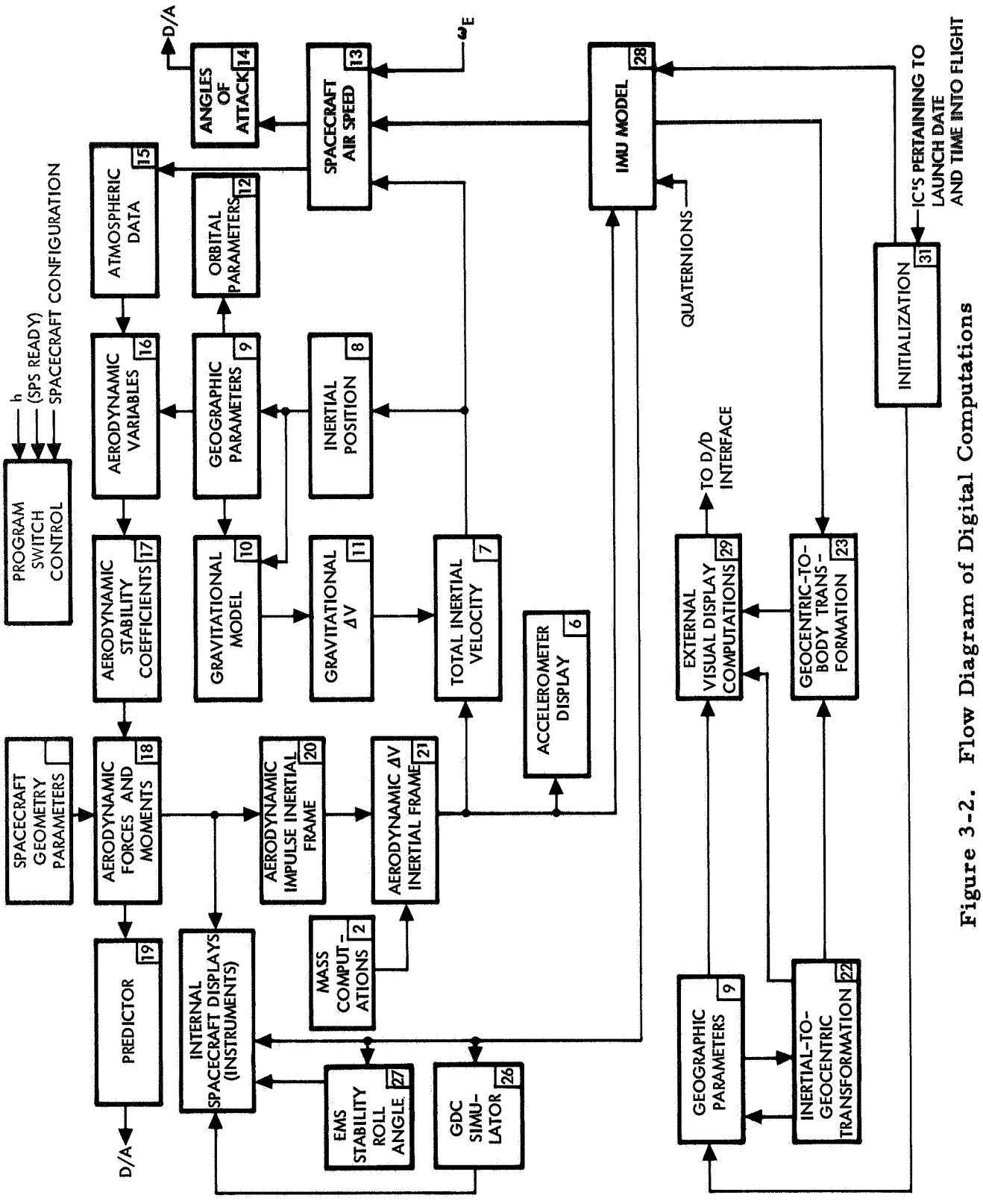

Figure 3-2. Flow Diagram of Digital Computations ($h < 400,000$ Feet)

Table 3-1. Miscellaneous Notations

Notation	Definition
$[\ \ ]$	A square matrix
$\{\ \ \}$	A column matrix (e.g., vector)
$\lfloor\ \ \rfloor$	A row matrix (e.g., vector)
Δ	When preceding a dynamic variable, the change in the variable during a single computation cycle.
$[\cos (B, P)]$	The direction cosine transformation matrix (represents the direction cosines generated by a rotation from the P-frame to the B-frame)
$\cos (B, P)_{ij}$	The direction cosine between the j-axis of the P-frame and the i-axis of the B-frame (i.e., the a_{ij} element of the $[\cos (B, P)]$ matrix)
Subscript "n"	The value during n^{th} computation cycle
$[\ \ ]^T$	The transpose of the matrix in brackets
$[\cos (B, P)^0]$	The value of matrix elements at time of initialization

Table 3-2. Subscripts* Defining Reference Frames

Reference Frame**	Definition
I	Nonrotating, origin at earth center, X-axis along vernal equinox, Z-axis through North Pole.
E	Fixed to rotating earth, origin at earth center, X-axis through prime meridian, z-axis through North Pole.
G	Rotates with spacecraft orbital position, origin at earth center, X-axis through spacecraft center of gravity, Y-axis in equatorial plane.
LG	Rotates with G-frame, origin at spacecraft center of gravity, X-axis points east, Y-axis points south, Z-axis points through earth center.
H	Rotating frame, origin at spacecraft center of gravity, Z-axis points through earth center, X-axis points in orbital velocity direction (horizontal component).
B	Rotates with spacecraft, origin at spacecraft center of gravity, X-axis parallel to axis of symmetry, positive toward command module apex, Z-axis through foot of couch. See Figure 2-1.
OB	Rotates with spacecraft, origin at spacecraft center of gravity, rotated from B-frame about Y_B axis by $\theta = +32.5231132°$.
SCT	Rotates with scanning telescope line of sight (LOS) when viewing stars, X-axis parallel to LOS. Frame is rotated from NB-frame by shaft and trunnion angles.
WLOS	Rotates with spacecraft, X-axis parallel to LOS through rendezvous window.
TLOS	Rotates with scanning telescope LOS when viewing earth, X-axis parallel to LOS.

Table 3-2. Subscripts* Defining Reference Frames (Cont)

Reference Frame**	Definition
PLOS	Rotates as optical probe gimbal biases are changed. Desired inertial LOS's are resolved in this frame.
SXT	Rotates with sextant trunnion, X-axis parallel to LOS (to star). Frame is rotated from NB-frame by shaft and trunnion angles.
BI	Nonrotating, origin at spacecraft center of gravity, axes coincide with B-frame at problem initiation.
P	Rotates with IMU platform. When all gimbals are zeroed, P - and B-frames are parallel.
PI	Nonrotating, axes coincide with P-frame at problem initiation.
PD	Rotates from P-frame to new P-frame orientation in succeeding computation cycle. Represents platform orientation change due to drift or fine alignment of platform.
LT	Rotates with earth, axes coincide with G-frame if spacecraft is at target landing point.
R	Rotating, similar to G-frame with passive rendezvous vehicle substituted for active spacecraft.
DI	Nonrotating, defined at FDAI alignment; i.e., the angles displayed on the FDAI may be considered the rotations from the DI-frame to the B-frame.

*Use symbols as superscripts and subscripts to Euler angle. The superscript defines the frame rotated from, and the subscript defines the frame rotated to. For example ψ_G^E is the geocentric longitude, and θ_G^E is latitude.

**Some of the subscripts listed are illustrated in Figure 3-3.

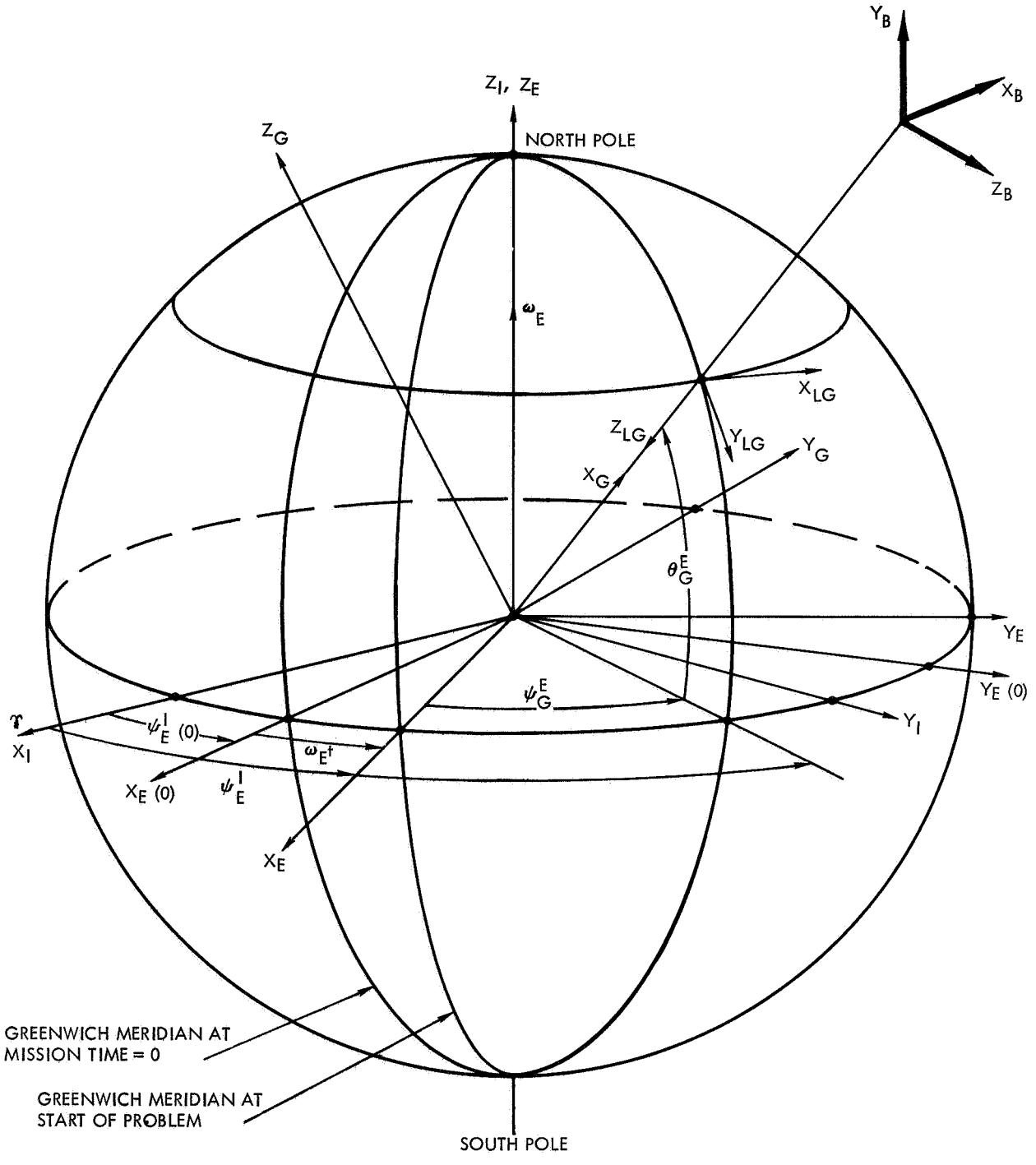

Figure 3-3. Coordinate Frame for Spacecraft State Vector Determination

Table 3-3. Mathematical Model Symbols

Components			Resultant	Definition
X	Y	Z	R	Position
$\dot{X}$	$\dot{Y}$	$\dot{Z}$	V	Velocity
$\ddot{X}$	$\ddot{Y}$	$\ddot{Z}$	$\ddot{R}$	Acceleration
F_X	F_Y	F_Z	F	Forces
	δ_θ	δ_ψ		Gimbal angles (SPS engine)
A_O	A_I	A_M		*Gimbal angles (outer, inner, and middle)
ϕ	θ	ψ		*Euler angles
$\dot{\phi}$	$\dot{\theta}$	$\dot{\psi}$		*Euler angle rates
ω_X	ω_Y	ω_Z	ω	Angular velocity
$\dot{\omega}_X$	$\dot{\omega}_Y$	$\dot{\omega}_Z$	$\dot{\omega}$	Angular acceleration
L_X	L_Y	L_Z	L	Moments
I_X	I_Y	I_Z	I	Impulse
P_X	P_Y	P_Z	P	Platform gyro error counter change per computation cycle
			M	Mass
			t	Running time reference
			T	Time interval

*Components are not along orthogonal axes.

Table 3-4. Superscripts to Dynamic Variables

Superscript	Definition
A	Due to aerodynamic loads
SPS	Due to SPS thrust
CM RCS	Due to command module RCS thrust
SM RCS	Due to service module RCS thrust
g	Due to earth gravity
S	Value sensed by instrument
P	Platform (IMU)

Note: These symbols are used to differentiate between sources of dynamic effects—e.g., F^A—force due to aerodynamic loads. The notation in this document is often inconsistent because many symbols for quantities have become traditional—e.g., $\bar{c}$, ω_E—and therefore were not redefined in this system of notation.

Table 3-5. Miscellaneous Variable Quantities

Symbol	Mnemonic	Description	Units
$\delta\theta_T$ $\delta\psi_T$		SPS gimbal trim angles	rad
ρ		Atmospheric density	slug/ft^3
V_S		Velocity of sound	ft/sec
V^A		True airspeed of spacecraft	ft/sec
$\bar{q}$		Dynamic pressure	lb/ft^2
MN		Mach number	ND
C_M		Aerodynamic pitching moment coefficient	ND
C_{NY}		Aerodynamic normal force coefficient	ND
C_A		Aerodynamic axial force coefficient	ND
D		Aerodynamic drag force	lb
L/D		Aerodynamic lift-to-drag ratio	ND
h		Altitude of spacecraft	ft
$V_{\omega E}$		Local geocentric earth velocity	ft/sec
V_g		Spacecraft velocity relative to non-rotating earth	ft/sec
D		Integer and fractional number of days from 1 July 1968 00.00 GMT	days
T		Time from launch	sec
ΔX_{CG}		$X_{CG} - X_{REF}$	inches
G		Total acceleration due to external loads	g's
G^A		Sensed acceleration along X-axis	g's
α, β		Y, Z rotation sequence to align X_B to velocity relative to air	rad
ϕ_A, α_T		-X, Y rotation sequence to align X_B to velocity relative to air	rad
γ_I		Angle $\vec{V}_I$ makes with local horizontal	rad
γ_g		Angle $\vec{V}_g$ makes with local horizontal	rad
ψ_H^{LG}		Angles $\vec{V}_I$ and $\vec{V}_g$ makes with east.	rad
R_g		Range to target	nm
T_g		Equatorial gravity coefficient	ND
T_{gZ}		Normal-to-equatorial gravity coefficient	ND
e_1 e_2 e_3 e_4		Quaternion elements	ND

Table 3-6. Miscellaneous Mathematical Model Constants

Symbol	Magnitude	Units	Description
I_{SP}	10131.6	lb-sec/slug	SPS engine specific impulse
M_{CM}	358.67	slugs	Mass of command module
S	129.4	ft^2	Aerodynamic reference area
$\bar{c}$	12.83	ft	Characteristic aerodynamic reference length
c_{LO}	0.0	ND	Aerodynamic rolling moment coefficient
X_{REF}	95.10	ft	Aerodynamic reference
ω_E	$7.29211504 \times 10^{-5}$	rad/sec	Earth rotation rate
R_E	20,925,741	ft	Earth radius at equator (Fisher)
f	1/298.3	ND	Earth Flattening coefficient (Fisher)
R_M	20,903,520	ft	Arithmetic mean of earth's radius at pole and equator
N_M	6076.1155	ft/nm	Foot-to-nautical mile conversion
μ	1.4076539×10^{16}	ft^3/sec^2	Earth gravitational constant
J	1.625×10^{-3}	ND	Earth main oblateness constant
H	5.750×10^{-6}	ND	Earth pear shape constant
κ	6.750×10^{-6}	ND	Earth second-order oblatness constant
π	3.1415927	ND	
X_{CG}	1040.8	inches	Command module center of gravity in spacecraft reference system
Y_{CG}	-0.4	inches	Command module center of gravity in spacecraft reference system
Z_{CG}	6.8	inches	Command module center of gravity in spacecraft reference system
ℓ_g	10.57	ft	Distance between engine attachment point and spacecraft center of gravity
C_A			Accelerometer errors (scale)
C_B			Accelerometer errors (bias)
K_p	5.21025641		Pulses per feet per second
K_e	0.01	ND	Coefficient defining drift rate in cage mode
K_C	0.01523	ND	Coefficient defining platform rate during coarse alignment
K_f	8.080808/50	ND	Quaternion feedback gain

3.1.1 Program Switch Control

The sequence of subroutines, i.e., computations, is dependent upon the condition of four switches. The logic for enabling each switch and its function are given in Table 3-7.

Table 3-7. Switch Enabling Logic and Functions

Switch No.	Logic	Function
1	Enable - SPS ready Disable - electrical thrust off plus 1.53 seconds	Switch 1A allows thrust on interrupt to be processed. Switches 1B and 1C permit calculation of pointing errors.
2	Enable - CSM configuration Disable - CM configuration	Switch 2A permits main engine impulse computations to be processed.
3	Enable - altitude less than 400,000 feet (Figure 3-2) Disable - altitude greater than 400,000 feet (Figure 3-1)	Switches 3A and 3B permit calculation of aerodynamic variables. Switch 3C changes computation of velocity in air from inertial velocity to geocentric velocity. Switches 3D and 3E change ΔV from thrusting to aerodynamic. Switch 3F changes G_A from thrusting to aerodynamic.
4	Enable - 0.05 g on Disable - 0.05 g off	Switch 4A switch GDC drive output.

3.1.2 Mass Computation and SPS Impulse

The response of a multiple-point digital integrator to a "near step" input was found to be unsatisfactory. This problem is circumvented by deriving the velocity increment from the propellant consumption. Propellant consumed-versus-time is analytically described as follows:

$$M(t) = [8.77193\, u_3(t - t_{ON} - 0.436)]\,[u_1(t - t_{ON} - 0.436) - u_1(t - t_{ON} - 0.55)]$$

$$+ u_2(t - t_{ON} - 0.55) - u_2(t - t_{OFF} - 0.27)$$

$$- [5.46247\, u_3(t - t_{OFF} - 0.27)]\,[u_1(t - t_{OFF} - 0.27) - u_1(t - t_{OFF} - 0.425)]$$

$$+ [0.1533 - 0.138763\, u_3(t - t_{OFF} - 0.425)]\,[u_1(t - t_{OFF} - 0.425) - u_1(t - t_{OFF} - 1.53)]$$

where

$$u_1(t) \triangleq \text{step} = \int \delta(t)$$

$$u_2(t) \triangleq \text{ramp} = \int u_1(t)dt$$

$$u_3(t) \triangleq \text{parabolic} = \int u_2(t)dt$$

t_{ON}; t_{OFF} = times at which electrical thrust-on and thrust-off commands occur

$$\Delta M_{(n)} = M_{(n+1)} - M_{(n)}$$

$$\Delta I_{(n)} = I_{sp}\, \Delta M_{(n)}$$

The ΔI computed is that change in impulse for the upcoming computational interval, so that it is really based on predicted values. This computation is desirable when PIPA information is computed.

3.1.3 SPS Impulse in Body Frame

The incremental impulse per computation cycle is transformed into components along spacecraft axes.

$$\left|\Delta I^{SPS}\right|_B = \Delta I^{SPS} \begin{Bmatrix} 1.0 - 0.5\,(\delta_\theta^2 + \delta_\psi^2) \\ \delta_\psi \\ -\delta_\theta \end{Bmatrix}$$

3.1.4 Total Velocity Change Due to RCS and SPS Forces

To measure the translational effects of the jets accurately, the jet forces (in the body frame) are integrated by analog integrators, and the output is sampled by the digital equations. The resultant impulse is determined by

$$\left|\Delta I^{RCS}_{(n)}\right|_B = \int_{t_o}^{t_n} \left|F^{RCS}\right|_B dt - \int_{t_o}^{t_{n-1}} \left|F^{RCS}\right|_B dt \qquad \text{(lb-sec)}$$

This impulse is divided by the average spacecraft mass during the sampling interval, which gives velocity change due to the RCS during the interval.

The impulse change lags by one computation interval (20 milliseconds). Since jet forces are small, the difference is completely negligible.

In an attempt to detect small velocity changes due to RCS jets and, at the same time, not overload the analog integrators during long-RCS on-times, two integrators were used per axis. Alternately, each integrator was zeroed. One integrator is in the zero state while the other is actively integrating. Digital logic performs the switching operation and approximately reduces the digital "past value" to zero. The switching interval (1.28 seconds) and the analog-to-digital scaling were selected to accommodate the extremes in RCS-induced velocity effectively.

$$M_{AVE} \left|\Delta V\right|_{B_{(n+1)}} = \left|\Delta I^{SPS}\right|_{B_{(n+1)}} + \left|\Delta I^{RCS}\right|_{B_{(n)}}$$

3.1.5 Transformation of Velocity Increment to Inertial Components

$$\left|\Delta V\right|_I = [\cos(B,I)]^T \left|\Delta V\right|_B$$

3.1.6 Accelerometer Input

The total inertial acceleration of the spacecraft is

$$\ddot{R} = \left(\Delta V_X^2 + \Delta V_Y^2 + \Delta V_Z^2\right)_I^{1/2} \Big/ \Delta t$$

For display on the EMS g-meter

$$G_A = (\Delta \dot{X})_B / \Delta t \qquad \text{for } h > 400,000 \text{ feet}$$

$$G_A = \left(F_X^A\right)_B / M_{CM} \qquad \text{for } h < 400,000 \text{ feet}$$

3.1.7 Total Inertial Velocity

The inertial velocity of the spacecraft during the $(n+1)^{th}$ computer frame is

$$\left|V\right|_{I_{(n+1)}} = \left|V\right|_{I_{(n)}} + \left|\Delta V\right|_{I_{(n+1)}} + \left|\Delta V^A\right|_{I_{(n)}} + \left|\Delta V^g\right|_{I_{(n)}}$$

3 1.8 Inertial Position

The inertial position of the spacecraft is obtained by a four-point Adams-Bashforth integration of the inertial velocity.

$$Y_{n+1} = Y_n + \Delta t \left(\frac{55}{44} Y'_n - \frac{59}{24} Y'_{n-1} + \frac{37}{24} Y'_{n-2} - \frac{9}{24} Y'_{n-3} \right)$$

where

Y_n = value of X, Y, or Z in the n^{th} computation interval.

Y'_n = value of $\dot{X}$, $\dot{Y}$, or $\dot{Z}$ in the n^{th} computation interval.

This results from a Taylor series expansion about Y_{n+1}.

3.1.9 Geographic Parameters

a Radial distance from earth center to spacecraft center of gravity

$$R = \left(X^2 + Y^2 + Z^2 \right)^{1/2}$$

b. Geocentric latitude

$$\sin \theta^E_G = Z/R$$

$$\cos \theta^E_G = \left(X^2 + Y^2 \right)^{1/2} / R$$

$$\theta^E_G = \tan^{-1} \left[Z / \left(X^2 + Y^2 \right)^{1/2} \right]$$

c. Total longitude angle from Aries

$$\sin \psi^I_E = Y / \left(X^2 + Y^2 \right)^{1/2}$$

$$\cos \psi^I_E = X / \left(X^2 + Y^2 \right)^{1/2}$$

$$\psi^I_E = \tan^{-1} (Y/X)$$

d. Geocentric longitude

$$\psi^E_G = \psi^I_G - \psi^I_E$$

where $$\psi_E^I = \psi_E^I(0) + \omega_E t$$

e. Geocentric altitude

$$h = R\left[1.0 - \left(\frac{R_E}{R}\right)\left(1.0 - f \sin^2 \theta_G^E\right)\right]$$

f. Inertial velocity in geocentric frame

$$\left\{V_I\right\}_G = [\cos (G, I)] \left\{V_I\right\}_I$$

$$V_I = \left(\dot{X}^2 + \dot{Y}^2 + \dot{Z}^2\right)^{1/2}$$

g. Geocentric velocity (velocity relative to rotating earth surface)

$$V_g = \left[\dot{X}_G^2 + \left(\dot{Y}_G - V_{\omega E}\right)^2 + \dot{Z}_G^2\right]^{1/2}$$

where $V_{\omega E} = R_{\omega E} \cos \theta_G^E$

h. Inertial flight path angle

$$\gamma_I = \sin^{-1}\left(\dot{X}_G / V_I\right)$$

i. Geocentric flight path angle

$$\gamma_g = \sin^{-1}\left(\dot{X}_G / V_g\right)$$

j. Inertial heading angle

$$\sin \psi_H^{LG} = \dot{Y}_G \Big/ \left[\left(\dot{Y}_G\right)^2 + \left(\dot{Z}_G\right)^2\right]^{1/2}$$

$$\cos \psi_H^{LG} = \dot{Z}_G \Big/ \left[\left(\dot{Y}_G\right)^2 + \left(\dot{Z}_G\right)^2\right]^{1/2}$$

$$\psi_H^{LG} = \tan^{-1}\left(\dot{Y}_G / \dot{Z}_G\right)$$

k. Geocentric heading angle

$$V_{EF} = \tan^{-1}\left[\left(\dot{Y}_G - V_{\omega E}\right) \Big/ \dot{Z}_G\right]$$

l. Orbit inclination

$$\cos i = \sin \psi_H^{LG} \cos \theta_G^E$$

m. Range to target

$$R_g = \frac{R_M}{N_M} \left\{ \cos^{-1} \left[\sin \theta_G^E \sin \theta_{LT}^E + \cos \theta_G^E \cos \theta_{LT}^E \cdot \cos \left(\psi_E^I - \psi_E^I(0) - \psi_{LT}^E \right) \right] \right\}$$

n. Geographic nomenclature

R_M = earth mean radius = R_{PAD} = 20, 909, 806. 5808 ft

N_M = 6076. 1155 ft/nautical mile

$\theta_{LT}^E, \psi_{LT}^E$ = geocentric target coordinates

f = earth flattening = 1/298. 3

ω_E = 0. 729211504 x 10^{-4} rad/sec

3. 1. 10 Gravitational Model

The gravity components in the geocentric frame are computed as follows.

$$\left| \ddot{R}^g \right|_G = - \frac{\mu}{R^3} \begin{bmatrix} T_g & 0 & 0 \\ 0 & T_g & 0 \\ 0 & 0 & T_{gZ} \end{bmatrix} \left| R \right|_G$$

$$T_g = 1.0 - J\left(\frac{R_E}{R}\right)^2 P_2 - H\left(\frac{R_E}{R}\right)^3 P_3 + \kappa\left(\frac{R_E}{R}\right)^4 P_4$$

$$T_{gZ} = T_g + \frac{1}{Z}\left[2JZ\left(\frac{R_E}{R}\right)^2 + 0.6\, HR\left(\frac{R_E}{R}\right)^3 P_2 + \frac{\kappa Z}{6}\left(\frac{R_E}{R}\right)^4 \left(6.4 - 5.6\, P_2\right) \right]$$

and

$$P_2 = 5 \sin^2 \theta_L - 1$$

$$P_3 = 7 \sin^3 \theta_L - 3 \sin \theta_L$$

$$P_4 = \frac{1}{6}\left(63 \sin^4 \theta_L - 42 \sin^2 \theta_L + 3\right)$$

and

$$J = 1.623 \times 10^{-3}$$

$$H = 5.75 \times 10^{-6}$$

$$\kappa = 6.75 \times 10^{-6}$$

3.1.11 Gravitational ΔV

The change in spacecraft inertial velocity due to gravitation only is computed from the gravity acceleration components in the geocentric frame, producing incremental velocity components per computer frame.

The frequencies found in the gravity force equations are so low that, at 20 millisecond computation intervals, a rectangular integrator is sufficiently accurate.

3.1.12 Orbital Parameters

a. Angular momentum

$$\ell = RV_I \cos \gamma_I$$

b. Total energy

$$e = \frac{1}{2} V_I^2 - \mu/R$$

c. Semi-latus pectum

$$p = \ell^2/\mu$$

d. Major axis

$$a = -\mu/2\epsilon$$

e. Eccentricity

$$\epsilon = (1.0 - p/a)^{1/2}$$

f. Minor axis

$$b = (pa)^{1/2} = a\left(1.0 - \epsilon^2\right)^{1/2}$$

g. Orbit period

$$T_0 = 2\pi a\,(a/\mu)^{1/2}$$

h. Apogee distance

$$R_A = P/(1-\epsilon)$$

i. Perigee distance

$$R_P = P/(1+\epsilon)$$

j. Apogee distance above earth surface

$$H_A = \left(R_A - R_{PAD}\right)\Big/N_M$$

k. Perigee distance above earth surface

$$H_P - \left(R_P - R_{PAD}\right)\Big/N_M$$

l. True anomaly angle (measured from perigee)

$$f = \left\{\cos^{-1}\left[(p-R)/\epsilon R\right]\right\} \text{ sign } \dot{X}_G$$

m. Eccentric anomaly angle

$$E = \left\{\cos^{-1}\left[(a-R)/\epsilon a\right]\right\} \text{ sign } \dot{X}_G$$

n. Longitude of ascending node

$$\Omega = \psi_G^E - \tan^{-1}\left(\tan \psi_H^{LG} \sin \theta_G^E\right)$$

o. Argument of latitude

$$C = \tan^{-1}\left(\tan \theta_G^E \cos \psi_H^{LG}\right)$$

p. Argument of perigee

$$\omega = C - f$$

q. Orbital constants

$$\mu = 1.4076539 \times 10^{16} \text{ ft}^3/\text{sec}^2$$

$$\pi = 3.1415927$$

$$R_{PAD} = 6373322.44 \text{ km} = 20,909,806.5808 \text{ ft}$$

$$N_M = 6076.1155 \text{ ft/nautical mile}$$

3.1.13 Spacecraft Air Speed

The inertial velocity of the spacecraft resolved into components along the spacecraft axes (body frame) is

$$\left|V_I\right|_B = [\cos (B, I)] \left|V_I\right|_I$$

If the spacecraft is below 400,000 feet, the velocity of the spacecraft with respect to the surrounding air mass is calculated.

$$\left|V^A\right|_B = [\cos (B, I)] \begin{Bmatrix} \dot{X} + \omega_E Y \\ \dot{Y} - \omega_E X \\ \dot{Z} \end{Bmatrix}_I = \begin{Bmatrix} u \\ v \\ w \end{Bmatrix}$$

where

ω_E is the earth rotation rate in radians per second

3.1.14 Angles of Attack

$$\alpha = \tan^{-1}\left(\frac{w}{u}\right)$$

$$\beta = \tan^{-1}\left(\frac{v}{w^2 + u^2}\right)^{1/2}$$

3.1.15 Atmospheric Data

Data on the density and speed of sound-versus-altitude are stored in tabular form in the computer memory. The data are based on the 1962 U.S. Standard Atmosphere. Table 3-8 is the exact table stored in the computer.

$$\rho \triangleq \text{air density}$$

$$V_s \triangleq \text{speed of sound}$$

3 1.16 Aerodynamic Variables

$$V^A = \left(u^2 + v^2 + w^2\right)^{1/2}$$

$$\bar{q} = 0.5 \ \rho V_A^2$$

$$MN = V_A / V_S$$

$$\phi_A = \tan^{-1}(v/w)$$

$$\alpha_T = \tan^{-1}\left(\frac{\left(v^2 + w^2\right)^{1/2}}{u}\right)$$

$$\sin \phi_A = \frac{v}{\left(v^2 + w^2\right)^{1/2}}$$

$$\cos \phi_A = \frac{w}{\left(v^2 + w^2\right)^{1/2}}$$

Refer to Figure 3-4 for command module axes, aerodynamic coefficients, and notation system.

Table 3-8. Atmospheric Data Stored in Memory

Altitude (h), feet	Air Density (ρ), slugs/ft^3	Velocity of Sound (V_S), ft/sec
406,000	0.27747E-10	894.50
389,000	0.54516E-10	894.50
374,000	0.10012E-09	894.50
361,000	0.18388E-09	894.50
347,000	0.35224E-09	894.50
334,000	0.68001E-09	894.50
321,000	0.13701E-08	894.50
311,000	0.23801E-08	894.50
301,000	0.42481E-08	894.50
290,000	0.80604E-08	884.00
278,500	0.15367E-07	884.00
269,500	0.25861E-07	884.00
262,500	0.38338E-07	884.00
254,000	0.57814E-07	908.20
245,500	0.85388E-07	932.04
237,000	0.12375E-06	955.25
228,500	0.17628E-06	977.93
220,000	0.24726E-06	1000.10
211,000	0.34832E-06	1023.10
202,000	0.48361E-06	1045.50
192,000	0.70459E-06	1057.80
182,000	0.10180E-05	1069.90
172,000	0.14594E-05	1082.00
164,000	0.19757E-05	1082.00
155,500	0.27264E-05	1082.00
147,000	0.38798E-05	1067.90
138,500	0.55796E-05	1053.30
130,000	0.81089E-05	1038.50
121,500	0.11918E-04	1023.50
113,500	0.17311E-04	1009.00
105,500	0.25425E-04	994.51
97,500	0.36933E-04	989.25
89,500	0.53879E-04	983.95
81,500	0.78947E-04	978.62
73,500	0.11620E-03	973.25
66,000	0.16765E-03	968.08
58,500	0.23996E-03	968.08
51,000	0.34346E-03	968.08
43,500	0.49171E-03	968.08
36,000	0.70319E-03	968.08
28,000	0.94843E-03	1033.40
20,000	0.12546E-02	1036.90

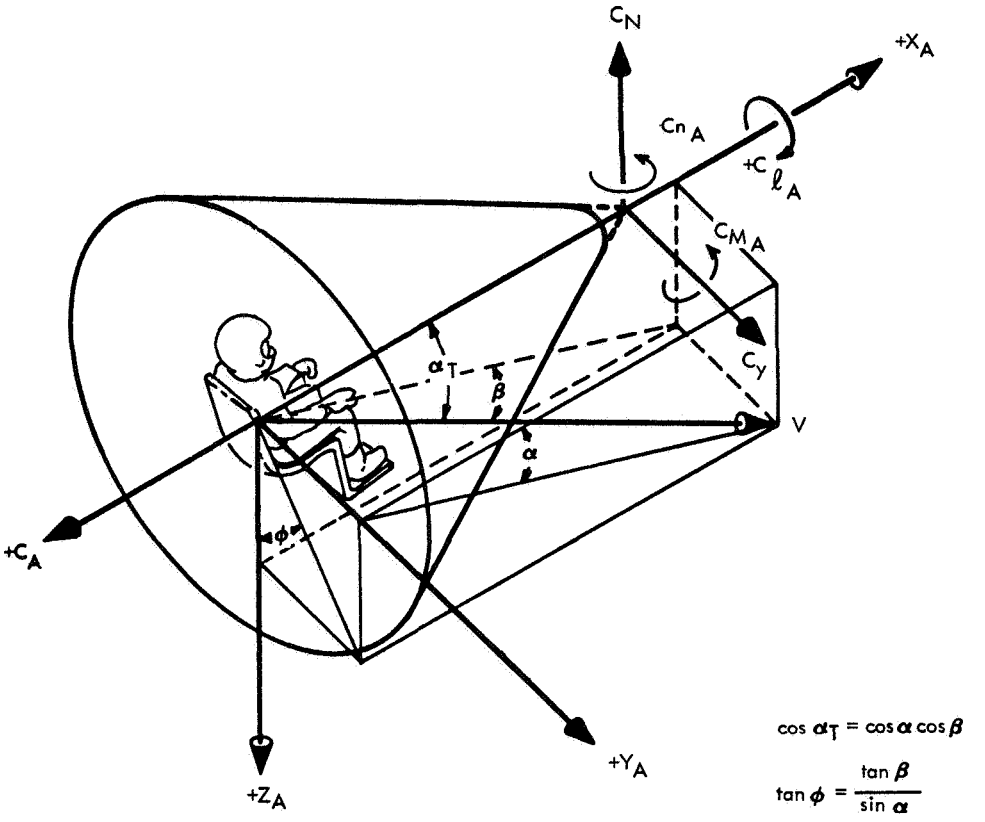

C_A	AXIAL FORCE COEFFICIENT (BODY AXIS), AXIAL FORCE/q_∞ S
$C_{\ell A}$	ROLLING MOMENT COEFFICIENT, ABOUT THE X AXIS AND THROUGH THE THEORETICAL CONE APEX (BODY AXIS), ROLLING MOMENT/q_∞ Sd
C_{M_A}	PITCHING MOMENT COEFFICIENT, ABOUT A LINE PARALLEL TO THE Y AXIS AND THROUGH THE THEORETICAL CONE APEX (BODY AXIS), PTICHING MOMENT/q_∞Sd
C_N	NORMAL FORCE COEFFICIENT (BODY AXIS), NORMAL FORCE/q_∞ S
C_{n_A}	YAWING MOMENT COEFFICIENT, ABOUT A LINE PARALLEL TO THE Z AXIS AND THROUGH THE THEORETICAL CONE APEX (BODY AXIS), YAWING MOMENT/q_∞ Sd
C_Y	SIDE FORCE COEFFICIENT (BODY AXIS), SIDE FORCE/q_∞S
$C_{M_q} + C_{M_{\dot\alpha}}$	PITCH DAMPING COEFFICIENT, PER RADIAN
$C_{n_r} + C_{n_{\dot\beta}}$	YAW DAMPING COEFFICIENT, PER RADIAN
α	ANGLE OF ATTACK, DEGREES
α_T	TOTAL ANGLE OF ATTACK, DEGREES
β	ANGLE OF SIDESLIP, DEGREES
ϕ	ROLL ANGLE, DEGREES
d	REFERENCE LENGTH = 154 INCHES
S	REFERENCE AREA = 129.35 SQUARE FEET
V	FREESTREAM VELOCITY, FEET PER SECOND
q_∞	DYNAMIC PRESSURE, POUNDS PER SQUARE FOOT
q	PITCH RATE, DEGREES PER SECOND

Figure 3-4. Command Module Axes, Aerodynamic Coefficients, and Notation System

3.1.17 Aerodynamic Stability Coefficients

A table is stored in the computer memory which gives C_A, C_{NY}, and C_M versus Mach number and angle of attack. This complete table is presented in Table 3-9.

3.1.18 Aerodynamic Forces and Moments

The forces acting on the spacecraft resolved along the spacecraft axes (body frame) are

$$\left|F^A\right|_B = -\bar{q}S\begin{Bmatrix} C_A \\ C_{NY}\sin\phi_A \\ C_{NY}\cos\phi_A \end{Bmatrix}$$

The drag force is

$$D = \bar{q}S\left(C_{NY}\sin\alpha_T + C_A\cos\alpha_T\right)$$

The lift-to-drag ratio is

$$L/D = \frac{C_{NY}\cos\alpha_T - C_A\sin\alpha_T}{C_{NY}\sin\alpha_T + C_A\cos\alpha_T}$$

The moments about the spacecraft axes due to aerodynamic loads are

$$\left|L^A\right|_B = -\bar{q}S\begin{Bmatrix} C_{NY}\left[Z_{CG}\sin\phi_A - Y_{CG}\cos\phi_A\right] - \bar{c}\,c_{LO} \\ -\cos\phi_A\left[\bar{c}\,C_M + C_{NY}\left(X_{REF} - X_{CG}\right) - C_A Z_{REF}\right] - C_A Z_{CG} \\ \sin\phi_A\left[\bar{c}\,C_M + C_{NY}\left(X_{REF} - X_{CG}\right) - C_A Z_{REF}\right] + C_A Y_{CG} \end{Bmatrix}$$

Table 3-9. Aerodynamic Stability Coefficients Stored in Memory

M_n	α_T	C_A	C_{NY}	C_M
0.40	180.1364	-0.87000	-0.00210	0.00330
0.40	175.1365	-0.87000	-0.01710	0.02500
0.40	170.1365	-0.87990	-0.03210	0.04800
0.40	165.1365	-0.88990	-0.06210	0.08130
0.40	160.1365	-0.89980	-0.09210	0.11950
0.40	155.1365	-0.89980	-0.10210	0.15340
0.40	150.1365	-0.85480	-0.09200	0.15570
0.40	145.1365	-0.79990	-0.05690	0.13620
0.40	140.1365	-0.74000	0.01180	0.10490
0.40	135.1365	-0.66010	0.02840	0.07280
0.40	130.1365	-0.59020	0.06860	0.04090
0.40	120.1365	-0.36040	0.14910	-1.03270
0.40	110.1365	-0.04050	0.20990	-0.10410
0.40	100.0000	0.10000	0.25200	-0.16560
0.40	90.0000	0.23000	0.26600	-0.22970
0.40	80.0000	0.30000	0.22100	-0.23640
0.40	70.0000	0.12000	0.05800	-0.13040
0.40	60.0000	0.21000	0.17900	-0.16960
0.40	50.0000	0.11000	0.43800	-0.29610
0.40	40.0000	0.20000	0.44800	-0.30070
0.40	30.0000	0.31000	0.36800	-0.24550
0.40	20.0000	0.42000	0.26700	-0.17360
0.40	10.0000	0.51000	0.14800	-0.09530
0.40	0.0000	0.54800	0.00000	-0.00000
0.70	180.1364	-0.98000	-0.00230	0.00380
0.70	175.1365	-1.00990	-0.02740	0.03270
0.70	170.1365	-1.01990	-0.02240	0.04190
0.70	165.1365	-1.02200	-0.00760	0.03330
0.70	160.1365	-1.00010	0.02760	0.03040
0.70	155.1365	-0.98010	0.03270	0.03850
0.70	150.1365	-0.95010	0.02270	0.06030
0.70	145.1365	-0.91000	0.01780	0.08340
0.70	140.1365	-0.86010	0.02800	0.08590
0.70	135.1365	-0.79010	0.05310	0.06780
0.70	130.1365	-0.67020	0.09840	0.03120
0.70	120.1365	-0.38050	0.19410	-0.05440
0.70	110.1365	-0.06060	0.26990	-0.13820

Table 3-9. Aerodynamic Stability Coefficients Stored in Memory (Cont)

M_n	α_T	C_A	C_{NY}	C_M
0.70	100.0000	0.17000	0.31800	-0.20940
0.70	90.0000	0.34000	0.31500	-0.25340
0.70	80.0000	0.51000	0.29600	-0.30300
0.70	70.0000	0.59000	0.32300	-0.30350
0.70	60.0000	0.19000	0.55000	-0.38520
0.70	50.0000	0.10600	0.58000	-0.37700
0.70	40.0000	0.23400	0.50000	-0.33440
0.70	30.0000	0.35800	0.40900	-0.27410
0.70	20.0000	0.50400	0.29600	-0.19720
0.70	10.0000	0.61500	0.16000	-0.10660
0.70	0.0000	0.64600	0.00000	-0.00000
0.90	180.1364	-1.09000	-0.00260	0.00420
0.90	175.1365	-1.10100	-0.01260	0.01710
0.90	170.1365	-1.11500	-0.00270	0.02710
0.90	165.1365	-1.12000	-0.01730	0.02460
0.90	160.1365	-1.10510	0.03540	0.02330
0.90	155.1365	-1.07510	0.05240	0.02120
0.90	150.1365	-1.04520	0.06750	0.02090
0.90	145.1365	-0.99020	0.07560	0.02450
0.90	140.1365	-0.93520	0.08480	0.03130
0.90	135.1365	-0.87030	0.11190	0.02160
0.90	130.1365	-0.76040	0.16320	-0.01290
0.90	120.1365	-0.45070	0.28890	-0.11550
0.90	110.1365	-0.11000	0.41770	-0.23660
0.90	100.0000	0.15500	0.46900	-0.30080
0.90	90.0000	0.39500	0.48500	-0.35880
0.90	80.0000	0.57000	0.46700	-0.39690
0.90	70.0000	0.54100	0.46600	-0.37450
0.90	60.0000	0.21800	0.62400	-0.43290
0.90	50.0000	0.21200	0.66800	-0.43790
0.90	40.0000	0.31100	0.57500	-0.38570
0.90	30.0000	0.45600	0.43900	-0.29820
0.90	20.0000	0.59500	0.28900	-0.19380
0.90	10.0000	0.69800	0.14000	-0.09500
0.90	0.0000	0.71900	0.00000	-0.00000
1.10	180.1364	-1.30500	-0.00310	0.00500
1.10	175.1365	-1.31500	-0.01310	0.01550
1.10	170.1365	-1.31500	0.00190	0.02120

Table 3-9. Aerodynamic Stability Coefficients Stored in Memory (Cont)

M_n	α_T	C_A	C_{NY}	C_M
1.10	165.1365	-1.30510	0.02190	0.01780
1.10	160.1365	-1.29010	0.03490	0.01890
1.10	155.1365	-1.27010	0.04900	0.01700
1.10	150.1365	-1.24020	0.06500	0.01610
1.10	145.1365	-1.21020	0.08710	0.01600
1.10	140.1365	-1.16840	0.14620	-0.01420
1.10	135.1365	-1.08160	0.23040	-0.06860
1.10	135.1365	-0.94880	0.31870	-0.13550
1.10	120.1365	-0.60110	0.45360	-0.25470
1.10	110.1365	-0.29630	0.54530	-0.33360
1.10	100.0000	-0.02200	0.61300	-0.38780
1.10	90.0000	0.23000	0.65500	-0.44010
1.10	80.0000	0.49100	0.66000	-0.48290
1.10	70.0000	0.56100	0.66800	-0.50050
1.10	60.0000	0.40300	0.74000	-0.52090
1.10	50.0000	0.40800	0.70200	-0.48350
1.10	40.0000	0.49700	0.56500	-0.38740
1.10	30.0000	0.72000	0.41700	-0.28690
1.10	20.0000	0.91800	0.27200	-0.19040
1.10	10.0000	0.99900	0.12500	-0.09060
1.10	0.0000	1.05100	0.00000	-0.00000
1.20	180.1364	-1.32500	-0.00320	0.00510
1.20	175.1365	-1.32000	-0.00110	0.01540
1.20	170.1365	-1.31000	0.00690	0.01840
1.20	165.1365	-1.30010	0.02190	0.01750
1.20	160.1365	-1.28010	0.03700	0.01640
1.20	155.1365	-1.25010	0.05200	0.01470
1.20	150.1365	-1.23020	0.06210	0.01850
1.20	145.1365	-1.20720	0.08710	0.01490
1.20	140.1365	-1.16140	0.15420	-0.02320
1.20	135.1365	-1.08660	0.23340	-0.07430
1.20	130.1365	-0.96080	0.32070	-0.13870
1.20	120.1365	-0.63310	0.46150	-0.25890
1.20	110.1365	-0.31130	0.55430	-0.34180
1.20	100.0000	-0.03000	0.62000	-0.39560
1.20	90.0000	0.22000	0.67000	-0.45370
1.20	80.0000	0.46500	0.69600	-0.50280
1.20	70.0000	0.57700	0.70500	-0.52350
1.20	60.0000	0.44900	0.76200	-0.53850

Table 3-9. Aerodynamic Stability Coefficients Stored in Memory (Cont)

M_n	α_T	C_A	C_{NY}	C_M
1.20	50.0000	0.47200	0.70500	-0.48930
1.20	40.0000	0.58100	0.58000	-0.40110
1.20	30.0000	0.76400	0.39500	-0.27260
1.20	20.0000	0.93900	0.24000	-0.16640
1.20	10.0000	1.02800	0.11700	-0.08190
1.20	0.0000	1.05000	0.00000	-0.00000
1.35	180.1364	-1.42000	-0.00340	0.00550
1.35	175.1365	-1.42000	0.00660	0.00930
1.35	170.1365	-1.41500	0.00960	0.01700
1.35	165.1365	-1.41010	0.02160	0.01840
1.35	160.1365	-1.40510	0.03670	0.01770
1.35	155.1365	-1.40010	0.05170	0.01810
1.35	150.1365	-1.37020	0.07170	0.01490
1.35	145.1365	-1.31030	0.13190	-0.01770
1.35	140.1365	-1.22050	0.20710	-0.06150
1.35	135.1365	-1.10070	0.28240	-0.11120
1.35	130.1365	-0.96090	0.35770	-0.16720
1.35	120.1365	-0.63110	0.48150	-0.27310
1.35	110.1365	-0.32140	0.57420	-0.35600
1.35	100.0000	-0.04000	0.64000	-0.41110
1.35	90.0000	0.20000	0.68500	-0.46620
1.35	80.0000	0.43500	0.70500	-0.50460
1.35	70.0000	0.54600	0.72000	-0.52980
1.35	60.0000	0.52600	0.76000	-0.54170
1.35	50.0000	0.55800	0.70100	-0.49160
1.35	40.0000	0.64900	0.57900	-0.40240
1.35	30.0000	0.78500	0.40800	-0.28110
1.35	20.0000	0.94600	0.26100	-0.17860
1.35	10.0000	1.05000	0.12700	-0.08750
1.35	0.0000	1.09200	0.00000	-0.00000
1.65	180.1364	-1.45000	-0.00350	0.00560
1.65	175.1365	-1.44200	0.00260	0.01100
1.65	170.1365	-1.44000	0.01260	0.01350
1.65	165.1365	-1.43010	0.02460	0.01460
1.65	160.1365	-1.42010	0.04160	0.01320
1.65	155.1365	-1.39020	0.06700	0.00610

Table 3-9. Aerodynamic Stability Coefficients Stored in Memory (Cont)

M_n	α_T	C_A	C_{NY}	C_M
1.65	150.1365	-1.35020	0.10180	-0.00750
1.65	145.1365	-1.27030	0.14400	-0.02950
1.65	140.1365	-1.18050	0.20420	-0.06590
1.65	135.1365	-1.06060	0.26450	-0.10680
1.65	130.1365	-0.92080	0.32780	-0.15300
1.65	120.1365	-0.61310	0.44850	-0.25000
1.65	110.1365	-0.31130	0.53830	-0.33230
1.65	100.0000	-0.03700	0.61200	-0.39780
1.65	90.0000	0.20000	0.65100	-0.44820
1.65	80.0000	0.40100	0.67100	-0.47960
1.65	70.0000	0.53900	0.69400	-0.50430
1.65	60.0000	0.61300	0.71200	-0.51430
1.65	50.0000	0.65500	0.68800	-0.48860
1.65	40.0000	0.74400	0.59100	-0.41710
1.65	30.0000	0.83300	0.46700	-0.32440
1.65	20.0000	0.92600	0.32600	-0.22290
1.65	10.0000	1.02000	0.16460	-0.11110
1.65	0.0000	1.09300	0.00000	-0.00000
2.00	180.1364	-1.47200	-0.00350	0.00560
2.00	175.1365	-1.47100	-0.00150	0.01360
2.00	170.1365	-1.46700	0.00650	0.01880
2.00	165.1365	-1.45300	0.01850	0.01970
2.00	160.1365	-1.43610	0.04660	0.01080
2.00	155.1365	-1.40220	0.08470	-0.00500
2.00	150.1365	-1.32530	0.12180	-0.02230
2.00	145.1365	-1.22940	0.15910	-0.04240
2.00	140.1365	-1.10550	0.20240	-0.06830
2.00	135.1365	-0.98960	0.25360	-0.10270
2.00	130.1365	-0.86070	0.30600	-0.13960
2.00	120.1365	-0.58700	0.41360	-0.22500
2.00	110.1365	-0.29320	0.50930	-0.31300
2.00	100.0000	-0.02300	0.59800	-0.39210
2.00	90.0000	0.21700	0.65000	-0.45100
2.00	80.0000	0.40600	0.69500	-0.49810
2.00	70.0000	0.53100	0.72500	-0.52330
2.00	60.0000	0.60600	0.72500	-0.52220
2.00	50.0000	0.67200	0.69000	-0.49090
2.00	40.0000	0.73300	0.62200	-0.43750
2.00	30.0000	0.79300	0.51500	-0.35850

Table 3-9. Aerodynamic Stability Coefficients Stored in Memory (Cont)

M_n	α_T	C_A	C_{NY}	C_M
2.00	20.0000	0.86300	0.37500	-0.26040
2.00	10.0000	0.91700	0.21100	-0.14400
2.00	0.0000	0.95000	0.00000	-0.00000
2.40	180.1364	-1.47000	-0.00350	0.00560
2.40	175.1365	-1.46500	0.00650	0.00720
2.40	170.1365	-1.45500	0.01850	0.00880
2.40	165.1365	-1.44010	0.03660	0.00790
2.40	160.1365	-1.40510	0.05870	0.00260
2.40	155.1365	-1.35820	0.08680	-0.00670
2.40	150.1365	-1.28030	0.12200	-0.02370
2.40	145.1365	-1.19040	0.15920	-0.04330
2.40	140.1365	-1.08050	0.19740	-0.06440
2.40	135.1365	-0.96060	0.24270	-0.09390
2.40	130.1365	-0.83070	0.28300	-0.12220
2.40	120.1365	-0.56090	0.37170	-0.19420
2.40	110.1365	-0.28110	0.47430	-0.28710
2.40	100.0000	-0.00000	0.57000	-0.37500
2.40	90.0000	0.22000	0.63000	-0.43910
2.40	80.0000	0.39000	0.67500	-0.48160
2.40	70.0000	0.51000	0.70000	-0.50460
2.40	60.0000	0.59500	0.71000	-0.51090
2.40	50.0000	0.65100	0.68000	-0.48290
2.40	40.0000	0.69800	0.63000	-0.44230
2.40	30.0000	0.77100	0.54500	-0.38160
2.40	20.0000	0.81700	0.41600	-0.29090
2.40	10.0000	0.85300	0.23200	-0.16740
2.40	0.0000	0.86200	0.00000	-0.00000
3.00	180.1364	-1.47500	-0.00350	-0.00570
3.00	175.1365	-1.47000	0.01450	0.00250
3.00	170.1365	-1.45010	0.03150	0.01100
3.00	165.1365	-1.42010	0.04760	0.00060
3.00	160.1365	-1.38020	0.06970	-0.00360
3.00	155.1365	-1.32020	0.09490	-0.01260
3.00	150.1365	-1.23030	0.12210	-0.02430
3.00	145.1365	-1.14040	0.15730	-0.04160
3.00	140.1365	-1.03040	0.18750	-0.05770
3.00	135.1365	-0.92050	0.22280	-0.07870
3.00	130.1365	-0.80060	0.25810	-0.10280

Table 3-9. Aerodynamic Stability Coefficients Stored in Memory (Cont)

M_n	α_T	C_A	C_{NY}	C_M
3.00	120.1365	-0.52080	0.33880	-0.17000
3.00	110.1365	-0.25100	0.43940	-0.26290
3.00	100.0000	0.02000	0.53000	-0.35510
3.00	90.0000	0.23000	0.59500	-0.41600
3.00	80.0000	0.38000	0.64500	-0.46070
3.00	70.0000	0.49000	0.68000	-0.48990
3.00	60.0000	0.57000	0.68800	-0.49450
3.00	50.0000	0.62500	0.67200	-0.47650
3.00	40.0000	0.66000	0.62500	-0.43820
3.00	30.0000	0.68500	0.55300	-0.38860
3.00	20.0000	0.71500	0.43000	-0.30590
3.00	10.0000	0.76000	0.23800	-0.17200
3.00	0.0000	0.77000	0.00000	-0.00000
4.00	180.1364	-1.46000	-0.00350	0.00560
4.00	175.1365	-1.45400	0.01160	0.00330
4.00	170.1365	-1.43410	0.02910	0.00270
4.00	165.1365	-1.39610	0.04790	0.00130
4.00	160.1365	-1.34120	0.06930	-0.00230
4.00	155.1365	-1.27520	0.09300	-0.00900
4.00	150.1365	-1.19030	0.12020	-0.01990
4.00	145.1365	-1.09240	0.14640	-0.03190
4.00	140.1365	-0.98640	0.17270	-0.04540
4.00	135.1365	-0.87650	0.20390	-0.06490
4.00	130.1365	-0.75560	0.23220	-0.08500
4.00	120.1365	-0.48870	0.30680	-0.14950
4.00	110.1365	-0.20690	0.39350	-0.23400
4.00	100.0000	0.05700	0.47500	-0.31400
4.00	90.0000	0.25400	0.54100	-0.38090
4.00	80.0000	0.38800	0.59200	-0.42530
4.00	70.0000	0.47500	0.63200	-0.45650
4.00	60.0000	0.53900	0.64700	-0.46500
4.00	50.0000	0.58800	0.63600	-0.45190
4.00	40.0000	0.62000	0.61300	-0.43220
4.00	30.0000	0.64400	0.55300	-0.39150
4.00	20.0000	0.67000	0.43900	-0.31280
4.00	10.0000	0.69300	0.23500	-0.16950
4.00	0.0000	0.70000	0.00000	-0.00000

Table 3-9. Aerodynamic Stability Coefficients Stored in Memory (Cont)

M_n	α_T	C_A	C_{NY}	C_M
6.00	180.1364	-1.49000	-0.00350	0.01370
6.00	175.1365	-1.48400	0.01150	0.01290
6.00	170.1365	-1.46110	0.03050	0.01140
6.00	165.1365	-1.41380	0.05260	0.00830
6.00	160.1365	-1.34520	0.07480	0.00330
6.00	155.1365	-1.26720	0.09600	-0.00160
6.00	150.1365	-1.17630	0.12020	-0.01030
6.00	145.1365	-1.08280	0.14240	-0.01940
6.00	140.1365	-0.97940	0.16870	-0.03380
6.00	135.1365	-0.86340	0.18190	-0.04100
6.00	130.1365	-0.73350	0.19830	-0.05470
6.00	120.1365	-0.47060	0.27090	-0.11780
6.00	110.1365	-0.18790	0.36860	-0.20990
6.00	100.0000	0.06000	0.45900	-0.30340
6.00	90.0000	0.26300	0.54300	-0.38270
6.00	80.0000	0.38300	0.59700	-0.42840
6.00	70.0000	0.46900	0.63800	-0.46020
6.00	60.0000	0.54400	0.65200	-0.46860
6.00	50.0000	0.59100	0.65000	-0.46310
6.00	40.0000	0.62400	0.63800	-0.45290
6.00	30.0000	0.62200	0.57600	-0.40930
6.00	20.0000	0.64300	0.46300	-0.33150
6.00	10.0000	0.67000	0.24400	-0.17380
6.00	0.0000	0.65000	0.00000	-0.00000
50.00	180.1364	-1.49000	-0.00350	-0.01370
50.00	175.1365	-1.48400	0.01150	0.01290
50.00	170.1365	-1.46110	0.03050	0.01140
50.00	165.1365	-1.41380	0.05260	0.00830
50.00	160.1365	-1.34520	0.07480	0.00330
50.00	155.1365	-1.26720	0.09600	-0.00160
50.00	150.1365	-1.17630	0.12020	-0.01030
50.00	145.1365	-1.08280	0.14240	-0.01940
50.00	140.1365	-0.97940	0.16870	-0.03380
50.00	135.1365	-0.86340	0.18190	-0.04100
50.00	130.1365	-0.73350	0.19830	-0.05470
50.00	120.1365	-0.47060	0.27090	-0.11780
50.00	110.1365	-0.18790	0.36860	-0.20990
50.00	100.0000	0.06000	0.45900	-0.30340
50.00	90.0000	0.26300	0.54300	-0.38270

Table 3-9. Aerodynamic Stability Coefficients Stored in Memory (Cont)

M_n	α_T	C_A	C_{NY}	C_M
50.00	80.0000	0.38300	0.59700	-0.42840
50.00	70.0000	0.46900	0.63800	-0.46020
50.00	60.0000	0.54400	0.65200	-0.46860
50.00	50.0000	0.59100	0.65000	-0.46310
50.00	40.0000	0.62400	0.63800	-0.45290
50.00	30.0000	0.62200	0.57600	-0.40930
50.00	20.0000	0.64300	0.46300	-0.33150
50.00	10.0000	0.67000	0.24400	-0.17380
50.00	0.0000	0.65000	0.00000	-0.00000

3.1.19 Predictor

A digital predictor is required prior to the transmission of the aerodynamic moments to the analog computers where they are summed with the moments due to RCS and SPS moments and integrated to produce body rates. The predictor compensates for the lag in digital computation and D/A conversion. The predictor is a four-point (four derivative), Taylor function prediction.

$$X_P = \Delta t \left\{ \frac{161}{24} X_n - \frac{293}{24} X_{n-1} + \frac{211}{24} X_{n-2} - \frac{55}{24} X_{n-3} \right\}$$

where

Δt = iteration interval

X_{n-i} = previous values of the variable

3.1.20 Aerodynamic Impulse—Inertial Frame

The computed aerodynamic body forces are transformed to the inertial frame. The impulse increments are computed by trapezoidal integration since the frequency components do not exceed one cps.

$$\left| \Delta I^A \right|_I = [\cos(B,I)]^T \left| F^A \right|_B \Delta t$$

3.1.21 Aerodynamic ΔV—Inertial Frame

Impulse due to aerodynamic loads, $\left| \Delta I^A \right|_B$, is divided by the spacecraft mass to produce the velocity change.

$$\left| \Delta V^A \right|_I = \frac{1}{M_{CM}} \left| \Delta I^A \right|_I$$

3.1.22 Inertial-to-Geocentric Transformation Matrix

See Figure 3-3.

$$[\cos(G,I)] = [\theta][\psi]$$

$$[\cos(G,I)] = \begin{bmatrix} C\theta C\psi & C\theta S\phi & S\theta \\ -S\psi & C\psi & 0 \\ -S\theta C\psi & -S\theta S\psi & C\theta \end{bmatrix}$$

$$\theta = \theta^{E}_{G} \qquad \psi = \psi^{E}_{G} + \psi^{I}_{E}$$

where

$$\psi^{I}_{E} = \frac{360}{365}(D-80) + \omega_E t$$

D = number of days from 00.00 GMT (1 July 1968)

t = time from launch

3.1.23 Geocentric-to-Body Transformation Matrix

See Figure 3-3.

$$[\cos(B,LG)] = \left[\phi^{LG}_{B}\right]\left[\theta^{LG}_{B}\right]\left[\psi^{LG}_{B}\right]^{*}$$

$$[\cos(B,LG)] = \begin{bmatrix} C\psi C\theta & S\psi C\theta & -S\theta \\ -S\psi C\phi + C\psi S\theta S\phi & C\psi C\phi + S\phi S\theta S\phi & C\theta S\phi \\ S\psi S\phi + C\psi S\theta S\phi & S\psi S\theta C\phi - C\psi S\phi & C\theta C\phi \end{bmatrix}$$

$$[\cos(LG,G)] = \left[\psi^{G}_{LG} = 90°\right]\left[\theta^{G}_{LG} = -90°\right]^{**}$$

*A Z, Y, X rotation sequence

**A constant matrix

$$[\cos(LG, G)] = \begin{bmatrix} 0 & 1 & 0 \\ 0 & 0 & -1 \\ -1 & 0 & 0 \end{bmatrix}$$

3.1.24 Change in Velocity Due to SPS in VD-Frame

The V-frame is defined in terms of the G-frame and heading angle. The V-frame is described as the target velocity frame.

$$[\cos(V, G)] = \begin{bmatrix} {}^{LG}_{\psi_H} \end{bmatrix} \begin{bmatrix} {}^{G}_{\theta_{LG}} \end{bmatrix}$$

$$[\cos(V, G)] = \begin{bmatrix} 0 & \sin\psi & \cos\psi \\ 0 & \cos\psi & -\sin\psi \\ -1 & 0 & 0 \end{bmatrix}$$

where

$$\psi = \psi^{LG}_{H}$$

$${}^{G}\theta_{LG} = -90°$$

Another frame is defined by rotations from the V-frame. This process defines the VD-frame. The X-axis of this frame is oriented in the direction of the desired velocity increase.

$$[\cos(VD, V)] = \begin{bmatrix} {}^{G}\phi_{B} \end{bmatrix} \begin{bmatrix} {}^{V}\theta_{VD} \end{bmatrix} \begin{bmatrix} {}^{V}\psi_{VD} \end{bmatrix}^{*}$$

$$[\cos(VD, V)] = \left[\begin{array}{c|c|c} C\theta C\psi & C\theta S\psi & -S\theta \\ \hline -C\phi S\psi & C\phi C\psi & S\phi C\theta \\ +S\phi S\theta C\psi & +S\phi S\theta S\psi & \\ \hline S\phi S & -S\phi C\psi & C\phi C\theta \\ +C\phi S\theta C\psi & +C\phi S\theta S\psi & \end{array}\right]$$

*A Z, Y, X sequence.

where all subscripts and superscripts have been removed.

A platform to VD transformation can now be defined as follows:

$$[\cos(VD, P)] = [\cos(VD,V)][\cos(V, G)][\cos(G, P)]$$

Then,

$$\left|V^C\right|_{VD} = [\cos(VD, P)]\left|V^C\right|_P$$

where V^C is the total velocity change during a ΔV maneuver.

The transformation $[\cos(VD, P)]$ is computed at the beginning of RCS ullage and held constant until t_{ON} (time of thrust-on command), at which time it is redefined and again held constant throughout the SPS burn.

3.1.25 Pointing Error Computation

The total ΔV maneuver pointing error is

$$\epsilon_{\theta}^{P} = \tan^{-1}(-\dot{Z}^C/\dot{X}^C)_{VD}$$

$$\epsilon_{\psi}^{P} = \tan^{-1}(\dot{Y}^C/\dot{X}^C)_{VD}$$

The SPS maneuver efficiency is

$$\eta_{MAN} = \frac{\dot{X}^C_{VD}(\text{FINAL}) - \dot{X}^C_{VD}(\text{THRUST ON})}{\left(\frac{I_{SP}\,(M_I - M_F)\,g}{(M_F + M_I)/Z}\right)}$$

3.1.26 GDC Simulator

The GDC simulator is a digital substitute for the transformations normally computed in the GDC front end. These functions were bypassed in the hardware GDC because of noise problems.

3.1.26.1 GDC Initialization at Interrupt

GDC initialization occurs when the GDC alignment button is depressed. The values of the FDAI gimbal angles which occur at this instant are retained for use in generating the continuously varying FDAI gimbal angles. The elements of the matrix [cos(B, I)] produced in the IMU model are also stored—i.e., $[\cos(B,DI)^0]$ is computed from FDAI angles at time of interrupt and is stored as is $[\cos(B, I)^0]$ from the IMU.

$$[\cos(B, DI)^0] = \begin{bmatrix} C\psi C\theta & S\psi & -C\psi S\theta \\ -C\phi C\psi C\theta + S\theta S\phi & C\phi C\psi & C\phi S\psi S\theta + S\phi C\theta \\ S\phi S\psi C\theta + C\phi C\theta & -S\phi C\psi & -S\phi S\psi S\theta + C\phi C\theta \end{bmatrix}^*$$

where ϕ, θ, and ψ are $\phi_B^{DI}(0)$, $\theta_B^{DI}(0)$, and $\psi_B^{DI}(0)$, which are values of FDAI gimbal angles when interrupt occurs.

3.1.26.2 GDC Euler Angle Generation

The GDC model (Figure 3-5) continuously calculates the required ball Euler angles. These angles are solved by equating elements between equivalent matrices—i.e., [cos(B, DI)] may be represented in two ways.

$$[\cos(B, DI)] = [\cos(B, I)][\cos(B, I)^0]^T [\cos(B, DI)^0]$$

from IMU	from IMU at time of initialization	angles from FDAI drive source (GDC output)

also

$$[\cos(B, DI)] = [\phi_B][\psi_R][\theta_R]$$

where ϕ_R, θ_R, and ψ_R are the correct FDAI Euler angles.

*A Y, Z, X Euler sequence

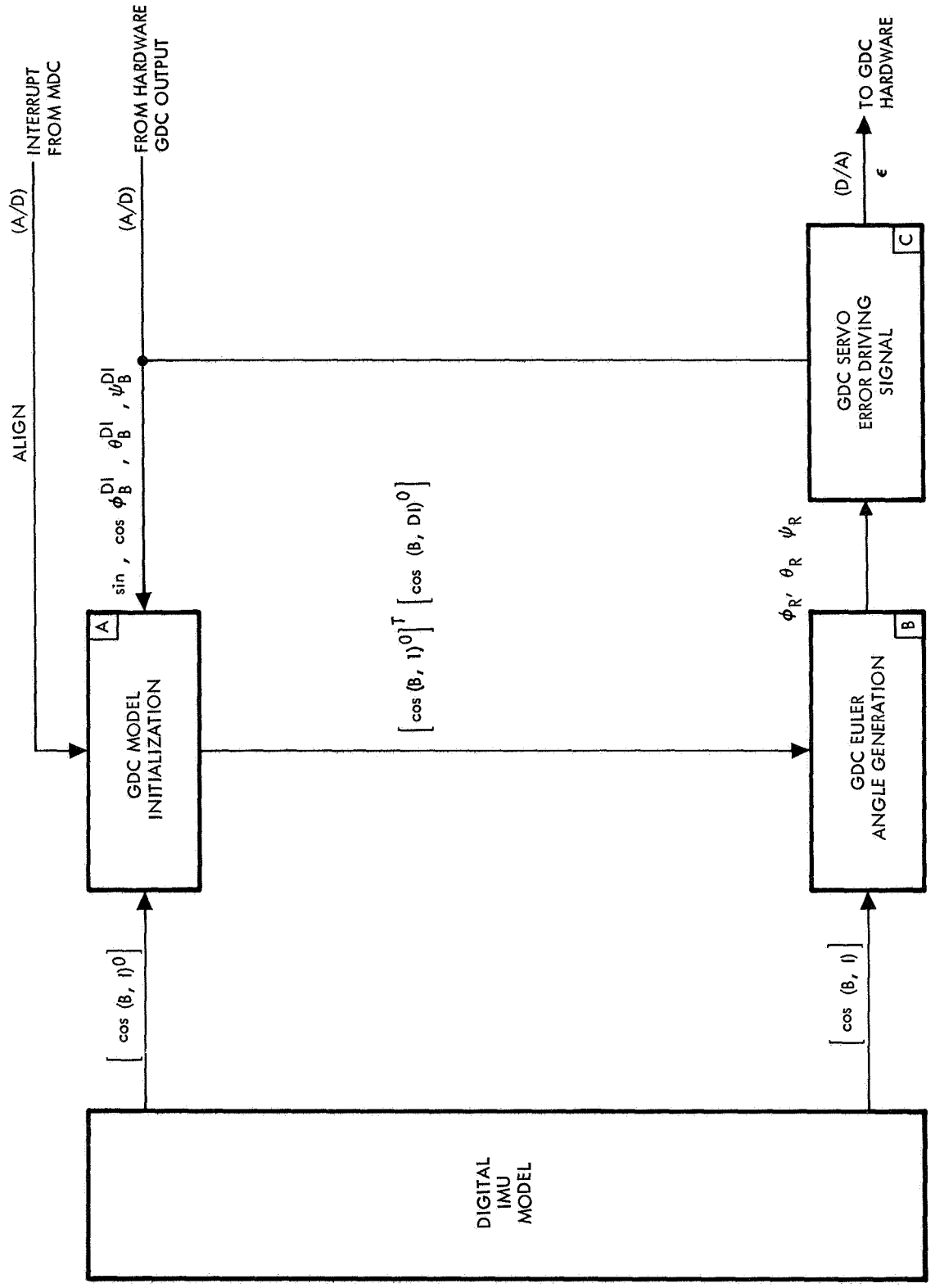

Figure 3-5. Gyro Display Coupler Simulator

By equating matrix elements, the sines and cosines of the required ball angles are obtained.

$$\sin \psi_R = \cos(B, SI)_{12} = a_{12}$$

$$\cos \psi_R = [1 - a_{12}^2]^{1/2}$$

$$\sin \phi_R = - a_{32}/\cos\psi_R$$

$$\cos \phi_R = a_{22}/\cos\psi_R$$

$$\sin \theta_R = - a_{13}/\cos\psi_R$$

$$\cos \theta_R = a_{11}/\cos\psi_R$$

where a_{ij} are elements of $[\cos(B, DI)]$

3.1.26.3 Error Signal to FDAI Ball Drive Motor

$$\epsilon_\phi = \sin(\phi_R - \phi_B^{DI}) = \sin\phi_R \cos\phi_B^{DI} - \cos\phi_R \sin\phi_B^{DI}$$

$$\epsilon_\theta = \sin(\theta_R - \theta_B^{DI}) = \sin\theta_R \cos\theta_B^{DI} - \cos\theta_R \sin\theta_B^{DI}$$

$$\epsilon_\psi = \sin(\psi_R - \psi_B^{DI}) = \sin\psi_R \cos\psi_B^{DI} - \cos\psi_R \sin\psi_B^{DI}$$

where

ϕ_B^{DI}, θ_B^{DI}, ψ_B^{DI} = actual FDAI drive angles from GDC

ϕ_R, θ_R, ψ_R = required FDAI drive angles from GDC

3.1.27 EMS Stability Roll Angle Simulator

The EMS digital model (Figure 3-6) derives a stability roll error signal which drives the roll resolver in the prototype GDC for control of the FDAI roll indicator and the EMS roll stability indicator.

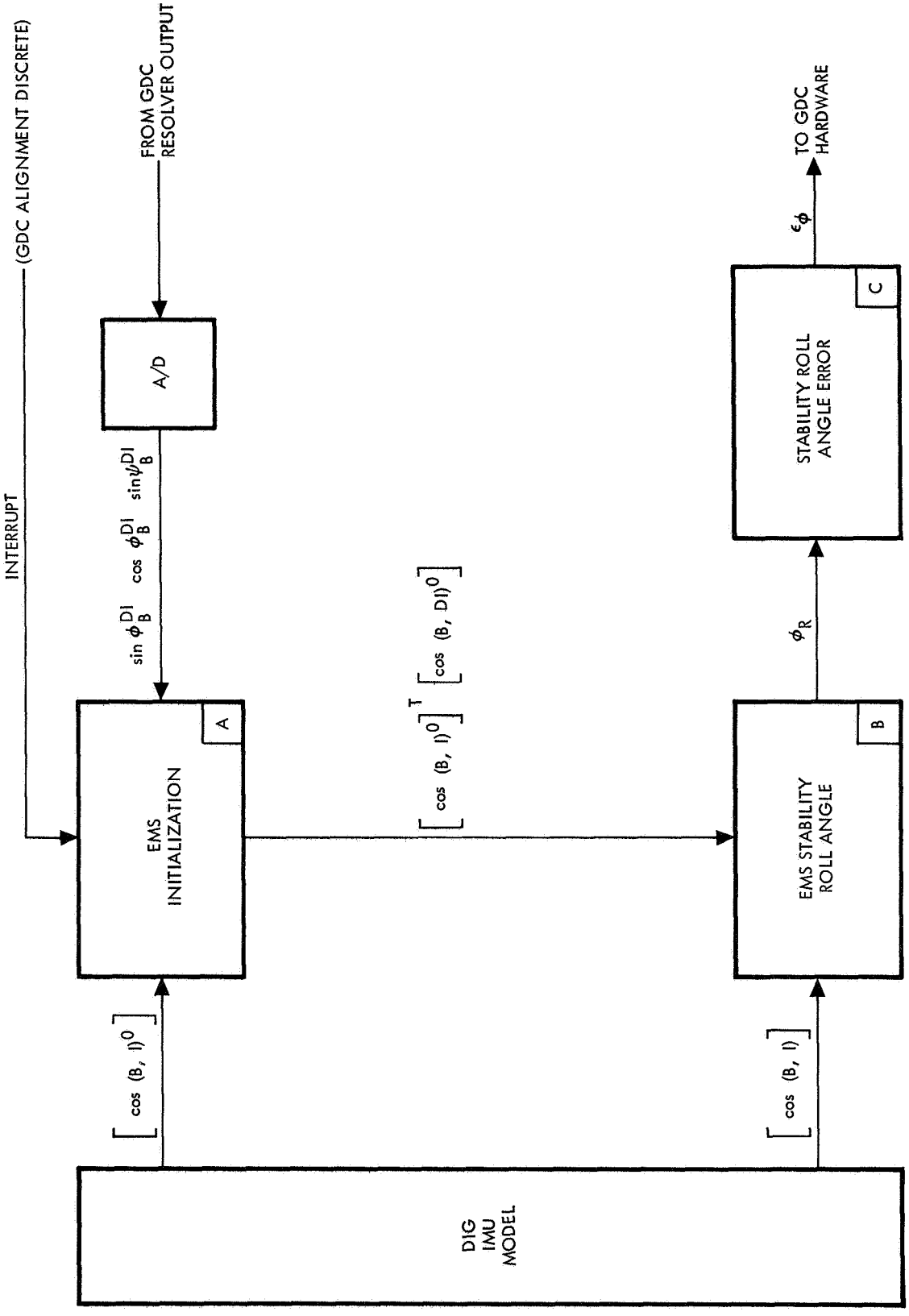

Figure 3-6. EMS Stability Roll Angle Simulator

3.1.27.1 EMS Initialization

EMS model initialization occurs when the GDC alignment button is depressed. At this instant, three elements of the matrix [cos(B, I)] available from the IMU model are stored—i.e., $\cos(B,I)^0_{21}$, $\cos(B,I)^0_{22}$, and $\cos(B,I)^0_{23}$, in addition to the roll and yaw signals to the FDAI gimbals—i.e., $\sin\psi_B^{DI}$, $\sin\phi_B^{DI}$, and $\cos\phi_B^{DI}$.

The desired stability roll rotation from an arbitrary FDAI reference orientation, DI-frame, can be found from the elements of [cos(NB, DI)]. The DI-frame is established by the choice of FDAI alignment angles at last alignment.

$$[\cos(OB, DI)] = [\cos(OB, B)]\,[\cos(B, I)]\,[\cos(B, I)^0]^T\,[\cos(B, DI)^0]$$

fixed — from IMU — from IMU at initialization — from FDAI at initialization

$$= [\phi_R][\psi_R][\theta_R]$$

where ϕ_R, ψ_R and θ_R are the required FDAI display angles (only ϕ_R is calculated).

3.1.27.2 EMS Stability Roll Angle

Since only one Euler angle is required from the matrix [cos(OB, DI)], i.e., ϕ_R, it is more efficient to solve for only those matrix elements necessary to produce ϕ_R. If a Y, Z, X (θ_R, ψ_R, ϕ_R) rotation sequence is assumed, a_{22} and a_{32} are then the required elements and ϕ_R is what ϕ_{NB}^{DI} should be

$$\sin\phi_R = \frac{a_{32}}{\left(a_{22}^2 + a_{32}^2\right)^{1/2}} = \frac{S\phi C\psi}{\left[C^2\phi C^2\psi + S^2\phi C^2\psi\right]^{1/2}}$$

$$\cos\phi_R = \frac{a_{22}}{\left(a_{22}^2 + a_{32}^2\right)^{1/2}} = \frac{C\phi C\psi}{\left[C^2\phi C^2\psi + S^2\phi C^2\psi\right]^{1/2}}$$

3.1.27.3 Stability Roll Angle Error

The stability roll angle error is calculated from the difference between GDC outputs $\sin\phi$, $\cos\phi$ and $\sin\phi_R$, $\cos\phi_R$.

$$\epsilon_\phi = \sin(\phi_R - \phi) = \sin\phi_R \cos\phi - \cos\phi_R \sin\phi$$

where ϕ is the angle sent out by the GDC to the displays.

3.1.28 IMU Model

The digital IMU model includes the mathematical manipulations outlined schematically in Figure 3-7. The numbers in the blocks correspond to the numbered explanations on the pages immediately following the figure.

There is no parallel integration in the simulation. The angular accelerations about the spacecraft axes are integrated on the analog computer to give body rates. The body rates are then converted through quaternion transformation and integration to quaternion elements from which a set of nine direction cosines is calculated forming a transformation (the BI-to-B transformation) from the initial body attitude at problem initiation to any subsequent angularly displaced attitude. The BI-frame from which the spacecraft is referenced then has a fixed relationship to the inertial I-frame. Thus, the I-to-BI transformation must be calculated for problem initiation, and the initialization of the quaternion elements becomes trivial.

All reference frames, including the platform frame, are then calculated by linear transformations from the BI- to B-frame.

Refer to Figure 3-7. There are two methods for arriving at the inertial-to-platform transformation, [cos(P, I)], depending upon which IMU mode is selected.

1. In the caged or coarse alignment modes, the platform gimbal angles are iteratively perturbed. During these modes, the [cos(P, I)] matrix is not updated. Only when these modes are left for one of the other three is the [cos(P, I)] updated by using the latest values of the gimbal angles (and the [cos(B, I)]) matrix, which is always updated every computation cycle.

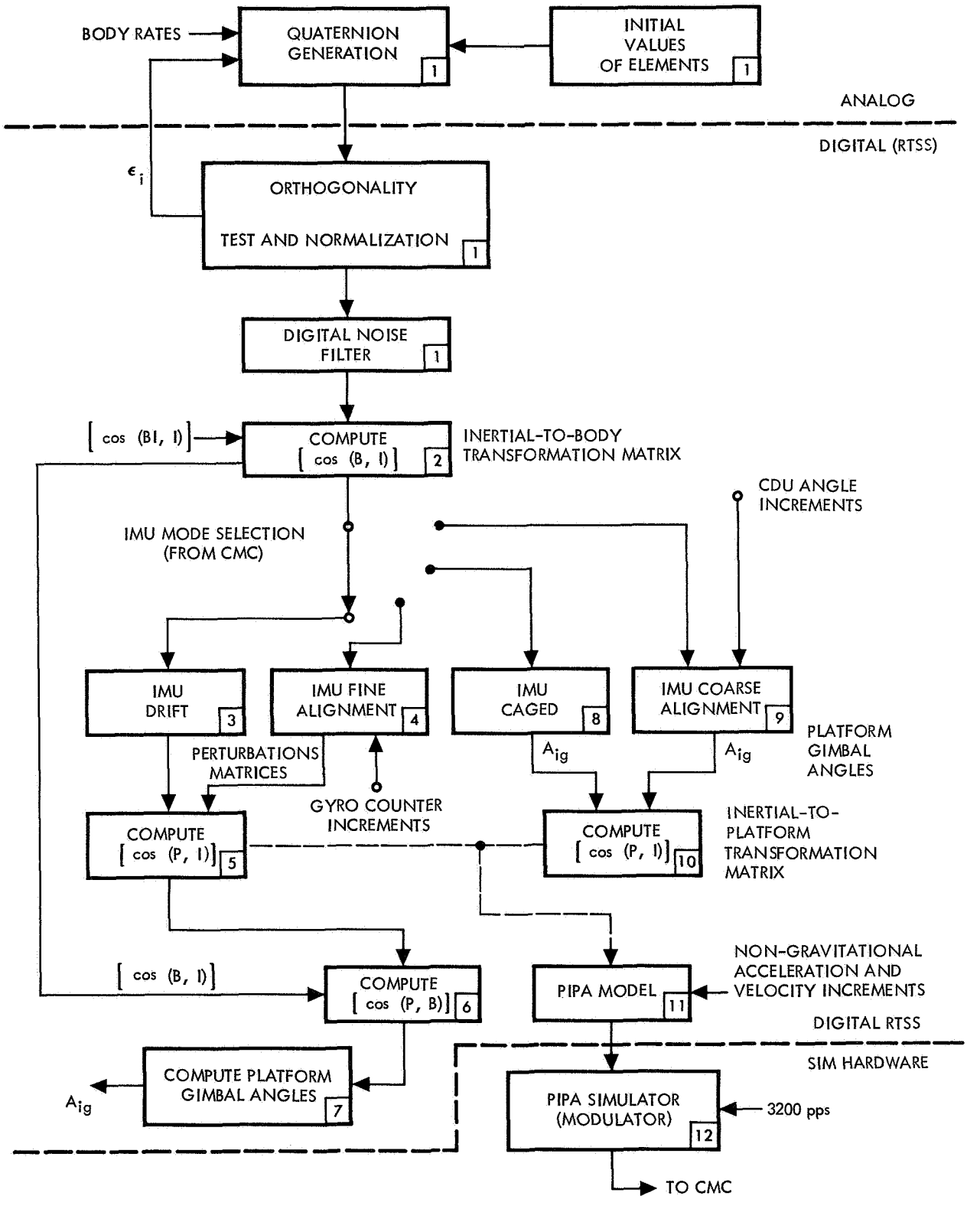

Figure 3-7. Flow Diagram of Calculations in IMU Model

2. In the drift and fine alignment modes, a small angle perturbation matrix is generated which premultiplies the previous [cos(P,I)] matrix, producing the new [cos(P,I)] matrix. This updating requires 10 computation frames for drift and 50 frames for fine alignment. The drift perturbation matrix is invariant, whereas the fine align perturbation matrix is computed from the platform gyro counter increment per computation cycle.

The platform gimbal angles are kept up to date in these modes by postmultiplying the [cos(P,I)] matrix by $[\cos(B,I)]^T$, which is always up to date, producing [cos(P,B)] . The gimbal angles are then derived from the direction cosine elements of this matrix.

The simulation of the PIPA results in a quite realistic sequence of pulses into the CMC. The output of a PIPA experiencing zero acceleration is characteristically a sequence of three positive pulses, followed by three negative pulses, and so on at a pulse rate of 3200 pps. If, for instance, a slight positive acceleration is sensed, an extra positive pulse will occur from time to time. With increasing sensed acceleration, the number of extra positive pulses will increase until all pulses are positive and the PIPA saturates. This saturation occurs at about +20 g's. Similarly, all output pulses would be negative at -20 g's. The CMC counts the positive and negative pulses and, from the difference, deduces the change in velocity.

The RTSS computes the number of extra positive or negative pulses to be produced per computer cycle interval (which is 20 milliseconds). This number is sent via the D/D interface to a modulator which operates on a 3200-pps carrier to produce the 3-3 pulse sequence plus the extra pulse or pulses computed by the RTSS.

Normally, the extra PIPA pulses would appear randomly distributed throughout any 20-millisecond time interval. However, the simulator modulator inserts all the extra pulses at or near the start of each period, which under high g conditions leads to some abnormal oscillation in the CMC acceleration and ΔV calculations. However, the simulation is highly realistic at low-g levels.

3.1.28.1 Generation and Correction of Quaternion Elements

In order to avoid transmission of high-frequency signals across the analog/digital interface, quaternion elements are sent to the RTSS in place of body rates. The quaternion elements are closely related to the integrals of body rates. Body Euler angles are a third choice, but are unsatisfactory because of singularities in the Euler rate equations.

Noise introduced by the A/D conversion is filtered out of the quaternion before [cos(B, BI)] is calculated. The quaternion generation interface is illustrated in Figure 3-8.

3.1.28.2 Inertial-to-Body Transformation Matrix

$$[\cos (B, I)] = [\cos (B, BI)][\cos (BI, I)]$$

where $[\cos (BI, I)] = [\cos (B, I)^0]$, i.e., computed at problem initiation and constant thereafter.

$$[\cos (B, BI)] = \frac{1}{N}\begin{bmatrix} \left(e_1^2 - e_2^2 - e_3^2 + e_4^2\right) & 2\left(e_1e_2 + e_3e_4\right) & 2\left(e_2e_4 - e_1e_3\right) \\ 2\left(e_3e_4 - e_1e_2\right) & \left(e_1^2 - e_2^2 + e_3^2 - e_4^2\right) & 2\left(e_2e_3 + e_1e_4\right) \\ 2\left(e_1e_3 + e_2e_4\right) & 2\left(e_2e_3 - e_1e_4\right) & \left(e_1^2 + e_2^2 - e_3^2 - e_4^2\right) \end{bmatrix}$$

where

N = normalizing factor

e_i = quaternion elements

i = 1-4

3.1.28.3 IMU Drift Perturbation Matrix

The drift matrix [cos (PD, P)] is constant and is calculated from a set of representative drift rates about the three spacecraft axes. When ω_{Xd}, ω_{Yd}, and ω_{Zd} are given, the total angular drift rate is

$$\dot{\mu}_d = \left[\omega_{Xd}^2 + \omega_{Yd}^2 + \omega_{Zd}^2\right]^{1/2}$$

The direction cosines of this rate vector with the spacecraft axes are

$$\cos \alpha_d = \omega_{Xd}/\dot{\mu}_d$$

$$\cos \beta_d = \omega_{Yd}/\dot{\mu}_d$$

$$\cos \gamma_d = \omega_{Zd}/\dot{\mu}_d$$

The incremental change in μ_d per computation cycle (10 frames) is

$$\Delta\mu_d = \dot{\mu}_d \Delta T$$

If

$$\Delta\mu_{d/2} = \phi$$

Then

$$[\cos(PD, P)] = \begin{bmatrix} (1-2S^2\phi S^2\alpha_d) & 2(S^2\phi C\alpha_d C\beta_d + S\phi C\phi C\gamma) & 2(S^2\phi C\alpha_d C\gamma_d - S\phi C\phi C\beta_d) \\ 2(S\phi C\alpha_d C\beta_d - S\phi C\phi C\alpha_d) & (1-2S^2\phi S^2\beta_d) & 2(S^2\phi C\beta_d C\gamma_d + S\phi C\phi C\alpha_d) \\ 2(S^2\phi C\alpha_d C\gamma_d + S\phi C\phi C\beta_d) & 2(S^2\phi C\beta_d C\gamma_d - S\phi C\phi C\alpha_d) & (1-2S^2\phi S^2\gamma_d) \end{bmatrix}$$

3.1.28.4 IMU Fine Alignment Mode Perturbation Matrix

The perturbation matrix is computed from the changes in the platform gyro displacement counters.

$$[\cos(PD, P)] = \begin{bmatrix} 1 - \frac{1}{2}\left(\Delta P_Z^2 + \Delta P_Y^2\right) & \Delta P_Z & -\Delta P_Y \\ -\Delta P_Z & 1 - \frac{1}{2}\left(\Delta P_X^2 + \Delta P_Z^2\right) & \Delta P_X \\ \Delta P_Y & -\Delta P_X & 1 - \frac{1}{2}\left(\Delta P_X^2 + \Delta P_Y^2\right) \end{bmatrix}$$

where ΔP_i is the change in the i^{th} gyro output during every fine alignment computation cycle.

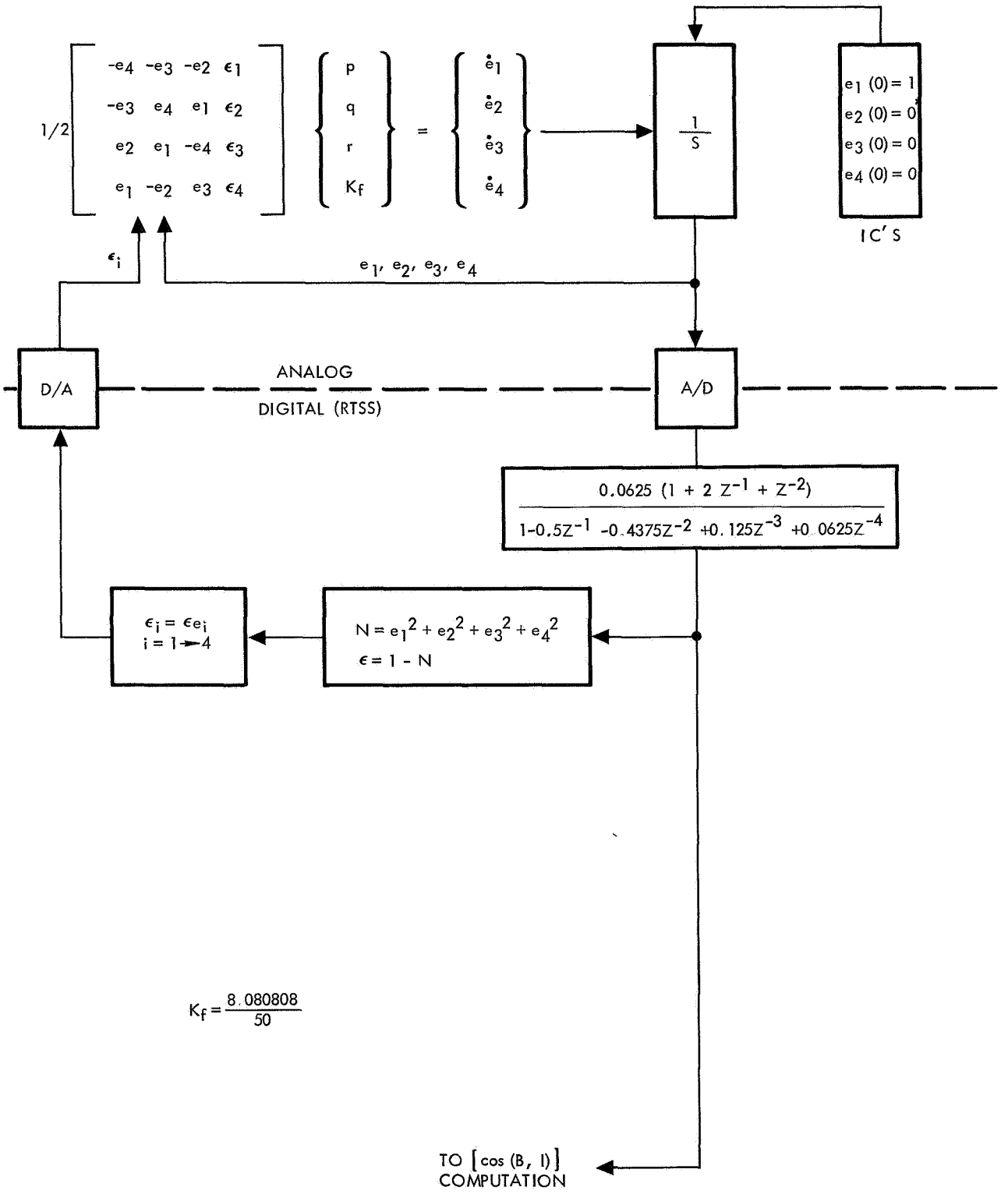

Figure 3-8. Quaternion Generation Interface

3.1.28.5 Inertial-to-Platform Transformation Matrix (Drift or Fine Alignment Modes)

In the drift or fine alignment modes, the updated [cos (P, I)] matrix is obtained by premultiplying the previous [cos (P, I)] matrix by the perturbation matrix from the drift or fine alignment mode, i.e.,

$$[\cos (PD, P)] \underset{(n)}{[\cos (P, I)]} = \underset{(n+1)}{[\cos (P, I)]}$$

3.1.28.6 Body-to-Platform Transformation Matrix

In the drift or fine alignment mode, it is necessary to compute the body-to-platform transformation to solve for the platform gimbal angles.

$$[\cos (P, B)] = [\cos (P, I)] [\cos (B, I)]^T$$

3.1.28.7 Platform Gimbal Angles

The gimbal angles are derived from the direction cosine elements of [cos (P, B)].

$$A_{mg} = \sin^{-1} [a_{21}]$$

$$A_{ig} = \tan^{-1} [-a_{31}/a_{11}]$$

$$A_{og} = \tan^{-1} [-a_{23}/a_{22}]$$

where a_{ij} is direction cosine in i^{th} row, j^{th} column.

3.1.28.8 Caged Mode

In the caged mode, the platform gimbal angles are computed directly.

$$A_{ig} = A_{ig} \text{ (last)} - K_C A_{ig} \qquad \text{(computed each cycle)}$$

where i represents i, m, o.

$$K_C = 0.01523$$

3.1.28.9 Coarse Alignment Mode

The platform gimbal angles are computed directly.

$$A_{ig} = A_{ig}\ (\text{last}) + K_E\, E_{ig}\ (\text{computed each cycle})$$

where

E_{ig} = gimbal drive command from the CDU. It is limited to a maximum value of 0.01745329252 rad.

K_E = 0.01 (based on 20-millisecond computation cycle)

3.1.28.10 Inertial-to-Platform Transformation Matrix (Caged and Coarse Alignment Modes)

In the caged or coarse alignment modes, the matrix [cos (P, I)] is updated only when switching to another mode. It is calculated as follows.

$$[\cos (P, I)] = [\cos (B, P)]^T [\cos (B, I)]$$

where

$$[\cos (P, B)] = [A_I]^T [A_M]^T [A_O]^T$$

$$[\cos (B, P)] = \begin{bmatrix} C\theta C\psi & S\psi & -S\theta C\phi \\ S\theta S\phi - C\theta S\psi C\phi & C\psi C\phi & C\theta S\phi + S\theta S\psi C\phi \\ S\theta C\phi + C\theta S\psi S\phi & -C\psi S\phi & C\theta C\phi - S\theta S\psi S\phi \end{bmatrix}^*$$

where θ, ψ, and ϕ represent A_{ig}, A_{mg}, A_{og} platform gimbal rotations in that sequence

[cos (B, I)] is always up to date in every computation cycle.

3.1.28.11 PIPA Model (RTSS Portion)

The digital calculations are shown in flow-graph form in Figure 3-9.

*X, Y, Z rotation sequence

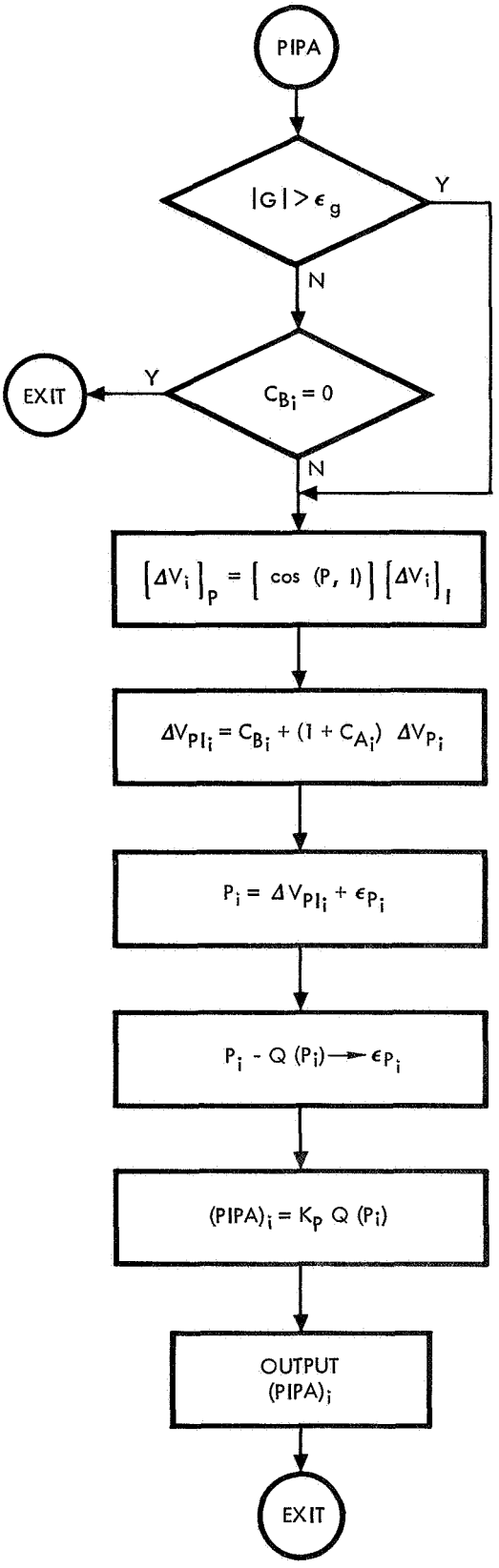

PIPA ROUTINE IS SELECTED.

TEST: IS PRESENT ACCELERATION LEVEL GREATER THAN THE NOISE LEVEL OF THE COMPUTATION COMBINED WITH NATURAL PIPA THRESHOLD ? $\epsilon_g = 0.035$ FT/SEC^2

TEST: IS THE PIPA BIAS ERROR ZERO? IF SO, DO NOT GO THROUGH PIPA CALCULATIONS FOR SUCH A LOW g-LEVEL

CONVERT THE CHANGE IN INERTIAL VELOCITY (DURING THIS CYCLE) TO A CHANGE ALONG PIPA AXIS

CALCULATE HOW MUCH SENSIBLE ΔV HAS ACCUMULATED ALONG PIPA AXIS.

CALCULATE HOW MUCH OF THIS ΔV WILL BE SENSED BY PIPA DURING THIS CYCLE.

CALCULATE RESIDUAL AMOUNT OF ΔV WHICH WILL BE SAVED AND ADDED ON NEXT CYCLE.

THIS DIGITAL WORD CONTAINS THE NUMBER OF UNBALANCED PIPA OUTPUT PULSES (TO BE GENERATED BY THE PIPA SIMULATOR).

THE OUTPUT GOES, VIA THE D/D INTERFACE, TO THE PIPA SIMULATOR WHERE IT IS USED TO MODULATE A 3200 PPS CARRIER

Figure 3-9. Digital Computation Sequence for Deriving a Simulated PIPA Output Corresponding to the Precalculated Spacecraft Velocity Change

3.1.28.12 PIPA Simulator (Modulator)

This part of the PIPA simulation is carried out in special purpose equipment interfacing between the RTSS (via D/D interface) and the CMC. A discussion of these operations is given in Subsection 3.3.

3.1.29 External Visual Display Computations

There are three simulated optical windows to the external world. (1) the left rendezvous window (LRW), (2) the scanning telescope (SCT), and (3) the sextant (SXT).

Through either the LRW or the SCT, but not both simultaneously, the earth sphere and/or the celestial sphere may be observed. These scenes are produced on a television display to the LRW where electronic matting is used to blank stars behind the earth. The same scene is displayed to the SCT; however, a direct view of the stars is combined with a television view of the earth, forbidding electronic matting out of stars behind the earth.

The sextant scene is a single point on a CRT representing a star and a single T representing a landmark. In practice, the sextant is used as a SCT of high magnification; therefore, only a single point is used. The capability for superimposing the landmark or another star still exists in the simulation, however.

Figure 3-10 represents the multiple transformations required to establish the relationship between the inertial LOS through the LRW and SCT and the celestial and earth spheres.

The celestial sphere optical probe is fixed, and the sphere rotates. The gimbal angles of the sphere then are required.

The earth sphere rotates about the polar axis and the orbit axis. The polar rate is fixed, but the orbit rate for noncircular orbits must be computed.

The optical probe viewing the earth sphere must be driven to any LOS direction relative to the earth that the spacecraft may have; therefore, three gimbal drive angles are computed for the probe.

The earth sphere optical probe focal plane distance to the sphere varies with LOS direction; therefore, a variable focus adjustment must be computed as the angle from local vertical to LOS varies. The transformations for determining this adjustment are also given in Figure 3-10.

The sextant display requires computation of the X-Y coordinates of a spot on a CRT. These coordinates are based on the inertial orientation of

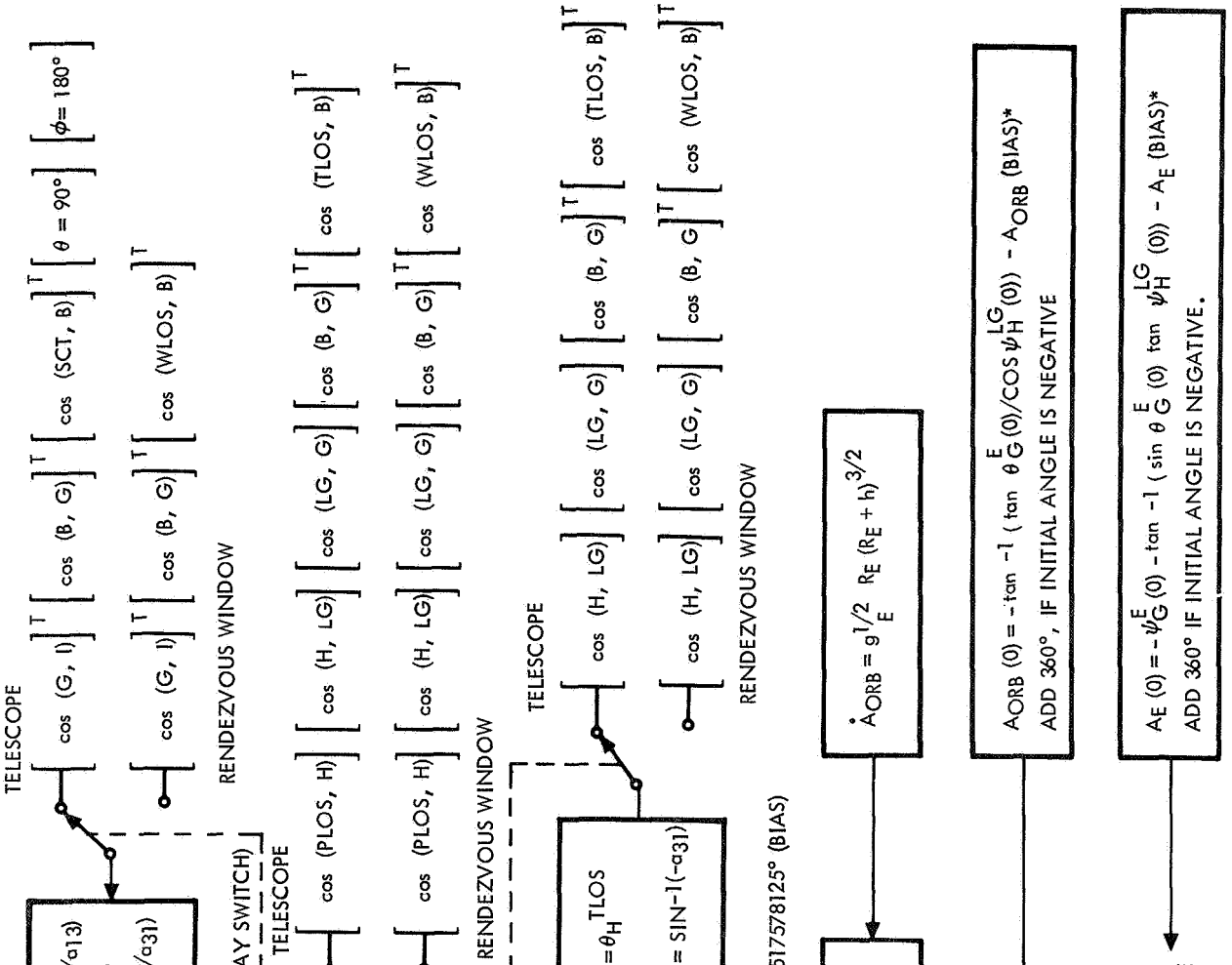

Figure 3-10. Flow Diagram of Transformation Matrix Operations Required for External Display Drives

the spacecraft and the spacecraft optics LOS relative to a selected star or landmark. These computations are given in Figure 3-11. Also available is the capability for determining the best choice of 37 prestored stars for any particular sextant orientation. The 37 stars are stored in memory with their inertial LOS components. See Table 4-2.

The actual digital computation scheme is more efficient than the flow diagrams would indicate. All transformations are not recomputed in every cycle. Presently, half the visual display computations are completed each computation cycle—i.e., a complete update occurs every 40 milliseconds.

The computed output angles are multiplexed from core memory to the digital-to-digital interface where they are compared with the digital shaft encoder returns from the display mechanisms. The D/D calculates an error signal that is then sent to the mechanism driving actuators.

The following transformations are required for visual display drives

$$[\cos(WLOS, B)] = \begin{bmatrix} C\theta C\psi & C\theta S\psi & -S\theta \\ S\theta C\psi S\phi - S\psi C\phi & S\theta S\psi S\phi + C\psi C\phi & C\theta S\phi \\ S\theta C\psi C\phi + S\psi S\phi & S\theta S\psi C\phi - C\psi S\phi & C\theta C\phi \end{bmatrix}^{*}$$

where**

$$\theta = \theta^{B}_{LOS}$$

$$\psi = \psi^{B}_{LOS}$$

$\phi = \phi^{B}_{LOS}$ (actually, the roll orientation of the television monitor with respect to the B-frame)

$$[\cos(SCT, B) = [\text{SHAFT DEROTATION}][\text{TRUNNION ROTATION}][\text{SHAFT ROTATION}][\cos(OB, B)]$$

$$= [\cos(SXT, B)]$$ (Use SXT angles in place of telescope angles)

*Z Y X rotation sequence

**All three angles are zero at present.

$$[\cos(SCT, B)] = \begin{bmatrix} CA_S & -SA_S & 0 \\ SA_S & CA_S & 0 \\ 0 & 0 & 1 \end{bmatrix} \begin{bmatrix} CA_T & 0 & -SA_T \\ 0 & 1 & 0 \\ SA_T & 0 & CA_T \end{bmatrix} \begin{bmatrix} CA_S & SA_S & 0 \\ -SA_S & CA_S & 0 \\ 0 & 0 & 1 \end{bmatrix} \begin{bmatrix} C\theta & 0 & -S\theta \\ 0 & 1 & 0 \\ S\theta & 0 & C\theta \end{bmatrix}$$

(devotion of shaft)

where $\theta = 32.5231132°$. The shaft is derotated after trunnion rotation to realign cross hairs in field of view.

$$[\cos(TLOS, B)] = [\text{ROTATION OF SCT TO VIEW EARTH}][\cos(SCT, B)]$$

$$= \begin{bmatrix} 0 & 0 & 1 \\ 0 & 1 & 0 \\ -1 & 0 & 0 \end{bmatrix} [\cos(SCT, B)]$$

$$[\cos(B, G)] = [\cos(B, LG)][\cos(LG, G)]$$

$$[\cos(B, G)] = \begin{bmatrix} C\psi C\theta & S\psi C\theta & -S\theta \\ -S\psi C\phi + C\psi S\theta S\phi & C\psi C\phi + S\psi S\theta S\phi & C\theta S\phi \\ S\psi S\phi + C\psi S\theta C\phi & S\psi S\theta C\phi - C\psi S\phi & C\theta C\phi \end{bmatrix} \begin{bmatrix} 0 & 1 & 0 \\ 0 & 0 & -1 \\ -1 & 0 & 0 \end{bmatrix}^*$$

where

$$\psi = \psi_B^{LG}$$

$$\theta = \theta_B^{LG}$$

$$\phi = \phi_B^{LG}$$

$$[\cos(G, I)] = \begin{bmatrix} C\theta C\psi & C\theta S\psi & S\theta \\ -S\psi & C\psi & 0 \\ -S\theta C\psi & -S\theta S\psi & C\theta \end{bmatrix}^{**}$$

*Z, Y, X rotation sequence.

**ψ, θ sequence.

STAR COORDINATES ON CRT

SXT TRUNNION DISPLAY X_{STAR}, Y_{STAR} $\leftarrow \begin{Bmatrix} X_{STAR} \\ Y_{STAR} \\ Z_{STAR} \end{Bmatrix}_{SXT} = (K_T) [\cos (SXT, B)] [\cos (B, G)] [\cos (G, I)] \left\{R^0_{STAR}\right\}_I$ **

LANDMARK COORDINATES ON CRT

SXT SHAFT DISPLAY X_{LM}, Y_{LM} $\leftarrow \begin{Bmatrix} X_{LM} \\ Y_{LM} \\ Z_{LM} \end{Bmatrix}_{OB} = (K_S) [\cos (OB, B)] [\cos (B, G)] [\cos (G, I)] \left\{R^0_{LANDMARK}\right\}_I$

ERROR PRINTOUT

*

$\epsilon_M = \tan^{-1}\left(\frac{X_{STAR}}{Z_{STAR}}\right) + \tan^{-1}\left(\frac{X_{LM}}{Z_{LM}}\right)$

*

$\epsilon = \cos^{-1}(Z_{STAR}/K_T)$

$\left\{R^T\right\}_I = [\cos (G, I)]^T [\cos (B, G)]^T [\cos (SXT, B)]^T \begin{Bmatrix} 0 \\ 0 \\ \hat{1} \end{Bmatrix}_{SXT}$

$\left\{R^0\right\}_I$ IS SELECTED FROM A TABLE OF MAJOR STARS STORED IN CMC MEMORY. SEE TABLE 4-2.

$\epsilon_T = \left\{\hat{R}^T\right\}^T_I \left\{R^0\right\}_I$
(SCALAR PRODUCT)

TEST AND SELECT NAVIGATION STAR, R^0 IN DETERMINED OCTANT, FOR MAXIMUM SCALAR PRODUCT ABOVE

*NOT CALCULATED FOR ME101
**INERTIAL COORDINATES OF PASSIVE VEHICLE ARE SUBSTITUTED FOR STAR IN RENDEZVOUS SIMULATION

Figure 3-11. Flow Diagram of Transformations Required for Sextant Simulation

where

$$\theta = \theta_G^E$$

$$\psi = \psi_G^E + \psi_E^I$$

and

$$\psi_E^I = \frac{360}{365}(D - 80) + \omega_E t$$

where

D = number of days from 1 July 1968, including fractional part

t = time from launch

$$[\cos(LG, G)] = \begin{bmatrix} 0 & 1 & 0 \\ 0 & 0 & -1 \\ -1 & 0 & 0 \end{bmatrix}$$

$$[\cos(H, LG)] = \begin{bmatrix} C\psi & +S\psi & 0 \\ -S\psi & C\psi & 0 \\ 0 & 0 & 1 \end{bmatrix}$$

where

$$\psi = \psi_H^{LG} = \sin^{-1}\left(\cos i / \cos \theta_G^E(0)\right)$$

and

$$i = \cos^{-1}\left(\cos \theta_G^E(0) \sin \psi_H^{LG}(0)\right)$$

$$[\cos(\text{PLOS}, H)] = \begin{bmatrix} C\theta & 0 & S\theta \\ 0 & 1 & 0 \\ -S\theta & 0 & C\theta \end{bmatrix}$$

where

$\theta = \theta^{H}_{PLOS}$ (the optical probe offset angle from the tangent to the orbit in the orbit plane)

3.1.30 Passive Rendezvous Vehicle Velocity and Position

A direct numerical integration method is used to compute the passive rendezvous vehicle velocity and position. The gravity model is identical to that used for the active vehicle, i.e., a complete four-term gravity model see paragraph 3.1.10. The integration routine is a two-point predictor-corrector

$$\text{PREDICTOR } Y_{n+1} = Y_n + \frac{\Delta t}{2}\left(3Y^1_n - Y^1_{n-1}\right)$$

$$\text{CORRECTOR } Y_{n+1} = Y_n + \frac{\Delta t}{2}\left(Y^1_{n+1} + Y^1_n\right)$$

where

Δt = iteration interval and

Y_n = X, Y, or Z value in the n^{th} computation interval

$Y'_n = \dot{X}$, $\dot{Y}$, or $\dot{Z}$ value in the n^{th} computation interval

If the iteration step size is ≤ 0.5 seconds, then the passive vehicle trajectory error will not exceed an RMS value of 50 feet over a period of 30 minutes. This algorithm provides updates of passive vehicle position to the visual displays at the rate of 10 per second. A Δt of 100 milliseconds is currently in use.

3.1.31 Methods for Initializing Hybrid Simulation

There are several sets of data which may be used to initialize the simulator. All information is read in on IBM cards to the RTSS, which then initializes the CMC, analog sections, and all other special purpose simulator

subsystems. If initial body rates with respect to inertial space are desired, then these initial conditions on p, q, and r must be made directly on the appropriate analog integrators. This option is never exercised in practice.

The initialization breaks into six categories

(A) Spacecraft center-of-gravity position

(B) Spacecraft center-of-gravity velocity

(C) Spacecraft body axis orientation

(D) Platform orientation

(E) Earth orientation with respect to sun and stars

(F) Passive rendezvous vehicle position and velocity

1. The simplest and most often used set of initial condition data is in inertial I-frame.

   (A) X, Y, Z components of $\vec{R}$ in I-frame

   (B) $\dot{X}$, $\dot{Y}$, $\dot{Z}$ components of $\vec{V}_I$ in I-frame

   (C) $\psi_B^I \theta_B^I \phi_B^I$, ZYX rotations from I-frame to B-frame

   (D) [REFSMMAT] all nine elements

   (E) Day and time of day of launch measured from 00.00 GMT, 1 July 1968 (in units of days)
   t, mission time elapsed

   (F) X, Y, Z components of $\vec{R}$ in I-frame
   $\dot{X}$, $\dot{Y}$, $\dot{Z}$ components of $\vec{V}_I$ in I-frame

2. Another convenient set of initial condition data is in the G-frame.

   (A and E) Day and time of day of launch measured from 00.00 GMT, 1 July 1968 (in units of days)

   t, mission time elapsed

$\theta_G^E \psi_G^E$, geocentric lattitude and longitude

h, altitude above ellipsoidal geocentric earth (calculated from earth center to spacecraft center of gravity and earth radius at given geocentric lattitude.)

(B) $\left|\vec{V}_I\right|$, magnitude of inertial SC velocity

ψ_H^{LG}, the heading angle

γ_I, the flight path angle

(C) ψ, θ, ϕ, the ZYX rotations from LG- to B-frame

(D) A_{ig}, the platform gimbal angles

(F) X, Y, Z components of $\vec{R}$ in I-frame
$\dot{X}$, $\dot{Y}$, $\dot{Z}$ components of $\vec{V}_I$ in I-frame

3. Initialization may also be performed in the CMC manner.

(A) X, Y, Z components of $\vec{R}$ in P-frame

(B) $\dot{X}$, $\dot{Y}$, $\dot{Z}$ components of $\vec{V}_I$ in P-frame

(C and D) [REFSMMAT] all nine elements

A_{ig}, the platform gimbal angles

(E) Day and time of day of launch measured from 00.00 GMT, 1 July 1968 (in units of days)

t, elapsed mission time

(F) X, Y, Z components of $\vec{R}$ in I-frame
$\dot{X}$, $\dot{Y}$, $\dot{Z}$ components of $\vec{V}_I$ in I-frame

3.2 DIGITAL-TO-DIGITAL INTERFACE

This interface is composed mostly of registers for storing binary quantities so that they are available for transfer either to the digital core memory or to the external hardware and displays. The interface also performs as a summing junction, producing an error signal to drive the external visual display mechanisms. The arithmetic logic compares the calculated

angles from the computer with the return signals from the digital shaft encoders. This digital error is then modified in the visual display interface by either digital-to-analog conversion or digital-to-400 cycles per second ac conversion as shown in Figure 3-12. The flow of words between registers is controlled by the sequence register so that the registers are updated as required by external hardware.

3.3 INTERFACE HARDWARE

The following special purpose simulation electronics are required for signal compatibility between the RTSS and the prototype hardware used in the simulator. Figure 3-13 shows the interface hardware between the CMC and the D/D.

3.3.1 Digital IMU Model-to-Hardware ICDU Interface

The ICDU normally converts the IMU platform gimbal angles into digital quantities for the CMC. In the simulator, the IMU gimbal angles are computed and available in digital form at the D/D interface.

In order to generate the proper inputs to the prototype ICDU's, the digital representations of the gimbal angles are sequentially sampled at the D/D and converted to analog signals representing sin A_{ig}, cos A_{ig} and sin 16 A_{ig}, cos 16 A_{ig}. These signals then modulate 800-cps carriers and are sent to the ICDU.

3.3.2 CMC-to-Digital Platform Torqueing Model Interface

The CMC normally generates a torqueing signal to the platform servos for realigning the IMU. Since the simulator mathematically realigns the IMU digital model, the torqueing signals must be counted and the count must be converted to a parallel digital word for acceptance by the D/D interface with the RTSS. This process is accomplished by sequentially sampling a counter register. The counter register and sequencer are reset on command from the RTSS.

3.3.3 Telemetry Interface Between CMC and RTSS

All telemetry communication with the CMC is via the RTSS. The CMC communicates serially, and the RTSS communicates by parallel words. Therefore, the interfacing hardware converts between serial and parallel wording. A special unit for initiating and timing of downlink data from the CMC is required. The CMC also takes care of uplink timing.

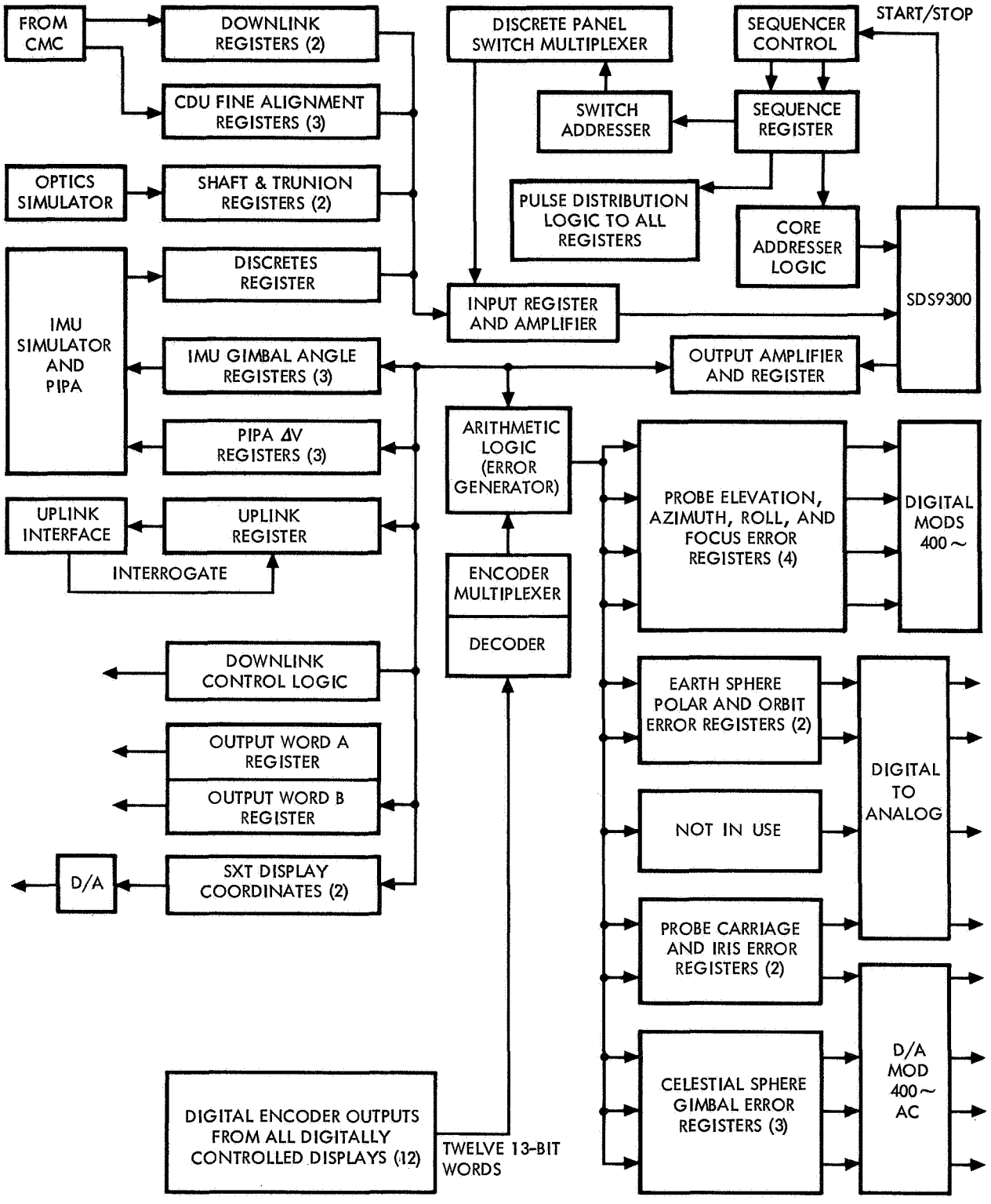

Figure 3-12. Flow Diagram of Digital-to-Digital Interface

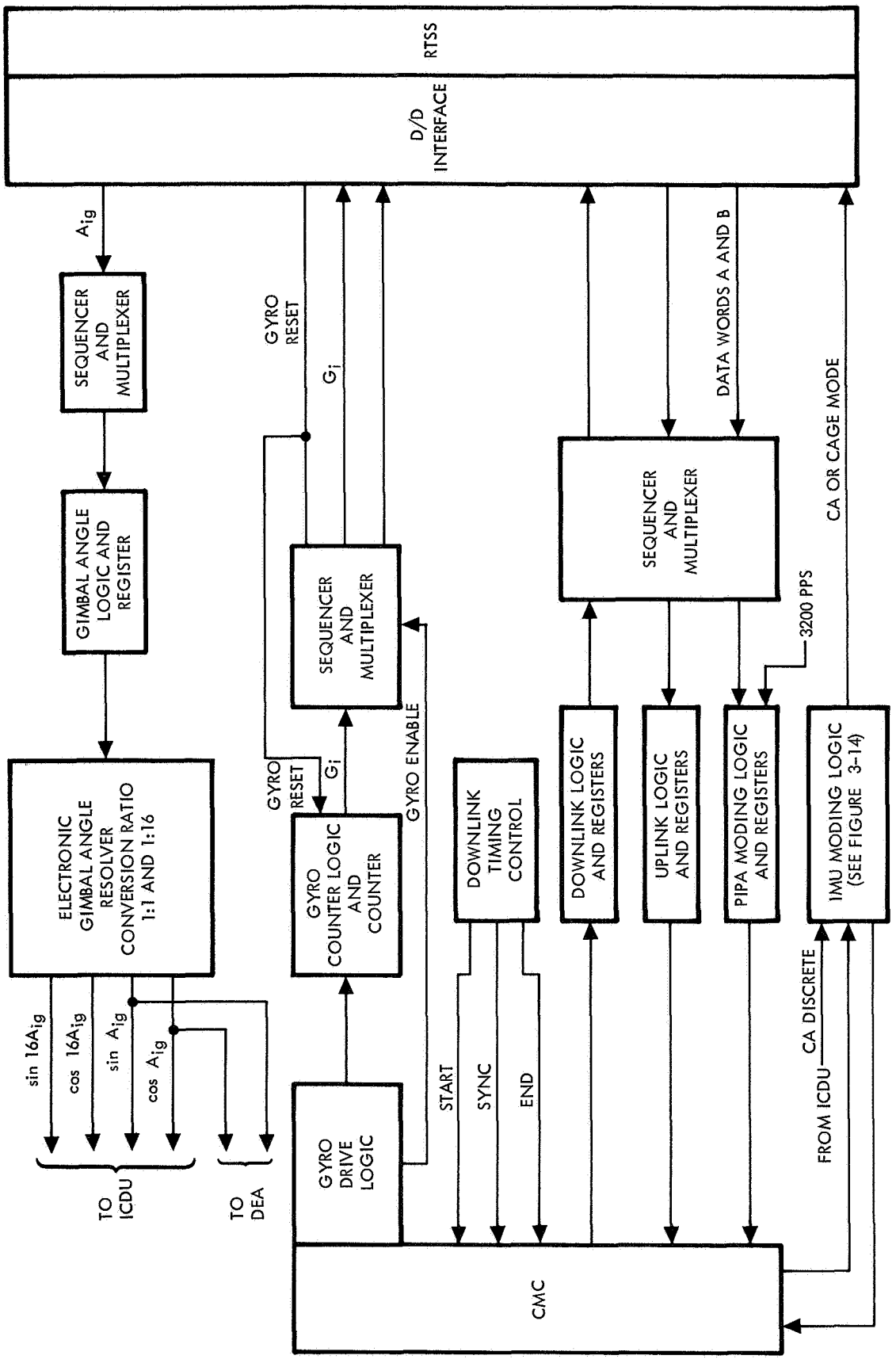

Figure 3-13. Interface Hardware Between CMC and Digital-Digital Converter

3.3.4 Digital PIPA Model-to-CMC Interface

Normally, the PIPA puts out a series of positive and negative pulses at a pulse rate of 3200 pps. An imbalance in the number of positive and negative pulses indicates a sensed non-zero acceleration level.

The digital PIPA model computes the amount of imbalance per computation cycle; the interface then must use this information to modulate a 3200 pps pulse train to reflect this computed imbalance.

3.3.5 Simulated IMU Moding Logic Function of PSA

The power servo assembly (PSA) normally performs the IMU mode switching logic. Special purpose circuitry simulates those logical functions associated with the PSA. This interface hardware provides the RTSS, via the D/D, with logical signals for program control in the digital IMU model routines. See Figure 3-14.

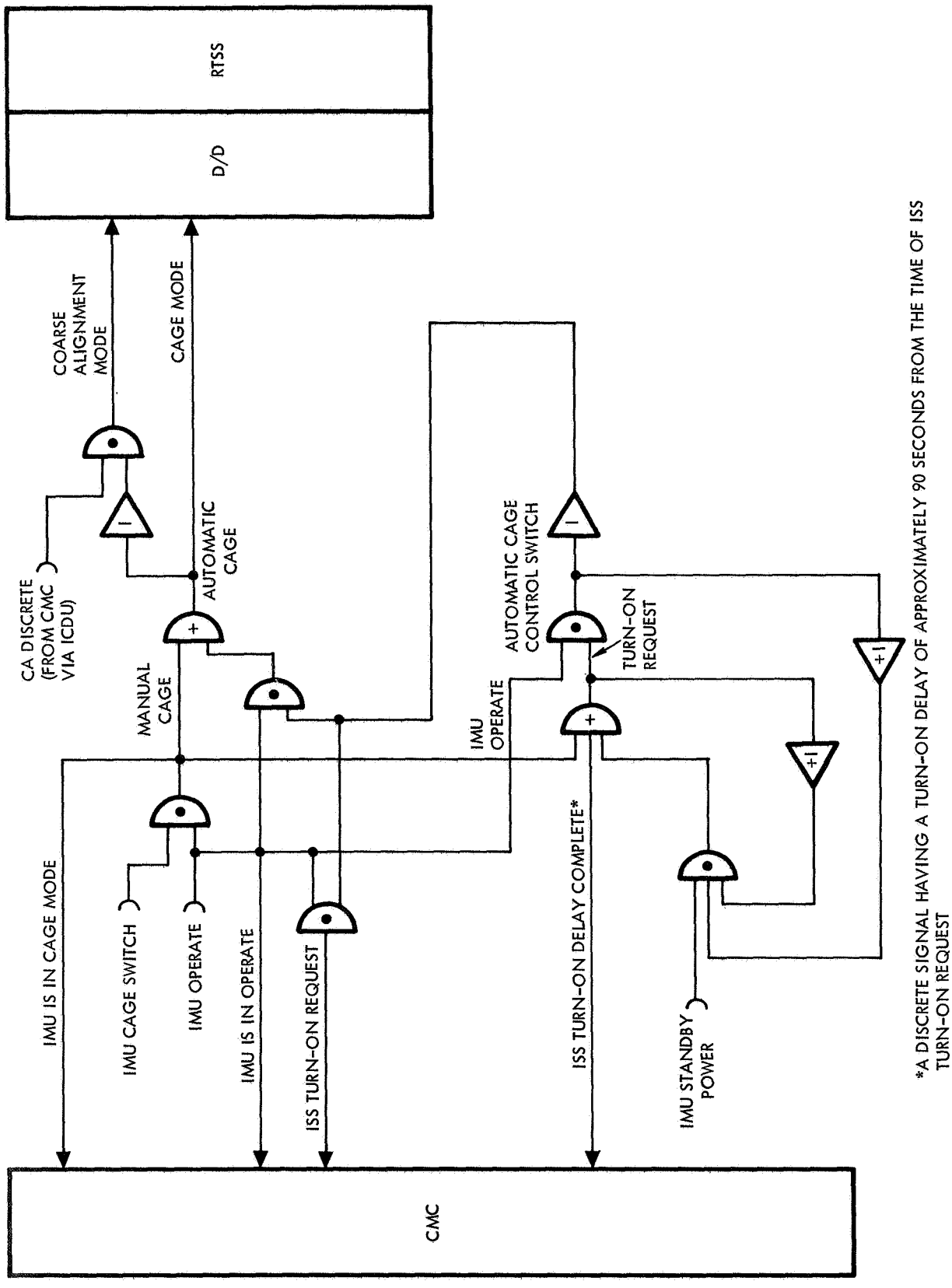

Figure 3-14. IMU Moding Logic

4.0 EXTERNAL VISUAL DISPLAY MECHANISMS

The external visual displays consist of a large sphere appropriately rendered to simulate the earth, a sphere with small steel balls embedded to simulate the celestial sphere, and a television viewing system to present scenes to the viewer on a cathode-ray tube (CRT). Appropriate optics are incorporated into the viewing system to form virtual imaging of scenes at infinity. Also included is a sextant character generator which is presented on an oscilloscope through collimating optics. Special scenes requiring views of both sphere models are provided by special electronic and optical processing. Window and scanning telescope viewing of the earth-celestial sphere models cannot be provided simultaneously.

4.1 EARTH MODEL AND VIEWING SUBSYSTEM

A photograph of the spherical earth model is shown in Figure 1-3. It is supported in such a manner as to permit rotations about an axis perpendicular to an orbit track and an axis coincident with the polar axis. Easterly progression caused by the earth's rotation is accomplished by a drive about the earth's polar axis.

The orbit inclination can be incrementally varied through 0- to 40-degree limits by changing the angle of the polar axis with respect to the orbit drive axis. The orbital rotation drive rate can be varied to represent the spacecraft velocity.

The earth sphere has 31 landmarks (Table 4-1) with terrain detail accuracy equivalent to one-half mile, positioned to within three nautical miles (nm) from their real earth location. The resolution detailing decreases gradually, approximately linearly, as the distance from each landmark increases until at 100 nm the detailing corresponds to one nm. The remaining terrain includes features (lakes, islands, rivers, etc.) that cover 100 square miles with the exception of remote, unfamiliar areas that are more than 1000 miles from landmarks. This latter terrain excludes features with areas less than 400 square miles, but has artistic conceptional detailing to correspond to one nm. Rivers are portrayed that are visually significant as viewed from an altitude of 100 nm.

Table 4-1. Earth Sphere Landmarks

Landmark	Position		
	Miles	Latitude (deg and min)	Longitude (deg and min)
(a) Pueo Point, Niihau, Hawaii	599	N21, 54	W160, 04.5
(b) Upolu Point, Hawaii, Hawaii	599	N20, 16.3	W155, 51
(c) Santa Rosa Island (west tip), California	404	N34, 00	W120, 15
(d) Punta del Norte, Isla de Guadalupe, Mexico	472	N29, 12	W118, 15.5
(e) Cabo de San Agustin, Isla Cedros, Mexico	472	N28, 06	W115, 22
(f) Punta Concepcion, Baja, California, Mexico	520	N26, 53	W111, 50
(g) Punta Tosca, Isla Santa Margarita	520	N24, 18.5	W111, 42
(h) Cabo San Antonio, Peninsula de Guanahacabiles, Cuba	587	N21, 52	W84, 57
(i) Key West (west end), Florida	525	N24, 33	W81, 48
(j) Cape Canaveral, Florida	466	N28, 27.6	W80, 31.6
(k) Bermuda Islands	412	N32, 19.5	W64, 44.5
(l) Dakar, Senegal	697	N14, 44.5	W17, 32

Table 4-1. Earth Sphere Landmarks (Cont)

Landmark	Miles	Position	
		Latitude (deg and min)	Longitude (deg and min)
(m) Cap Blanc, Mauritania	575	N20, 46.5	W17, 03
(n) Las Galletas, Tenerife, Canary Islands	536	N27, 59.5	W16, 41
(o) Kambia, Sherbo Island, Sierra Leone	818	N7, 34	W12, 58
(p) Barra de Corimba, Angola	1507	S9, 04	E12, 59.5
(q) Pelican Point, Walrus Bay, Southwest Africa	1273	S22, 53	E14, 27
(r) Luderitz Bay, Southwest Africa	1302	S26, 38	E15, 5
(s) Cabo de Inhaca, Ilha da Inhaca, Mozambique	1299	S25, 58	E32, 59
(t) Rugezi, Lake Victoria, Tanganyika	932	S2, 06.5	E33, 12
(u) Lake Nyasa (near Mbamba Bay), Tanganyika	1054	S11, 21	E34, 46
(v) Ilah do Bazaruto (north tip), Mozambique	1276	S21, 30.5	E35, 29
(w) Baia de Inhambane, Mozambique	1276	S23, 46.5	E35, 29.5
(x) Cape Peron, Peron Peninsula, Western Australia	1346	S25, 32	E113, 29

Table 4-1. Earth Sphere Landmarks (Cont)

Landmark	Miles	Position	
		Latitude (deg and min)	Longitude (deg and min)
(y) Northwest Cape, Exmouth Gulf, Western Australia	1229	S21, 47	E114, 09.5
(z) Cape Leeuwin, Western Australia	1461	S34, 22.5	E115, 07.5
(aa) Ponta Sevirava, Portugese Timor	1100	S8, 23	E127, 18
(ab) Cape Bedford, Queensland, Australia	1111	S15, 14	E145, 20.5
(ac) Cape St. George, New Ireland, Mismark Archipelago	989	S4, 51	E152, 53
(ad) Bougainville Island (Southeast tip), Solomon Islands	990	S6, 48.5	E155, 54.5
(ae) Cape Zelee, Maramasike Island, Solomon Islands	1094	S9, 48	E161, 33

Landscape rendering is painted in varying shades of four colors with the primary concern being land-water contrasts. Relief detailing is accomplished by shadow effects with the artistic work so illustrated as to minimize any ambiguity due to relative sun position.

The earth scene image for the window and scanning telescope is generated by a special optical probe designated the near object scanning probe (NOSP). It is a servo-driven lens system inserted between the earth model and a TV camera. The probe allows the viewing point to approach to within one-half inch of the six-foot-diameter earth model. The probe with its positionable gantry is shown in Figure 1-3. The front prism and the shaft within the NOSP are driven to simulate either the motion of the spacecraft or the combined motion of the spacecraft and shaft and trunnion angles of the

SCT to provide scene scanning. This is accomplished without shifting the view point of the probe. As the line-of-sight (LOS) distance to the model varies due to a changing viewing angle, focusing is adjusted automatically. The probe can be manually moved relative to the earth model to simulate discrete altitudes of from 35 to 28,000 nm.

The optical probe performance characteristics are shown in the following:

Position accuracy	7.5 minutes of arc
Focusing range	1/2 inch to infinity
Maximum rates	Approximately 40 deg/sec
Deadband	Less than 2.5 minutes of arc
Displacement	Yaw, roll - continuous pitch 0 to 135 deg

4.2 CELESTIAL SPHERE AND VIEWING SUBSYSTEM

The celestial sphere is viewed either directly through the SCT or with a flying spot scanner system for window scene presentation. A photograph of the celestial sphere is shown in Figure 1-3. It simulates a star field composed of 1353 stars varying from -1 to the fifth magnitude. Table 4-2 provides a list of 37 major stars stored in CMC memory and simulated accurately on the celestial sphere. The celestial sphere star placement is based on 1960 emphemeris data. For this reason, the star coordinates in the CMC program tapes were changed to those coordinate values that would coincide with exact calibrated star position on the celestial sphere. Therefore, the star coordinate appearing in the CMC and simulator are 1960 ephemeris plus or minus the static optical simulator errors. The stars are simulated by varying diameter polished steel balls positioned on a sphere to within 25 arc minutes of their true position in the heavens. The sphere is mounted in a gimbal system having three degrees of freedom in roll, pitch, and yaw. The sphere's support configuration consists of an inner, middle, and outer gimbal plus a fourth gimbal at 30 degrees tilt. Since the inner gimbal is external to the model, the gimbal falls within the field of view but is painted black to reduce interference.

Celestial sphere performance characteristics are as follows:

Position accuracy	30 minutes of arc
Maximum angular velocity	60 degrees/second

Star field occultation behind the earth is accomplished by blanking the star field by a television matting technique for the window display.

Table 4-2. Navigational Star List

No.	Star Name	Star	Mag.	ψ_{RA}°*	θ_{DA}°*	X**	Y**	Z**
1	Andromedae	α	2.1	1.50	+28.88333	+0.8756980	+0.0255300	+0.4821838
2	Ceti	β	2.2	10.50	-18.18333	+0.9340914	+0.1731730	-0.3122248
3	Cassiopeiae	γ	2.2	13.50	+60.45000	+0.4753107	+0.1144205	+0.8723461
4	Eridani (Archernar)	α	0.6	24.00	-57 41667	+0.4899518	+0.2212398	-0.8432082
5	Ursae Minoris	α	2.1	29.50	+89.10000	+0.0132289	+0.0077645	+0.9998823
6	Eridani	θ	3.4	44.25	-40.43333	+0.5452236	+0.5311876	-0.6485144
7	Ceti	α	2.8	45.00	+03.93333	+0.7060376	+0.7049554	+0.0674439
8	Persei	α	1.9	50.50	+49.73333	+0.4137582	+0.4948081	+0.7641787
9	Tauri	α	1.1	68.50	+16.43333	+0.3587124	+0.8890657	+0.2844075
10	Orionis	β	0.3	78.00	-08.25000	+0.2034766	+0.9684777	-0.1436950
11	Aurigae	α	0.2	78.25	+45.95000	+0.1424605	+0.6780623	+0.7210662
12	Carinae	α	-0.9	95.75	-52.66667	-0.0594701	+0.6038096	-0.7949071
13	Canis Majoris	α	-1.6	101.00	-16.66667	-0.1833847	+0.9407782	-0.2851428
14	Canis Minoris	α	0.5	114.25	+05.31667	-0.4048643	+0.9095903	+0.0934363
15	Velorum	γ	1.9	122.00	-47 23333	-0.3608726	+0.5757248	-0.7336974
16	Ursae Majoris	α	3.1	132.50	+48.50000	-0.4605558	+0.4793006	+0.7471006
17	Hydrae	α	2.2	141.50	-08.50000	-0.7740025	+0.6155832	-0.1482477
18	Leonis (Regulus)	α	1.3	151.50	+12.15000	-0.8576723	+0.4686351	+0.2116113
19	Leonis	β	2.2	176.75	+14.76667	-0.9641096	+0.0570049	+0.2593129
20	Corvi	γ	2.8	183.25	-17 33333	-0.9532064	-0.0607634	-0.2961509
21	Crucis	α	1.6	186.00	-62.81667	-0.4521151	-0.0518945	-0.8904487
22	Virginis (Spica)	α	1.2	200.75	10.96667	-0.9172417	-0.3497841	-0.1905748
23	Ursae Majoris	η	1.9	206.50	+49.50000	-0.5810470	-0.2880196	+0.7612024
24	Centauri	θ	2.3	211 00	-36.18333	-0.6892411	-0.4203341	-0.5901407
25	Bootis (Arcturus)	α	0.2	213.50	+19.36667	-0.7871330	-0.5189878	+0.3332766
26	Coronae Borealis	α	2.3	233.25	+26.83333	-0.5321598	-0.7152388	+0.4530335
27	Scorpii (Antares)	α	1.2	246.75	-26.35000	-0.3529061	-0.8250144	-0.4413713
28	Trianguli Austr.	α	1.9	250.75	-68.93333	-0.1154778	-0.3416209	-0.9327165
29	Ophiuchi	α	2.1	263.25	+12.58333	-0.1128070	-0.9696640	+0.2168556
30	Lyrae (Vega)	α	0.1	279.00	+38.75000	+0.1212117	-0.7683513	+0.6284458
31	Sagittarii	σ	2.1	283.25	-26.33333	+0.2065864	-0.8728720	-0.4420594
32	Aquilae (Altair)	α	0.9	297 25	+08.76667	+0.4530032	-0.8780522	+0.1543130
33	Capricorni	β	3.2	304.75	-14.90000	+0.5517077	-0.7936649	-0.2563487
34	Pavonis	α	2.1	305.75	-56.85000	+0.3195231	-0.4434948	-0.8373872
35	Cygni (Deneb)	α	1.3	310.00	+45.15000	+0.4517525	-0.5368893	+0.7125094
36	Pegasi	ε	2.5	325.50	+09.70000	+0.8133035	-0.5561560	+0.1709619
37	Piscis Austr.	α	1.3	344.00	-29.81667	+0.8347562	-0.2399939	-0.4955653

*Based on ephemeris for 1960.
**Components of star line of sight resolved in I-frame based on actual simulator optical subsystem alignment with celestial sphere.

4.3 SEXTANT DISPLAY

Simulation of sextant operation utilizes electronic generation of two characters which are displayed on an oscilloscope. One of the characters generated is a simulated star that responds to both spacecraft attitude rotations and optic hand controller inputs. The second character is a simulated landmark and responds only to attitude rotational inputs. All rotational inputs to the oscilloscope are simulated by X-Y displacement of the characters on its face. The scanning telescope and sextant and the controls and displays for their control are located in the lower equipment bay shown in Figures 1-5 and 4-1. The shaft and trunnion angles from these viewing devices are part of the input data to an onboard digital command module computer (CMC).

4.4 EXTERNAL VISUAL DISPLAY SYSTEM DRIVES

The earth model is driven through a polar axis and an orbit axis to generate the changing view which would be presented to an observer within the spacecraft because of its translation over the surface of the earth. The shaft and trunnion angles of the simulated scanning telescope and sextant are fixed but the apparent movement of their respective lines-of-sight (LOS) and the motion of the spacecraft with respect to inertial space are simulated by rotating the optical probe's LOS relative to the earth model, rotating the earth model, and rotating the celestial sphere model to provide apparent star motion. Scanning telescope and sextant reticle motions are accomplished by driving simulated reticles.

All rotational commands are generated in the form of position signals, except for the orbital axis drive signal which is a rate command and is only required for elliptical orbits.

Due to a system constraint, simultaneous presentations cannot be made at the window and telescope; therefore, initial positioning and drive signals are developed for both situations.

The coordinate axis frames required to define the relative orientations of the various coordinate systems consist of "real world" frames and simulation frames. The real world frames are inertial, earth, geocentric, local geocentric, heading, body, navigational base, telescope, sextant, and a subject LOS frame. The simulation frames are television monitor, television camera, zeroed gimbal axis, gimbal axis, celestial sphere, and a probe line-of-sight frame.

Each frame is composed of a right-hand orthogonal axis set. The real world frames are defined in Section 3.0 of this document. The simulation frames (frames whose orientations are due entirely to hardware considerations) are defined in paragraph 4.1 and illustrated in Figures 4-2, 4-3, and 4-4.

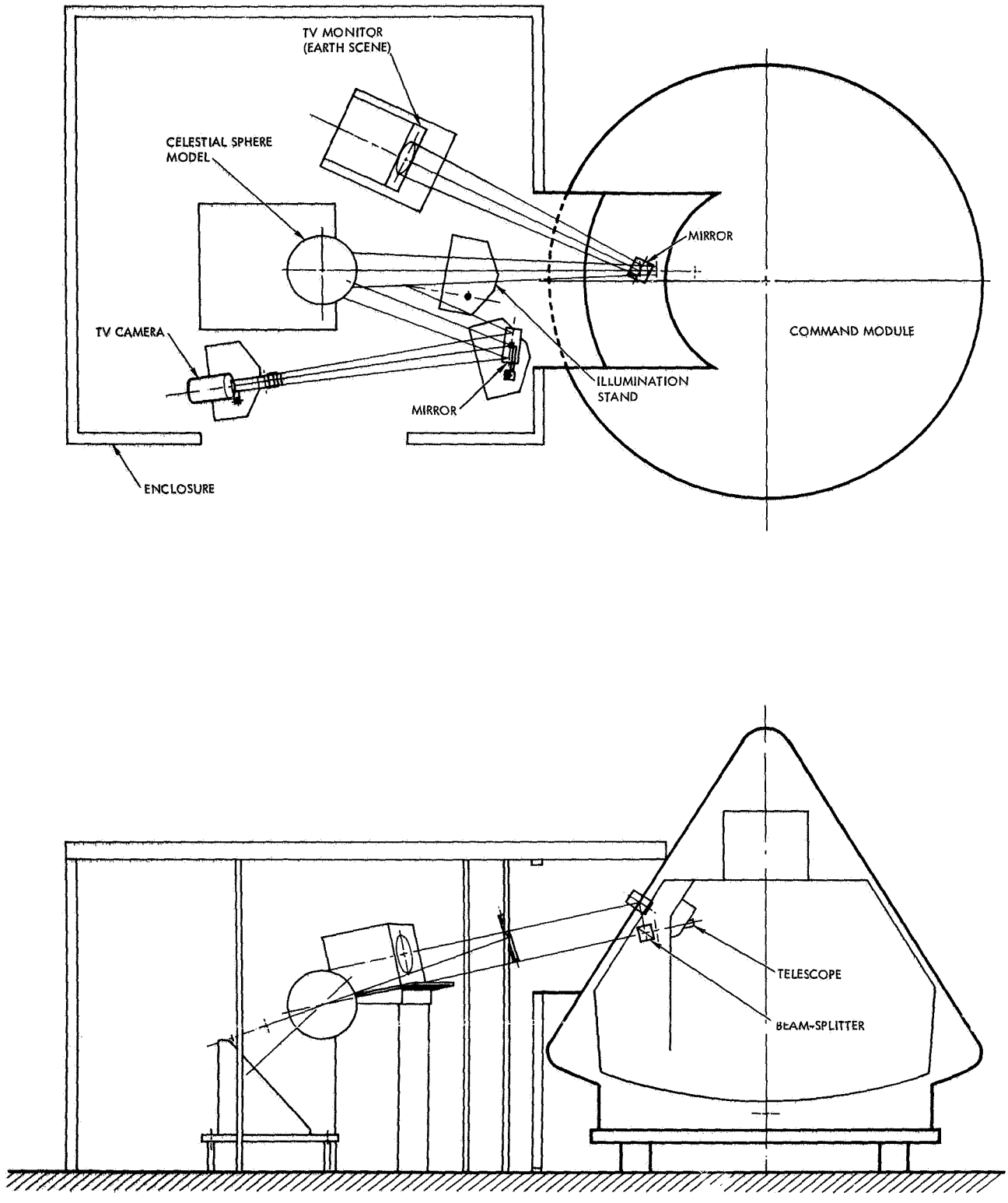

Figure 4-1. Sextant and Scanning Telescope Display Layout

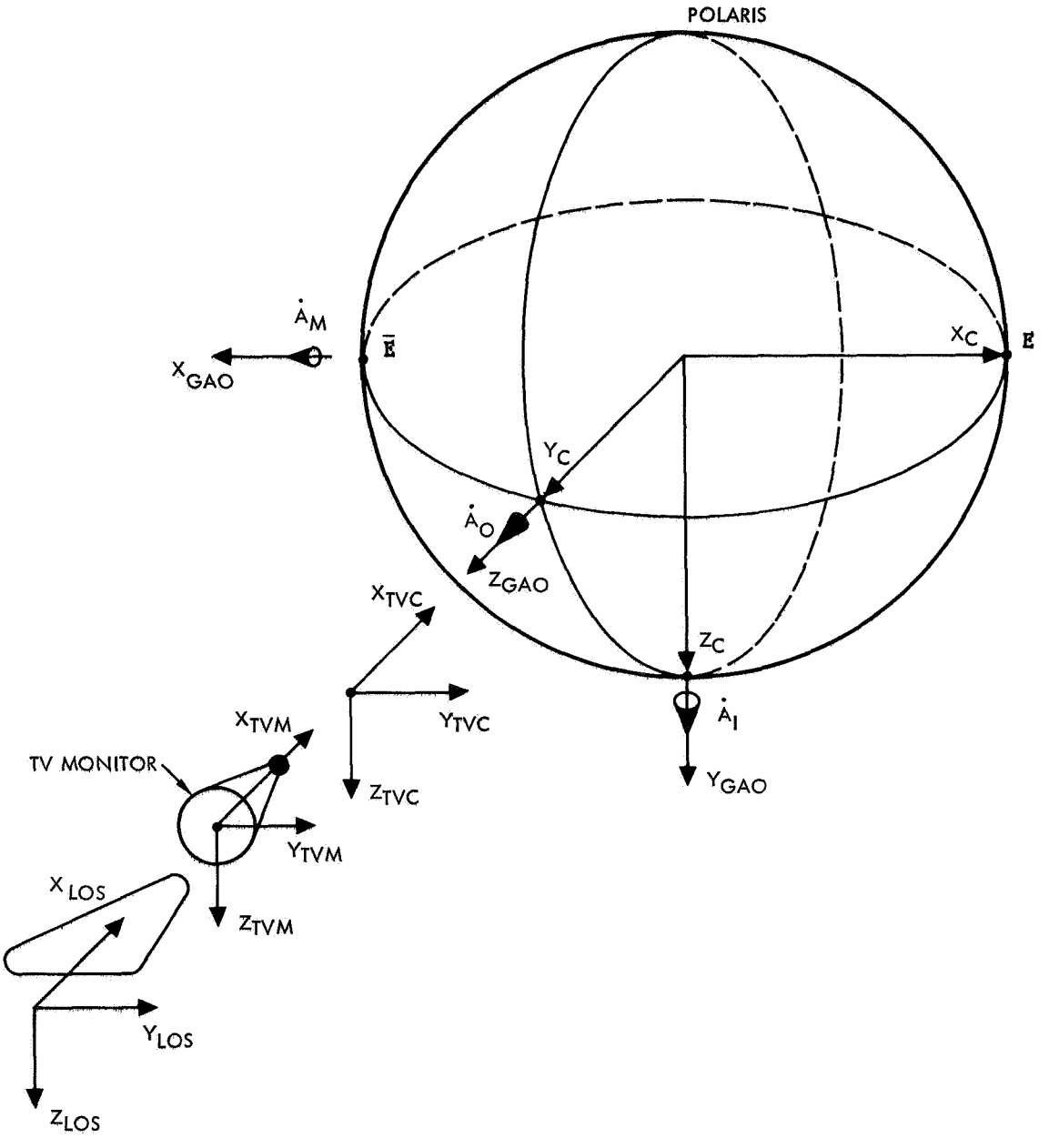

Figure 4-2. Celestial Sphere Diagram Showing LOS-Frame, TVM-Frame, TVC-Frame, GAO-Frame, and C-Frame

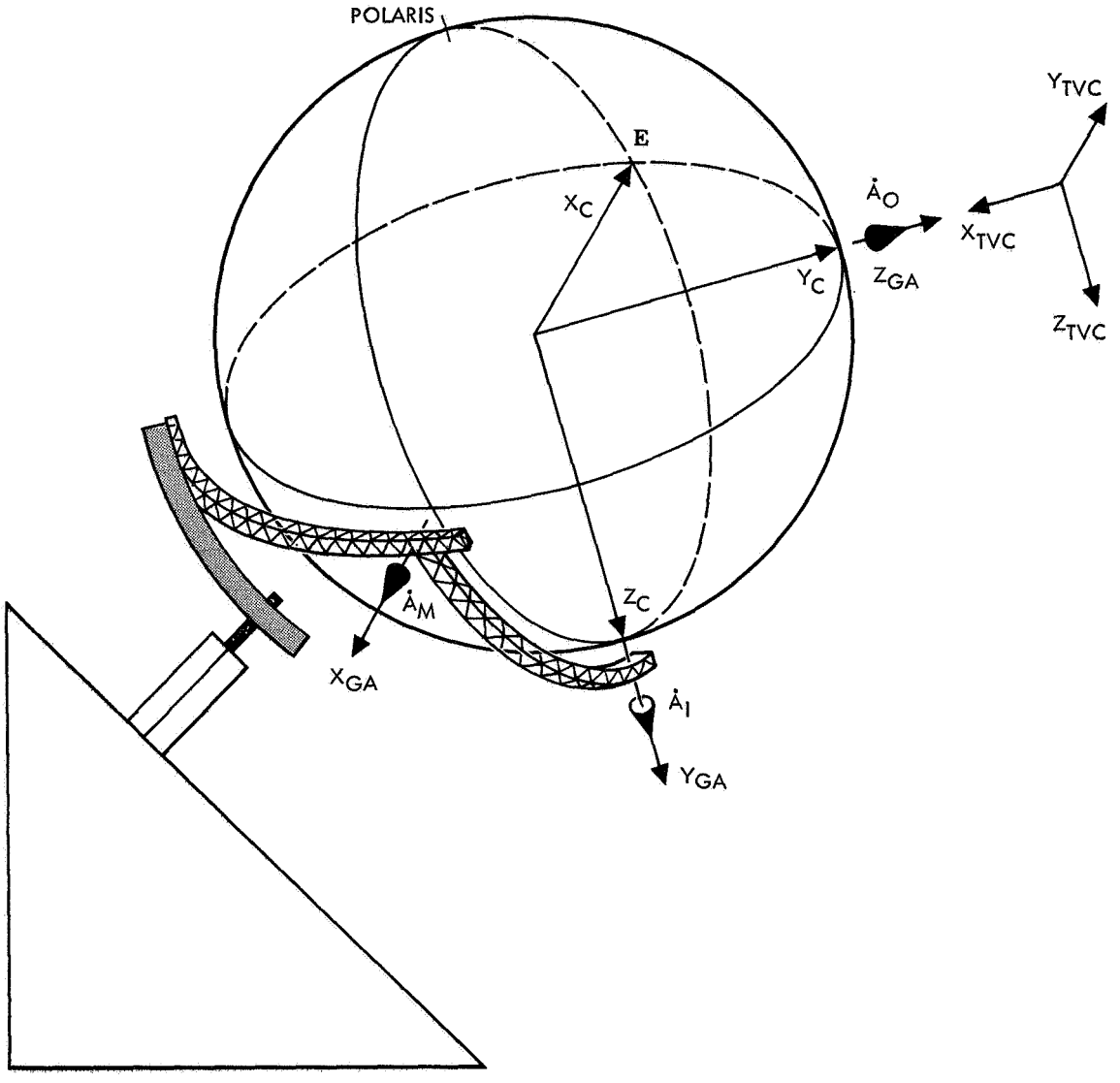

Figure 4-3. Celestial Sphere Diagram Showing GA-Frame, C-Frame, and TVC-Frame

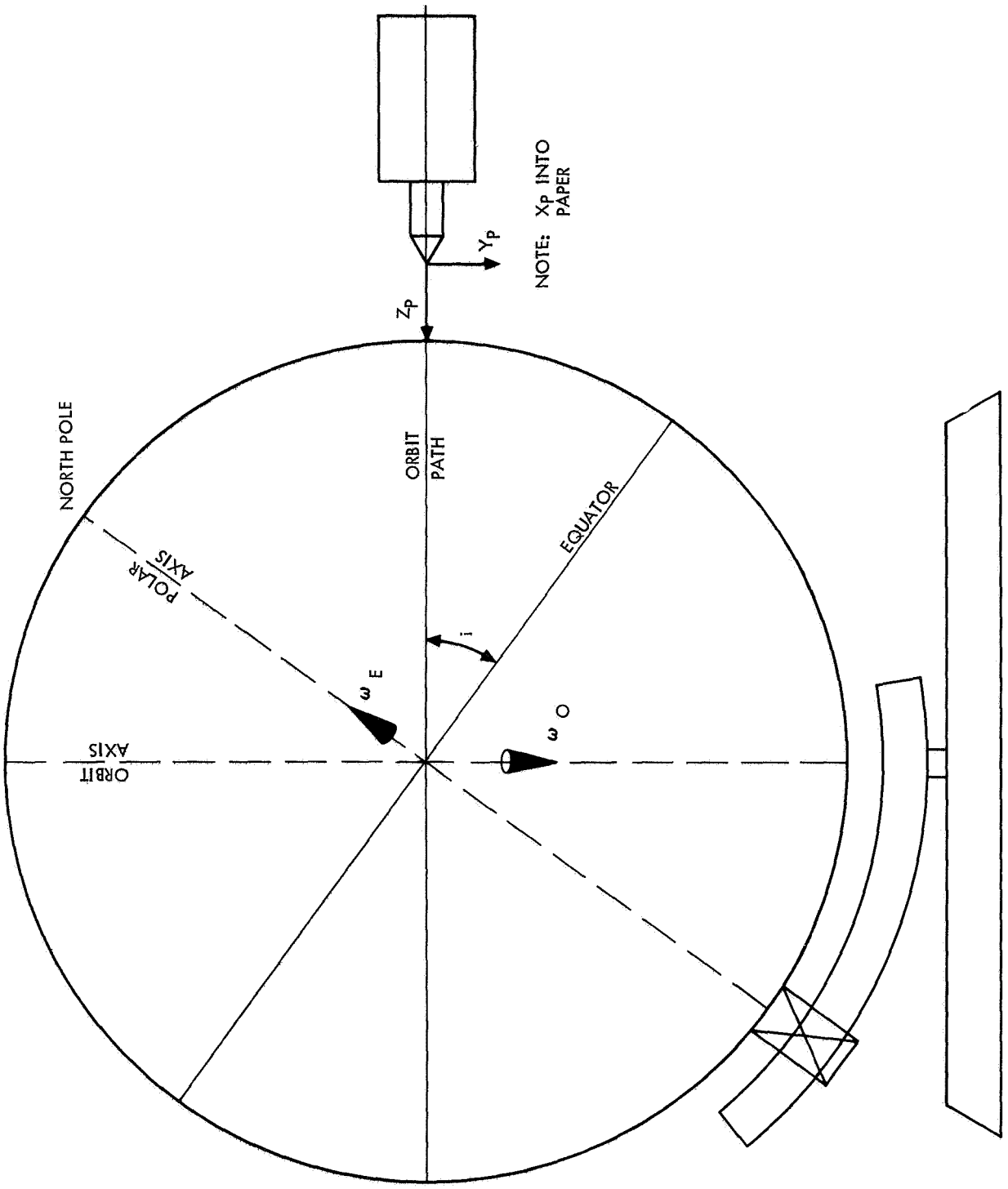

Figure 4-4. Earth Model Diagram Showing Orbit Drive Axis, Polar Drive Axis, and Optical Probe

4.5 DISPLAY REFERENCE FRAMES

1. Television Monitor, TVM-Frame (X_{TVM}, Y_{TVM}, Z_{TVM})

   The TVM-frame has its origin in the center of the tube's viewing surface. The X_{TVM} axis is parallel to the tube's longitudinal axis and positive out the back of the tube. The Z_{TVM} axis is positive down. This system is oriented with respect to the LOS frame by an angle ϕ_{TVM}. This frame is shown in Figure 4-2.

2. Television Camera, TVC-Frame (X_{TVC}, Y_{TVC}, Z_{TVC})

   The TVC-frame has its origin at the center of the camera's vidicon face. The X_{TVC} axis is parallel to the vidicon tubes longitudinal axis and is positive out the front of the tube. The Z_{TVC} axis is positive down and points through the bottom of the tube. The Y_{TVC} axis completes the right-hand set. The TVC-frame is oriented with respect to the TVM-frame so that $X_{TVC} = X_{TVM}$, $Y_{TVC} = +Y_{TVM}$, and $Z_{TVC} = +Z_{TVM}$ as shown in Figure 4-2.

3. Gimbal Axis, Zeroed, GAO-Frame (X_{GAO}, Y_{GAO}, Z_{GAO})

   The GAO-frame has its origin at the center of the celestial sphere model gimbal structure. The GAO-frame is oriented with respect to the TVC-frame as follows: $X_{GAO} = -Y_{TVC}$, $Y_{GAO} = Z_{TVC}$, and $Z_{GAO} = -X_{TVC}$ as shown in Figure 4-2.

4. Gimbal Axis, GA-Frame

   The GA-frame has its origin at the center of the celestial sphere model. The X_{GA} axis coincides with the middle gimbal axis, Y_{GA} coincides with the inner gimbal axis, and Z_{GA} coincides with the outer gimbal axis. The GA-frame rotates with respect to the GAO-frame through the angles A_O, A_M, and A_I. The GA-frame is shown in Figure 4-3.

5. Celestial Sphere, C-Frame (X_C, Y_C, Z_C)

   The C-frame has its origin at the center of the celestial sphere model. The X_C and Y_C axes lie in the celestial spheres equatorial plane. The X_C axis is directed at the vernal equinox, Z_C is directed at the south celestial pole parallel to the earth's polar axis, and Y_C completes the right-handed triad. The C-frame is oriented with respect to the GA-frame for $A_O = A_M = A_I = 0$ so that $X_C = -X_{GA}$, $Y_C = Z_{GA}$, and $Z_C = Y_{GA}$ as shown in Figure 4-3.

6. Probe LOS Zeroed, PO-Frame (X_{PO}, Y_{PO}, Z_{PO})

   Because of the inability of the probe to be driven at a sufficient rate for tracking when at or near the zero-zero position, the probe is physically mounted at an offset angle by rotating about the Y_{PO} axis through an angle A_{LOS}. To align the LOS, an additional 90 degrees is added to the A_{LOS} angle as a bias.

   The PO-frame has its origin at the nodal point of the probe's head prism. The Z_P axis is coincident with the probe's centerline and positive out. The Y_P axis is perpendicular to the probe's mounting base and positive through the base. The X_P is the LOS axis and completes the right-hand set.

7. Probe LOS, P-Frame (X_P, Y_P, Z_P)

   The P-frame is oriented with respect to the PO-frame by probe angles ϕ_P, ψ_P, and θ_P.

   The PO-frame is one-to-one with the P-frame for $\theta_P = \psi_P = \phi_P = 0$

8. Optics, O-Frame (X_O, Y_O, Z_O)

   The origin of the O-frame is in the simulated SCT. The SCT optics inverts the scene viewed through it and requires a 180-degree rotation for scene erection.

5.0 SIMULATED SCS ELECTRONICS AND SPS GIMBAL DYNAMICS

This section contains analytical models of SCS components for which prototype hardware was not available or its incorporation was not feasible. Also included are the TVSA and actuator models. Descriptions of the special-purpose electronics for EMS moding, SCS and SPS moding, and propellant accounting are also included.

The subsections that follow are numbered to correspond to the numbers in the blocks of Figure 1-6.

In most cases (i.e., blocks 2 through 6) a single analytical model is presented as representative of both the pitch and yaw channels in the case of the TVSA and actuator, and all three channels in the case of the GA and CEA. The constants, variables, and moding switches are listed according to channel in Tables 5-1, 5-2, and 5-3, respectively.

5.1 EMS MODE SWITCHING

The entry monitor system is simulated in three different parts, not including the instrument display in the evaluator.

The EMS accelerometer input is computed in Section 2 on the analog computer. The stability roll angle and velocity requirements of the EMS display are provided by the "9300." The sine and cosine of the stability roll angle are taken from the hardware GDC output. The 9300 computes the driving signal to the GDC shaft resolver stepper motor based on the returns from the GDC output and the internally calculated stability roll angle. (Refer to Section 3, paragraph 3.1.27.)

The EMS moding logic, however, is simulated on a HYDAC, which is patchable logic. The moding logic performs the same functions as the actual EMS hardware and is therefore not described herein.

5.2 GYRO ASSEMBLIES 1 AND 2

Two body-mounted attitude gyros (BMAG's) are simulated for each axis. BMAG 1 is normally in an attitude-sensing mode and BMAG 2 is normally in a rate-sensing mode. Switching is available for failing either gyro and, in case of failure in BMAG 2, BMAG 1 may be switched to its rate mode.

Table 5-1. Mathematical Model Constants

Symbol		Magnitude	Units	Description
Block Diagram	Analog Mech.			
G_1		124.4	deg/sec/deg	Backup (BMAG) torque gain
G_2		0.5	ND	Attitude error gain
G_3		10.0	ND	Attitude error gain
G_4		0.495	ND	MTVC rate filter gain
G_5		0.4	deg/sec	MTVC rate command gain
G_6		0.38386	ND	Roll to yaw coupling gain
G_7		0.125	ND	MTVC integrator gain
G_8		0.3115	ND	TVC LM-off attitude gain
G_9		0.166	ND	TVC LM-on attitude gain
G_{10}		0.372	ND	TVC LM-on integrator gain
G_{11}		0.399	ND	LM-off rate gain
G_{12}		0.998	ND	LM-on rate gain
G_{13}		0.0565	ND	TVC integrator gain
G_{14}	K_{SA}	2000.0	MA/rad	Servo amp gain
G_{15}	K_{CI}	3.5	lb/MA	Clutch dynamics gain
G_{16}	$K_{\dot{\delta}T}$	0.985 (yaw) 0.943 (pitch)	sec	TACH-XDCR and demodulator gain
G_{17}	K_{PO}	1.0	rad/rad	Position-XDCR and demodulator gain
G_{18}	K_{ST}	7.17×10^{-5} (yaw) 7.55×10^{-5} (pitch)	rad/sec/lb-ft	Speed-torque gain
G_{19}		1.0	ND	Rate gain
G_{20}		10.0	ND	Rate gain
G_{21}		1.75×10^6	lb/rad/sec	Gain of variable motor rate limiter
G_{22}		7.02×10^6	lb/rad	Gain of gimbal deflection limiter

Table 5-1. Mathematical Model Constants (Cont)

Symbol		Magnitude	Units	Description
Block Diagram	Analog Mech.			
τ_1		0.0163	sec	Backup (BMAG) time constant
τ_2		0.01	sec	Attitude error amp time constant
τ_3		0.01	sec	Summing amp time constant
τ_4		1.0	sec	Pseudo rate time constant
τ_5		0.025	sec	Rotary stick amp time constant
τ_6		0.6165	sec	Notch filter time constant
τ_7		0.7299	sec	Notch filter time constant
τ_8	τ_{14}	0.0268	sec	Clutch dynamics time constant
τ_9	τ_{15}	0.0326	sec	Clutch dynamics time constant
τ_{10}	τ_{16}	0.0038	sec	Clutch dynamics time constant
τ_{11}	$\tau_{\delta T}$	0.00151	sec	Tachometer XCDR and demodulator time constant
τ_{12}	τ_{13}	0.00794	sec	Actuator position transceiver time constant
τ_{13}	τ_{ST}	0.1	sec	Speed-torque time constant
ω_1		87.5	rad/sec	Rate gyro natural frequency
ω_2		48.9	rad/sec	MTVC rate filter natural frequency
ω_3		40.7	rad/sec	TVC LM-off shaping filter natural frequency
ω_4		29.0	rad/sec	TVC LM-on shaping filter natural frequency
ω_5		4.98	rad/sec	TVC notch filter natural frequency
ω_6		5.57	rad/sec	TVC notch filter natural frequency

Table 5-1. Mathematical Model Constants (Cont)

Symbol		Magnitude	Units	Description
Block Diagram	Analog Mech.			
ω_7		0.002	rad/sec	TVC integrator frequency constant
ω_8		0.212, 0.206	rad/sec	Pitch, yaw, no load rate limits
D_1		0.352	ND	Rate gyro damping ratio
D_2		0.773	ND	MTVC rate filter damping ratio
D_3		0.805	ND	TVC LM-off shaping filter damping ratio
D_4		0.489	ND	TVC LM-on shaping filter damping ratio
D_5		0.198	ND	TVC notch filter damping ratio
D_6		2.433	ND	TVC notch filter damping ratio
D_7		1000.0	ft-lb-sec	Actuator effective damping
L_1		+16.0, -16.0	deg	BMAG output limit
L_2		+50.0, -50.0	deg/sec	Backup BMAG rate limiter
L_3		+50.0, -50.0	deg/sec	Rate gyro output limit
L_4		+15.0, -14.0	deg	Attitude error limiter
L_5		+29.0, -25.0	deg/sec	Rate limiter
L_6		+14.0, -10.0	deg	MTVC command limit
L_7		+5.6, -4.7	deg	TVC integrator limit
L_8		+14.0, -10.0	deg	SCS gimbal command limit
L_9		+600.0, -600.0	MA	Servo amp limiter
L_{10}		+0.0785, -0.0785	rad	Gimbal position limiter

Table 5-1. Mathematical Model Constants (Cont)

Symbol		Magnitude	Units	Description
Block Diagram	Analog Mech.			
H_1		+2.0, -2.0	deg/sec	Rate deadband
H_2		0.07	deg/sec	Rate hysteresis
H_3		+4.0, -4.0	deg	Attitude error deadband
J	J_θ, J_ψ	304, 313	slug-ft^2	Main engine moment of inertia
R	R_θ, R_ψ	1.0	ft	Effective actuator lever arm
	δ_{bias}	0.0	rad	Engine gimbal bias
	$(\delta_\theta, \delta_\psi)_{TRIM}$	-2.0, 1.0	rad	Engine gimbal trim
	ϵ_T		rad	Engine thrust misalignment
	ϵ_θ		rad	Center of gravity uncertainty on thrust alignment

Table 5-2. Mathematical Model Variables

Symbol		Magnitude Range	Units	Description
Block Diagram	Analog			
H_4	ω_{NL}		rad/sec	Variable rate limiter
	F_{C_ψ}, F_{C_θ}		lb	Clutch force (yaw, pitch)
	ϕ_d, θ_d, ψ_d		deg	Display attitude (roll, pitch, yaw)
	$p_{d1AC}, q_{d1AC}, r_{d1AC}$		deg/sec	AC Rate 1 (roll, pitch, yaw)
	$p_{d2AC}, q_{d2AC}, r_{d2AC}$		deg/sec	AC Rate 2 (roll, pitch, yaw)
	p_f, q_f, r_f		deg/sec	Sensed body axis rates (roll, pitch, yaw)
	$\delta_{\psi CC}, \delta_{\theta CC}$	+4.80 deg to -4.8 deg	rad	CMC steering command (yaw, pitch)
	$\delta_{\psi D}, \delta_{\theta D}$		rad	Display actuator position (yaw, pitch)
	$\delta_\psi, \delta_\theta$	+4.80 deg to -4.8 deg	rad	Engine gimbal angle (yaw, pitch)
	$\ddot{\delta}_\psi, \ddot{\delta}_\theta$	+4.28 deg/sec to -4.8 deg/sec^2	rad/sec^2	Engine gimbal acceleration (yaw, pitch)
	$F_{\psi DWT}, F_{\theta DWT}$		lb	Dog-wags-tail force (yaw, pitch)
t_1			sec	Electrical command to CM RCS jets
t_2			sec	Electrical command to SM RCS jets
$\dot{\omega}_{CM}$			lb/sec	CM RCS propellant flow rate per jet
$\dot{\omega}_{SM}$			lb/sec	SM RCS propellant flow rate per jet

Table 5-3. Mode Logic Switches

Logic Switch*	Function	Logical Condition
QS21	Attitude signal enable (roll, pitch, yaw)	(See Honeywell Document)
QS28	Rate 1 enable (roll, pitch, yaw)	C 12989-5
QS29	Rate 2 enable (roll, pitch, yaw)	
QS25	High rate enable (roll, pitch, yaw)	
QS32	RJC proportional enable (roll, pitch, yaw)	
QS30	MTVC integrator enable (pitch, yaw)	
QS1	TVC manual command enable	
QS2	SCS gimbal command enable	
QS3	Gimbal trim enable	
QS11	LM-off gain enable (pitch, yaw)	
QS12	LM-on gain enable (pitch, yaw)	
QS26	Cross coupling enable (roll, yaw)	
QS44	Pseudo rate disable (roll, pitch, yaw)	
K30	MTVC Rate 2 enable (pitch, yaw)	
K31	MTVC Rate 1 enable (pitch, yaw)	
K22	Minimum deadband enable (roll, pitch, yaw)	
K25	High rate enable (roll, pitch, yaw)	
K11	TVC integrator enable (pitch, yaw)	
K2	Servo No. 2 engage (pitch, yaw)	(ME 101 software logic,)
SR1	GA 1 power on	IL 190-600-BII-67-018
SR2	GA 2 power on	
SR3	ECA ac power	
SR4	ECA ac Bus 2 power	
PP, YP	Pitch, yaw servo power	

*Logic switches starting with Letters "Q" or "K" are preceded by a number 1, 2, or 3 for designation of roll, yaw, or pitch CEA channel (see Honeywell document).

Only one channel is represented in the flow diagram of Figure 5-1. The other two channels are identical to this channel. However, the constants, variables, and moding switches are defined on a per-channel basis in Tables 5-1, 5-2, and 5-3, respectively.

The sensed body rate at the input is the body rate calculated on the analog computer, modified by bending oscillations. (Refer to Section 2, paragraph 2.19.)

The indicated scaling blocks represent the voltage adjustments required to interface properly with the prototype hardware.

5.2.1 Gyro Output Limit (GA1)

$$\boxed{\begin{array}{c}\text{Deadband} \sim L_1 \\ \hline \text{Gain} = 1.0\end{array}}$$

5.2.2 Gyro Torque Gain (GA1 in Rate Mode)

$$\boxed{G_1}$$

5.2.3 Torque Rate Limiter (GA1 in Rate Mode)

$$\boxed{\begin{array}{c}\text{Limits} \sim L_2 \\ \hline \text{Gain} = 1.0\end{array}}$$

5.2.4 Torque Loop Lag (GA1 in Rate Mode)

$$\boxed{\frac{1}{\tau_1 S + 1}}$$

5.2.5 Rate Gyro Response (GA2)

$$\boxed{\begin{array}{c}\text{Limits} \sim L_3 \\ \hline \dfrac{1}{\left(\dfrac{S}{\omega_1}\right)^2 + \dfrac{2(D_1)S}{\omega_1} + 1}\end{array}}$$

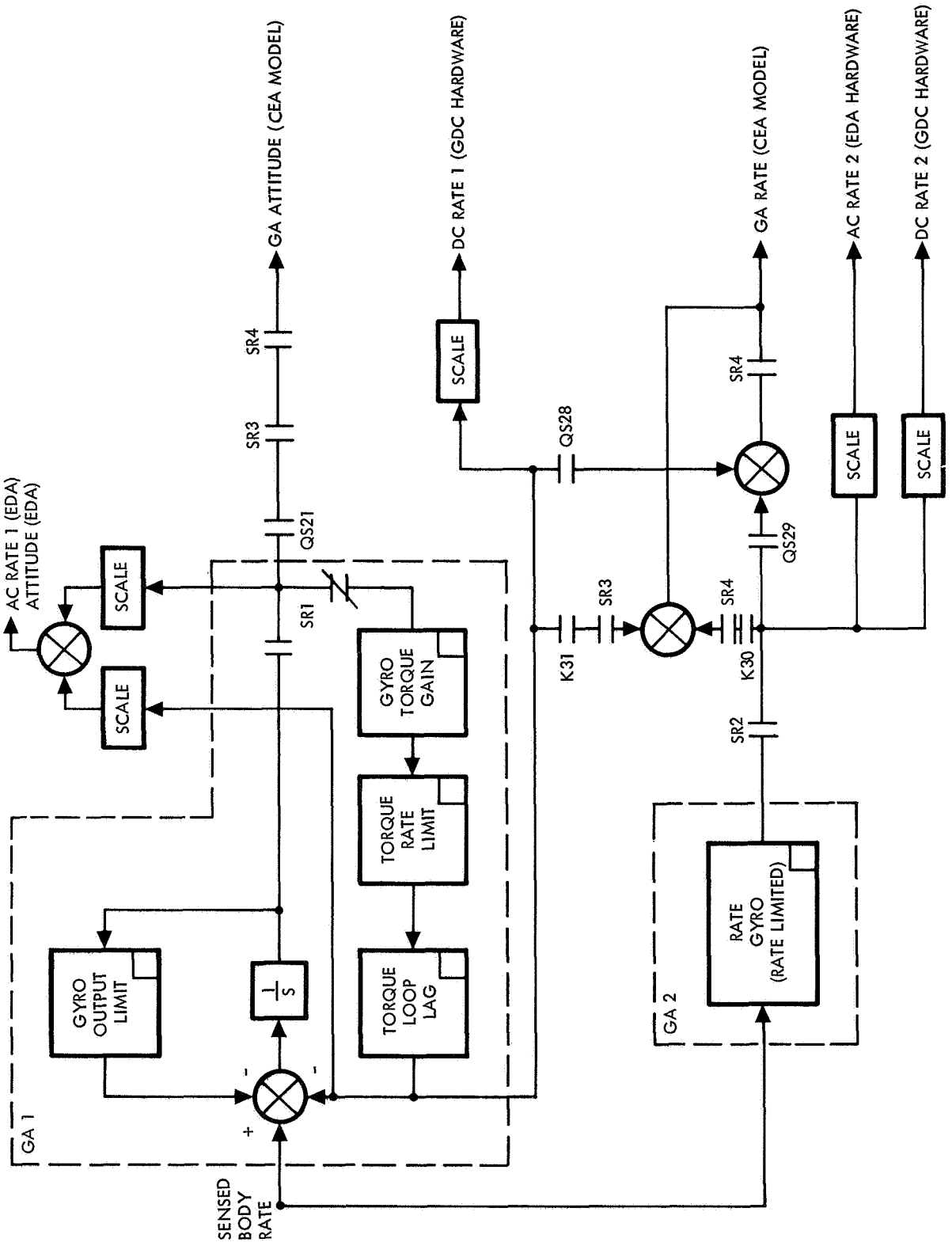

Figure 5-1. Flow Diagram of Gyro Assembly Model

5.3 ELECTRONIC CONTROL ASSEMBLY (CEA)

The CEA is simulated entirely by analog computer representation except for the switching amplifier This is simulated by specially constructed hardware called the "jet select logic," which performs a number of functions. A general flow diagram of the CEA simulator is given in Figure 5-2. A detailed breakdown of the blocks follows with paragraph numbering coinciding with the numbers in the blocks.

5.3.1 MTVC Rate Filter

$$\frac{G_4}{\left(\frac{S}{\omega_2}\right)^2 + \frac{2 D_2 S}{\omega_2} + 1}$$

5.3.2 MTVC Integrator

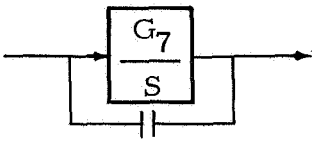

5.3.3 MTVC Command Limiter

Limits L_6
Gain = 1.0

5.3 4 Rotation Controls 1 and 2

Prototype hardware S/N 10028ESK0004

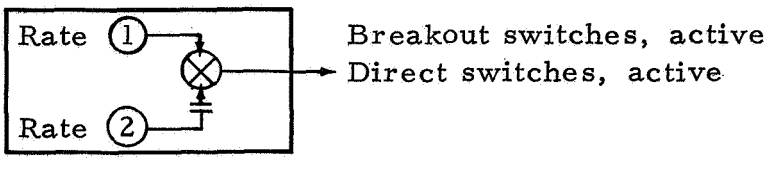

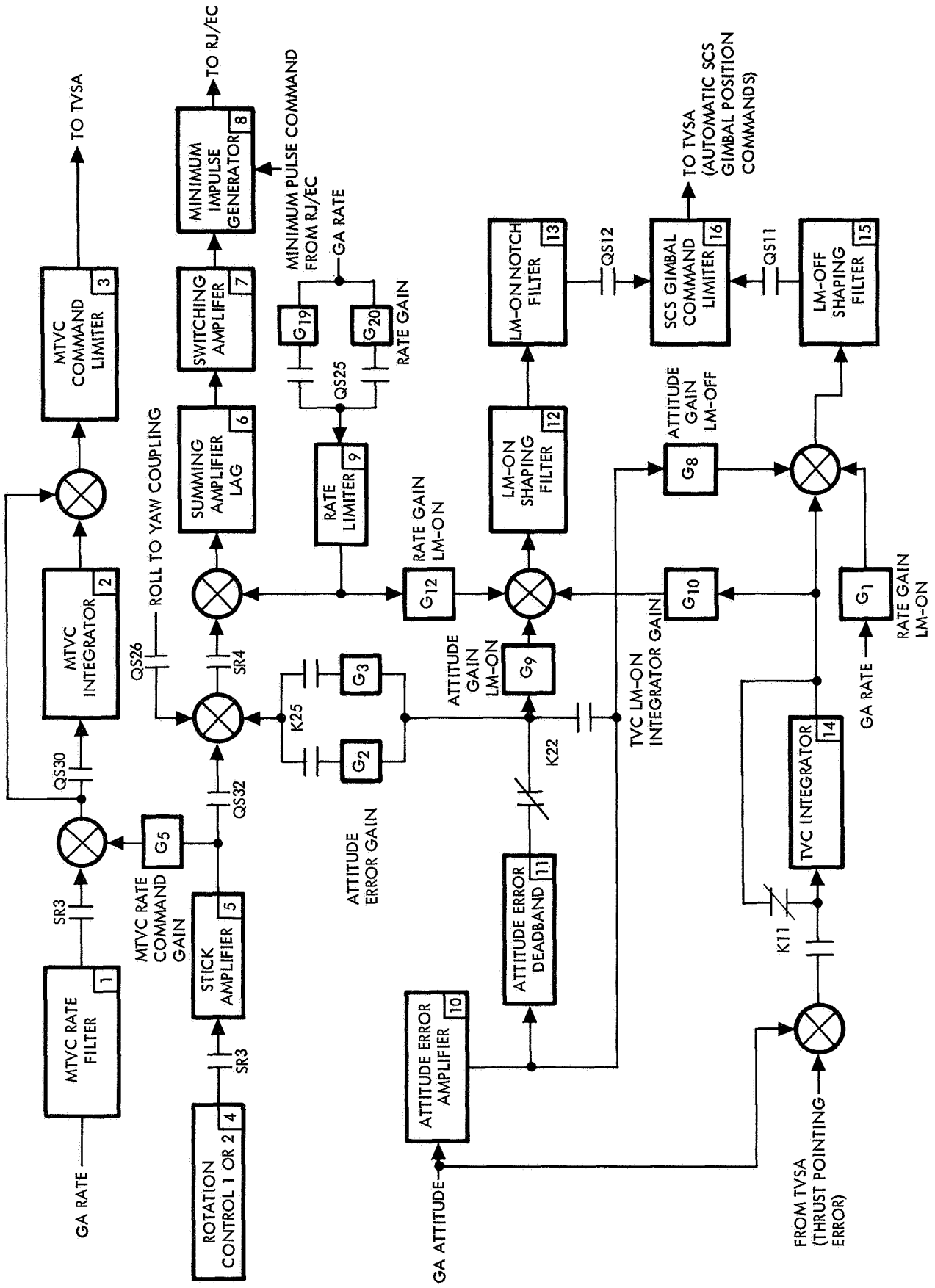

Figure 5-2. Flow Diagram of CEA Model

5.3.5 Stick Amplifier

$$\frac{1}{\tau_5 S + 1}$$

5.3.6 Summing Amplifier Lag

$$\frac{1}{\tau_3 S + 1}$$

5.3.7 Switching Amplifier and Pseudo Rate Feedback

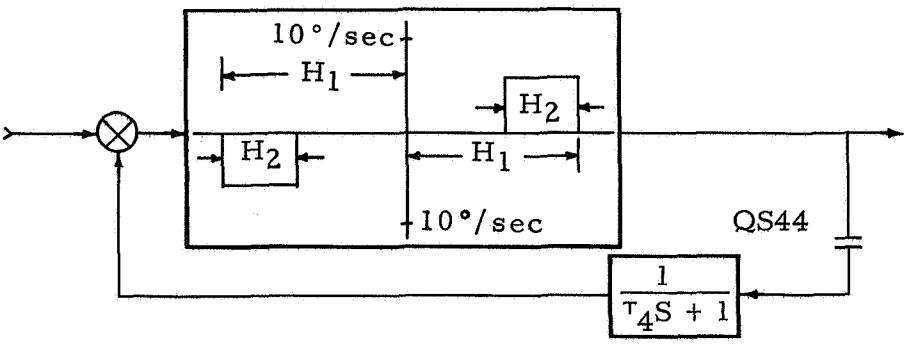

5.3.8 Minimum Impulse Generator

If input is from switching amplifier, the pulse out of the generator has a duration of $\geq T_{M\omega}$. If input is a minimum impulse command from the RJ/EC, the output pulse duration is $T_{M\omega}$.

5.3.9 Rate Limiter

Limits ~ L_5
Gain = 1.0

5.3.10 Attitude Error Amplifier

Limits ~ L_4
$\frac{1}{\tau_2 S + 1}$

5 3.11 Attitude Error Deadband

Deadband H_3
Gain = 1.0

5 3.12 LM-On Shaping Filter

$$\frac{1}{\left(\frac{S}{\omega_4}\right)^2 + \frac{2\,(D_4)\,S}{\omega_4} + 1}$$

5.3.13 LM-On Notch Filter

$$\frac{\left(\frac{S}{\omega_5}\right)^2 + \frac{2(D_5)S}{\omega_5} + 1}{\left(\frac{S}{\omega_6}\right)^2 + \frac{2\,(D_6)\,S}{\omega_5} + 1} \quad \frac{\tau_6 S + 1}{\tau_7 S + 1}$$

5.3 14 TVC Integrator

Limits~L_7
$\frac{G_{13}}{S + \omega_7}$

5 3.15 LM-Off Shaping Filter

$$\frac{1}{\left(\frac{S}{\omega_3}\right)^2 + \frac{2(D_3)\,S}{\omega_3} + 1}$$

5.3.16 SCS Gimbal Command Limiter

Limits~L_8
Gain = 1.0

5.4 TVSA, ACTUATOR, AND GIMBALS

The TVSA, SPS actuators, and gimbal responses are simulated entirely by analog computer models. The functions simulated are given in a flow diagram in Figure 5-3. A detailed breakdown of the blocks follows, with paragraph numbering coinciding with the numbers in the blocks.

5.4.1 Servo Amplifier and Limiter

Limits L_9
Gain = G_{14}

5.4.2 Clutch Dynamics

$$\frac{G_{15}\ (\tau_8 S + 1)}{(\tau_9 S + 1)\ (\tau_{10} S + 1)}$$

5.4.3 Gimbal Acceleration

$$\frac{R}{J}$$

5.4.4 Variable Motor Torque

$$\frac{R\ F_c}{|F|}$$

5.4.5 Torque Lag

$$\frac{G_{18}}{\tau_{13} S + 1}$$

5.4.6 Variable Motor Rate Limiter (A Variable Deadband)

L_{11} →

Deadband ~ L_{11} (variable)
Gain = G_{21}

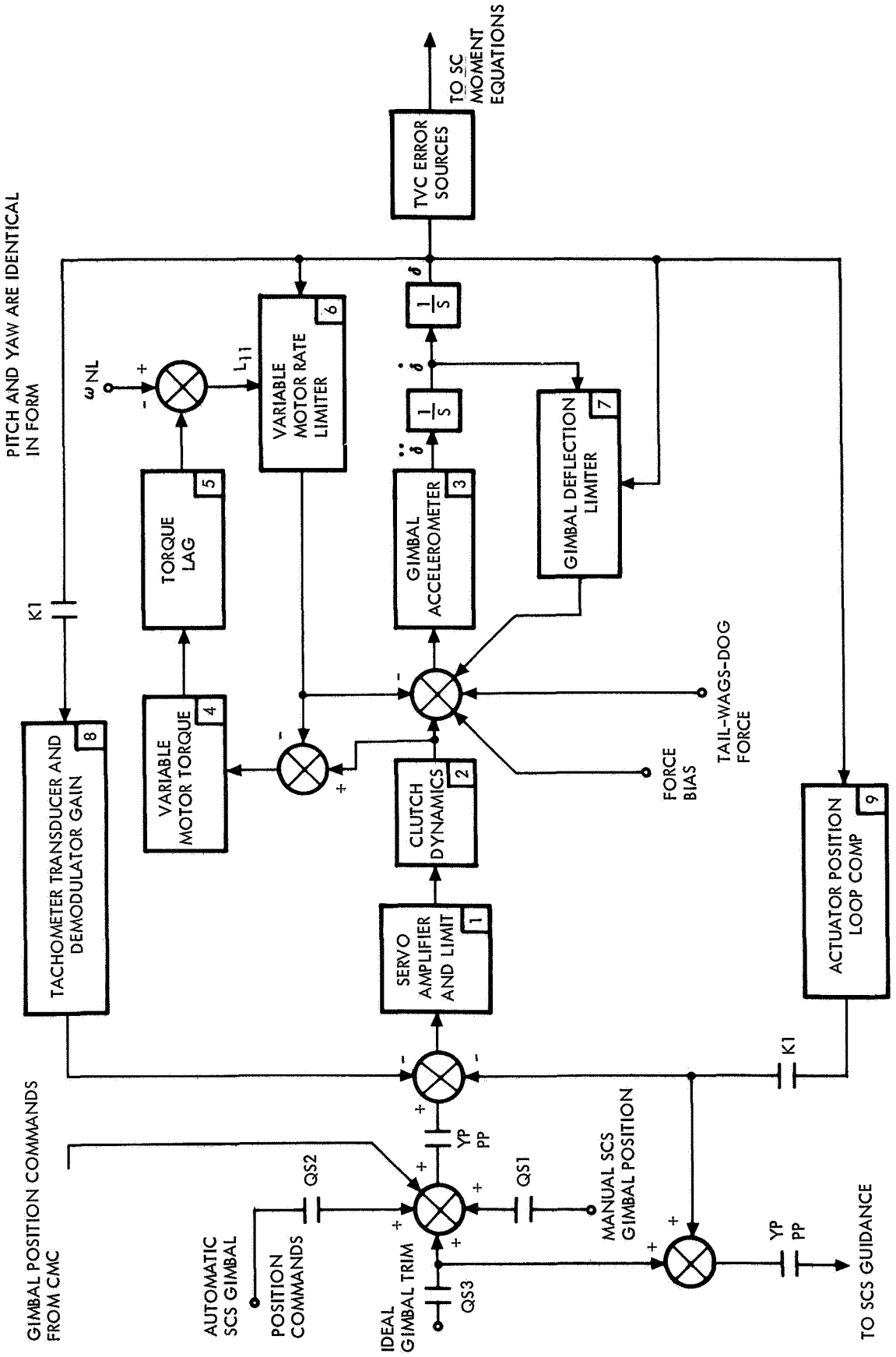

Figure 5-3. Flow Diagram of TVSA and Actuator Model

5.4.7 Gimbal Deflection Limiter

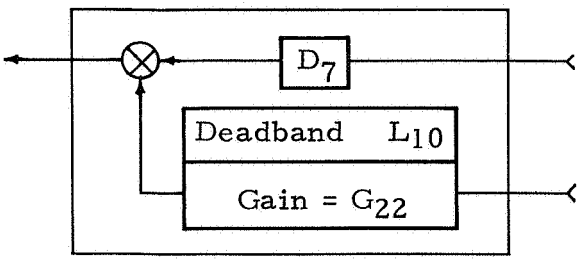

5.4.8 Tachometer Transducer and Demodulator Gain

$$\frac{G_{16}}{\tau_{11}S + 1}$$

5.4.9 Actuator Position Transducer Gain and Lag

$$\frac{G_{17}}{\tau_{12}S + 1}$$

5.4.10 TVC Error Source Location

See Figure 5-4.

5.5 JET SELECT LOGIC

The jet select logic (JSL) is a special-purpose hardware device which simulates the operation of portions of the following SC hardware: electronic control assembly (ECA), reaction jet engine on/off control (RJ/EOC), RCS control box, RCS fuel system, mission events sequence controller (MESC), and the RCS jets themselves. ECA functions include the switching amplifier, pseudo rate feedback generation, and minimum impulse generation. All functions of the RJ/EOC with the exception of the SPS engine on/off logic and the CM/SM jet transfer switch portion of the RCS control box are also simulated in the JSL. The RCS fuel system includes control of SM helium 1 and 2 and SM RCS primary and secondary fuel control valves, and the CM system A and B fuel control valves. MESC functions include CM/SM separation, CSM/LV separation, and RCS/command enable. Provisions are included for shaping of the thrust transmitted to vehicle moment equations consisting of on and off delays for SM automatic, SM direct, and CM automatic or direct jet firings.

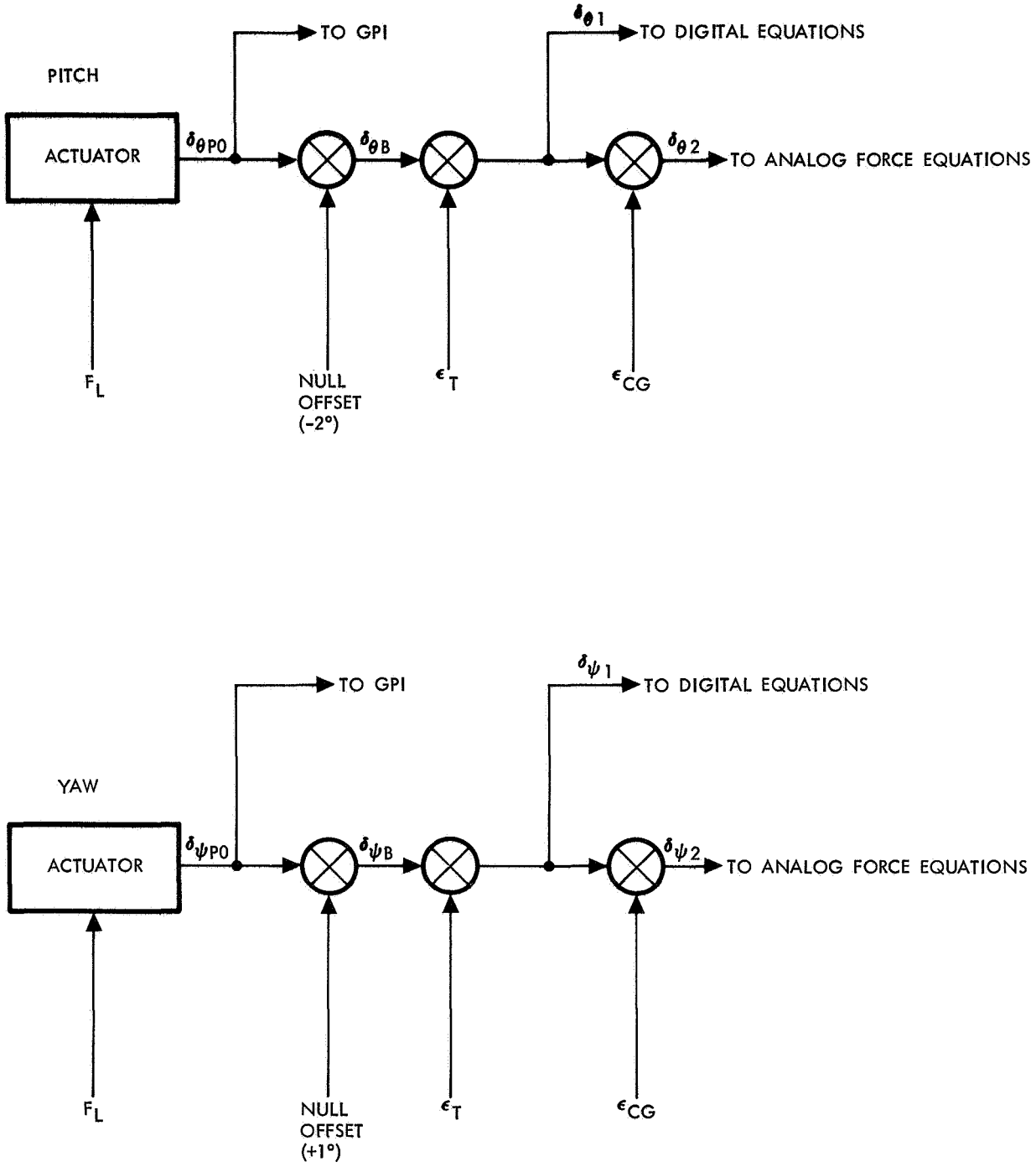

F_L THRUST MISALIGNMENT FORCE = ±510 POUNDS
(THIS ERROR SOURCE IS TO BE INSERTED AT IGNITION)

ϵ_T THRUST MISALIGNMENT ANGLE = ±0.57 DEGREE

ϵ_{CG} CG UNCERTAINTY = ±1 0 DEGREE

(ϵ_T AND ϵ_{CG} MAY BE INSERTED AS INITIAL CONDITIONS)

Figure 5-4. TVC Error Source Location

The JSL receives moding logic signals from the command module, drive signals from the two rotational hand controllers, the translational hand controller and the CMC, and provides drive signals for the SM helium and propellant and command module propellant valve position indicators in addition to jet thrust signals for vehicle moment equations and electrical on/off commands for the fuel accounting system.

In addition, provisions are included for the insertion of various simulated hardware failures. These include switching amplifier on-off failures, solenoid on-off failures, CMC RCS jet command on-off failures, and solenoid on-off failures. (Figure 5-5 shows the JSL relationship to interfacing simulator subsystems.)

5.6 RCS PROPELLANT ACCOUNTING

5.6 1 CM Propellant Flow Rate (Per Jet) ≃ lb/sec

$$\dot{W}_{CM} = 0.2105 \qquad t_1 < 0.020 \text{ sec}$$

$$\dot{W}_{CM} = 0.345 + 0.076\, e^{-21t_1} \qquad t_1 \geq 0.020 \text{ sec}$$

5 6.2 SM Propellant Flow Rate (Per Jet) ≃ lb/sec

$$\dot{W}_{SM} = 0.164 \qquad t_2 < 0.010 \text{ sec}$$

$$= 0.136 \qquad 0.010 \leq t_2 < 0.023$$

$$= 0.123 \qquad 0.023 \leq t_2 < 0.060$$

$$= 0.120 \qquad 0.060 \leq t_2 < 0.100$$

$$= 0.1178 \qquad t_2 \geq 0.100$$

5.7 ORDEAL SIMULATOR

Orbit rate drive earth and lunar (ORDEAL) drives the FDAI AAI pitch axis at the orbit rate as a backup local vertical reference. The only input is estimated average altitude over a circular orbit. The output is the sine and cosine of the desired AAI pitch gimbal angle. The normal DEA output (pitch) is added to the ORDEAL output.

The ORDEAL simulator employs a prototype instrument panel and all functions are provided with in-flight hardware specifications. These specifications are ±10 percent in the output flow rate and ±2 deg/hr in the orbit rate calculation.

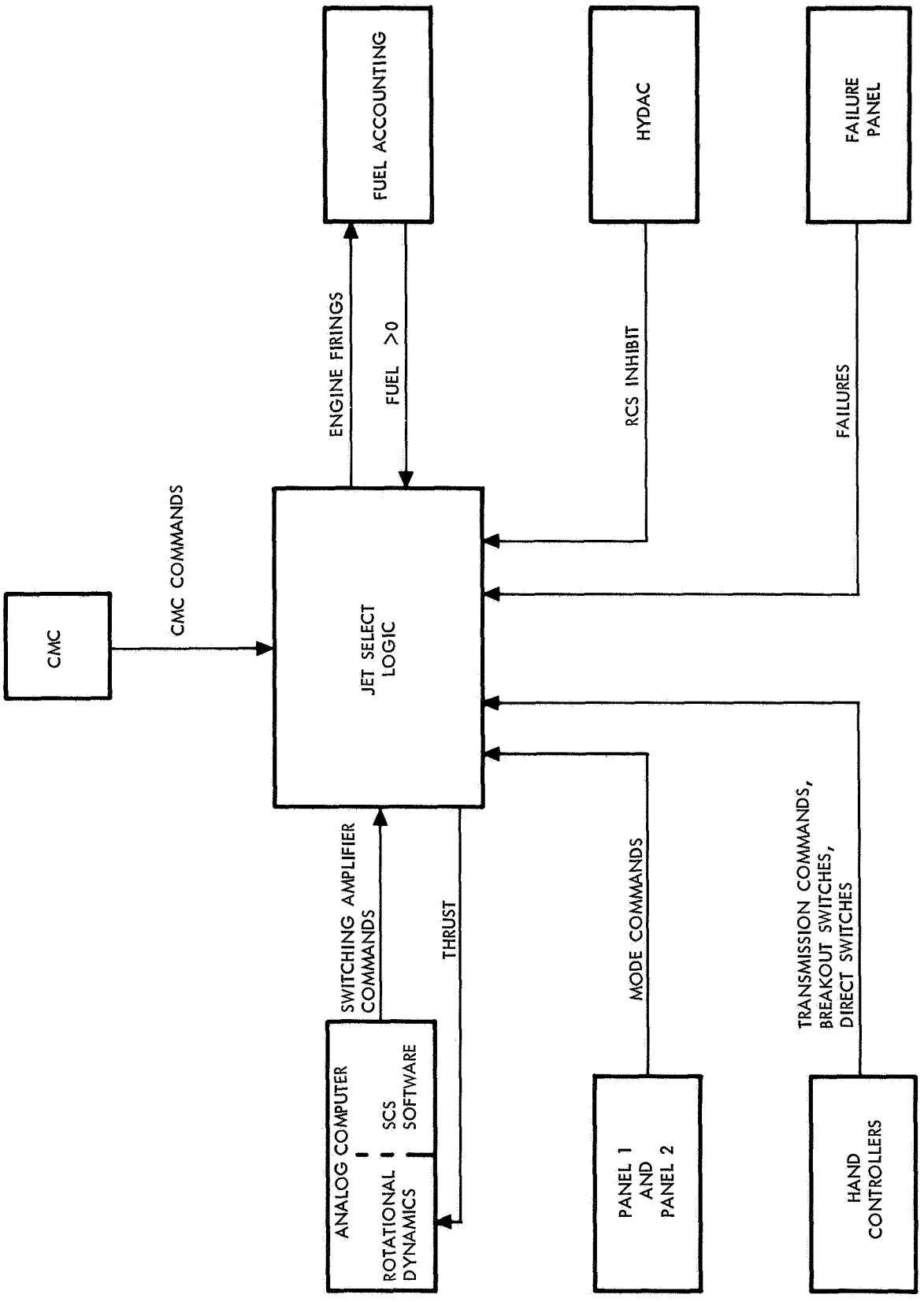

Figure 5-5. Reaction Jet/Electronic Coupler

6 0 SCS PROTOTYPE HARDWARE

Prototype hardware was used whenever feasible, as in the SCS display electronics assembly (DEA), the gyro display coupler (GDC), and switches and displays. This hardware is listed in Table 6-1. Most of it was used in earlier mission evaluation studies and modifications were made to bring it up to the latest specifications. Additional modifications were added in some cases to improve reliability without affecting functional performance.

Table 6-1. SCS Hardware

Name	Serial Number
Gyro display coupler (GDC)*	10028ESH0003
Display electronics assembly (DEA)	10028ESD0003
Rotational controller	10028ESK0004
Translational controller	10028ESL0003
Gimbal position/fuel pressure indicator (GP/FPI)	10028ESJ0006
Attitude set panel (AS/CP)	10028ESP0001
Flight director attitude indicator (FDAI) (2)	10028ESN0002 10028ESN0004

*The GDC operation is modified slightly. The IMU inputs are not transformed in the GDC. The transformations are calculated in the RTSS and the resulting error signals are sent directly to the logic drive of the GDC stepper motors.

7.0 GNCS PROTOTYPE HARDWARE

Prototype hardware was used in the case of the command module computer (CMC), the two display keyboards (DSKY), the interface control panel (ICP), and the electronic coupler display units (ECDU), which include the optical and inertial CDU's. Figure 7-1 shows the optical subsystem and prototype hardware interfacing with the gimbal drive simulator.

The CMC incorporated a tape recorded program in place of core ropes Otherwise, the CMC was representative of the flight hardware.

Modifications were made to the MIT program (Sundisk 281) for utilization in ME-101 simulation. These changes were made to make better use of some of the mission simulator capabilities and obtain results compatible with the system. Table 7-1 lists the locations changed and the values used.

Fixed banks 07 and 40 were altered to allow a warning signal to the SDS 9300 computer when uplink is not being transmitted correctly. This signal is fed back from the CMC to the RTSS after each word in uplink has been sent and its state indicates to the RTSS whether the transmission is satisfactory.

The alteration in bank 05 allows only one identification word marker to be sent per downlink list. The CMC program is written to present a marker for an ID word at word 101-102 in the downlist (the time of CMC clock), and at the initial word of each list. Since downlink stripper electronics were built when the downlist contained only one ID word per 200 words (a full list), a change in the program was necessary.

The celestial sphere used in the simulation complex exhibits the stars according to the 1960 ephemeris data while the star table used in Sundisk 281 is updated to 1968-69. The star unit vectors in bank 13 of the program have been changed to represent a true star position in the star field. These vectors are intended to absorb any positioning error known to exist at a particular star in the celestial sphere.

The locations changed are 13, 3374 to 13, 3731 and the corresponding check sum word in location 3735.

Table 7-1. Changes to Sundisk 282

Bank	Location	Original Value	New Value
05	2745	44260	34260
	2747	03013	05013
	3626	43305	51304
		From:	To:
07	3743	03734	03747
	3745	03734	03747
	3747	03747	34263
	3750	03750	00006
	3751	56435	05011
	3752	Blank	03734
	3753	Blank	03753
	3754	Blank	03754
	3755	Blank	11140
40	3531	00104	00114
	3537	76407	76377
13, 3374 to 13, 3731	1968-69 ephemeris data	1960 ephemeris data + system placement error	

The interconnection of this hardware with other elements of the simulator is illustrated in Figure 1-6.

A description of the sextant shaft and trunnion simulator is presented in this section because of its close relationship to the prototype hardware in the simulator.

The G&N optics (SXT and SCT) are rotated from the optics base by rotating the shaft and trunnion gimbals. However, the sources of visual images are fixed relative to the evaluator so that actual rotation of the gimbals is no longer desirable. The gimbal drive simulator, then, calculates the gimbal rotations which would have occurred and informs the CMC and RTSS of the resulting angles. The RTSS then causes the scene to change just as it would have if the optics had rotated with respect to the real world. Figure 7-1

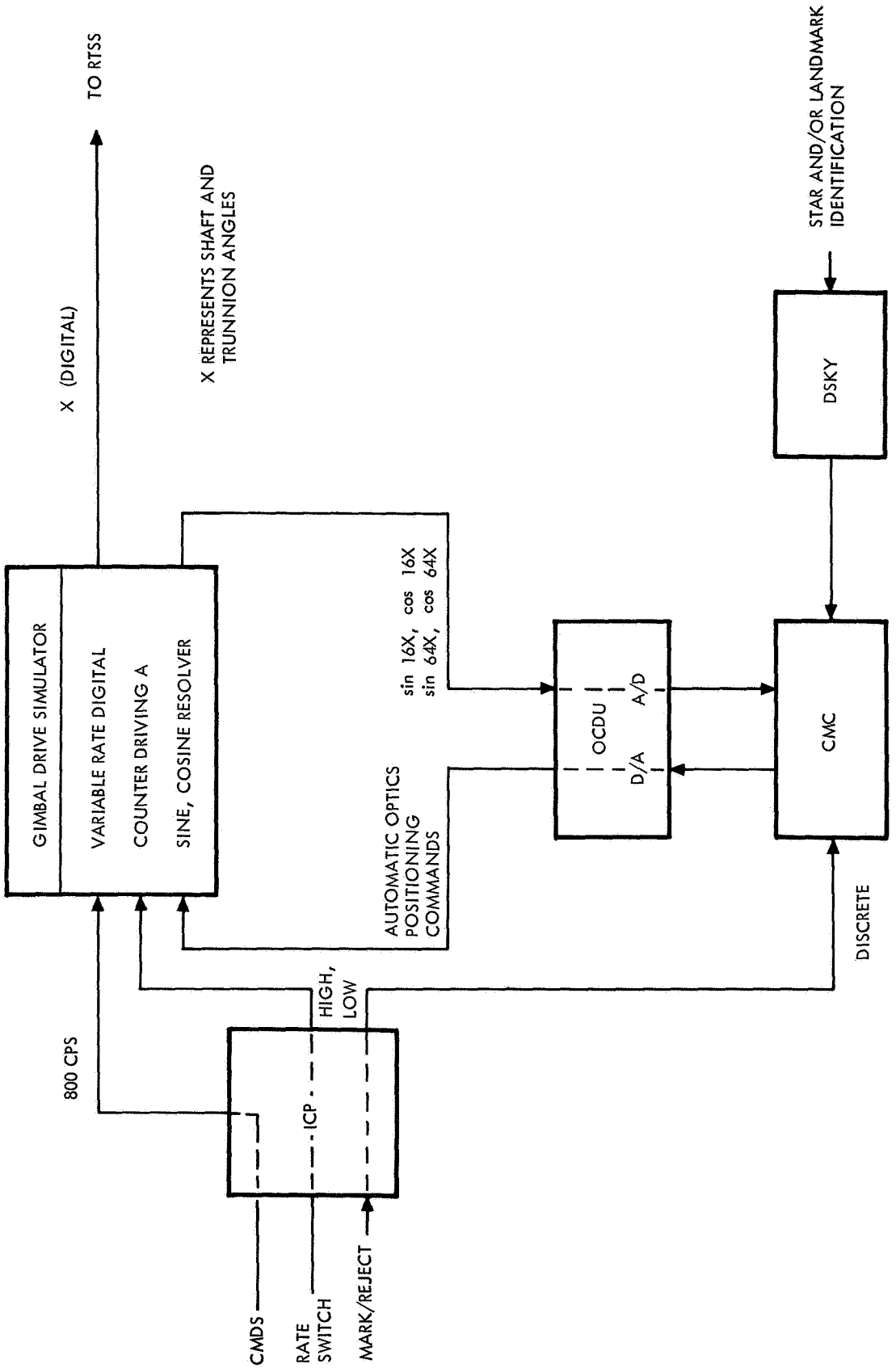

Figure 7-1. Optical Subsystem Diagram Showing Prototype Hardware Interfacing With Gimbal Drive Simulator

is a diagram of the optical subsystem showing the various components of prototype hardware interfacing with the gimbal drive simulator. A list of GNCS hardware is shown in Table 7-2

Table 7-2. GNCS Hardware

Name	Serial Number
OCDU/ICDU (ECDU)	PC-3
ICP	ACSK 3
CMC	5 (Raytheon)
DSKY 1	9
DSKY 2	15

As shown in Figure 7-1, the sextant and SCT shaft and trunnion and associated drive mechanisms have been replaced by an idealized model. No servo dynamics are simulated, positioning is exact within the tolerances of the electronic resolvers, and the SCT and sextant have exactly the same shaft and trunnion angles at all times. The gimbal drive simulator also provides the resolved mode function, which allows the image to be driven with left-right, up-down commands for ease in positioning image.

The optical coupler display units (OCDU), the indicator control panel (ICP), and the command module computer are all prototype hardware items supplied by NASA.

8.0 COMMAND MODULE EVALUATOR

8.1 GENERAL DESCRIPTION OF CONTROLS AND DISPLAYS

The command module evaluator used in the simulation studies consists of a plywood mockup whose interior dimensions and equipment location closely approximate the actual Block II/ME 101 SC configuration. It contains all SC windows with the exception of the hatch window, with out-the-window visual displays and prototype COAS mounting facilities for the left-hand docking window. Two of the three crew couches (commanders and LM pilot) are permanently installed with provisions for installing the center or command module pilot's couch if desired. The couches themselves are similar to the Block I prototype couches suitably modified and mounted to position the astronaut's head and body in both attitude and position to conform to actual Block II/SC 101 configuration. The left-hand or commander's docking window is masked so that, in conjunction with the couch positioning and visual display optical alignment, a properly oriented docking window presentation is obtained. Simulated SC interior lighting is provided in the left- and right-hand couches and the lower equipment bay. The left-hand couch position provides for variable intensity flood lighting for general illumination, variable integral lighting for the two FDAI's, and numerical lighting control for the main DSKY ELS readout. The right-hand couch is provided with variable intensity flood lighting for the LM pilot's position. In the LEB area, both flood lighting for general illumination and numeric lighting for the LEB DSKY are provided.

The main control and display console, which includes Panels 1 through 9, is installed in the evaluator, and all hardware including switches, circuit breakers, meters, valve position indicators, and prototype displays is mounted and mechanically operable. Only those hardware items that have a direct effect on the dynamics of the simulated spacecraft are connected to the simulation, but all switches including those electrically inactive are monitored via a switch position multiplexor to the SDS 9300 computer for recording purposes. All Panel 1 or commander's station switches are active with the exception of those associated with the MESC (1S29 through 1S35 and 1S60, numbers which correspond to the Honeywell switch designation), ELS logic, and command module propellant dump and purge functions. On Panel 2, the active switches include the primary service module RCS propellant isolation valve switches, the service module RCS helium 1 and 2 isolation valve switches, the command module RCS propellant switches, the RCS command ON/OFF, CM/SM transfer switches, and

caution/warning system control switches. All Panel 7 power switches are active with the exception of the EDS power switch. Two of these, namely the FDAI power and the SCS electronics power switch, are used (in the appropriate position) to control the application of power to the prototype EM 3 electronics display assembly and gyro display coupler.

All switches supply power ON/OFF logic signals to the appropriate software areas (analog computer and JSL) to control signal flow in the software systems. Active circuit breakers on Panel 8 include the SCS breakers, SCS logic power, RCS propellant isolation, RCS logic, and SPS gimbal motor control. On Panel 9, the only active switches are the CM/SM separation 1 and 2 switches. The interconnecting wiring between the main display active panels (1, 2, 7, 8, and 9) is such that both dc buses MNA and MNB, and both ac buses AC1 and AC2 are properly routed via the correct circuit breakers, through the power and/or system moding switch to logic, which will ultimately control signal flow paths in the software and prototype hardware areas.

Prototype displays, which are part of the main display console, include the two FDAI's, the gimbal position/fuel pressure indicator, the attitude set control panel, and the Panel 2 main DSKY. Simulated displays include the altimeter, G meter, and LVα/SPS P_c meters driven directly from the analog, and a simulated entry monitor system which consists of a subpanel on which are mounted moding switches, lift vector indicator, and ΔV/range to go numerical display. The G vs V scroll display is simulated by a cathode ray tube which receives its information via video signals from the softwave EMS mechanization. A detailed description of the simulated EMS display is given in Subsection 8.3. For spacecraft manual attitude and translation control, two prototype rotational hand controllers and a translational hand controller are provided.

Equipment installed in the LEB area includes a simulated Panel 100, a prototype G&N indicator control panel, a simulated optical unit assembly with the sextant and telescope eyepieces, and the navigation station DSKY. The simulated Panel 100 contains the controls for LEB flood lighting, integral and numerics lighting for the navigation station DSKY and the IMU, and optical power switches. The prototype G&N indicator supplies minimum impulse controller, optics controller, and other OSS moding signals to the optics subsystem interface. The sextant and telescope eyepieces are used to observe visual display outputs which consist of an oscilloscope presentation of a star and reticle for the sextant, and a composite star field and earth scene for the telescope. The telescope views the dynamic star display combined with the televised dynamic earth display by means of a beam splitter that combines the two images, which are then viewed through a collimating lens to place the virtual image at infinity.

8.2 SIMULATED EMS PANEL AND SCROLL

The prototype EMS was not available for simulation purposes. The simulated panel closely resembled the prototype panel except for slight changes in the internal lighting and appearance of the switches. The major modification was to the scroll assembly. The simulated panel displays the scroll by means of a closed-circuit television view of a scroll chart mounted on an X-Y plotter. The plotter Y axis is driven by the acceleration calculated to exist along the spacecraft X axis ($\ddot{X}_B$) and the plotter X axis is driven by the integral of $\ddot{X}_B$ plus appropriate initial condition. Besides the difference in appearance between the prototype scroll and the cathode-ray tube display, the simulated scroll uses larger numbers to compensate for the decreased television resolution. The plotter pen is also visible. The scroll charts are not consecutive, but must be replaced individually.

APPENDIX
ABBREVIATIONS AND ACRONYMS

A/D	Analog-digital converter
AAI	All attitude indicator
AC	Alternating current
AOH	Apollo Operations Handbook
ARS	Attitude reference system
AS/CP	Attitude set/control panel
ATVC	Automatic thrust vector control
BMAG	Body-mounted attitude gyro
BN	Bending
CDU	Coupler data unit
CEA	Control electronic assembly
CG	Center of gravity
CM	Command module
CMC	Command module computer
CMD	Command
COAS	Crewman's optical alignment sight
CRA	Continuous Recovery Area
CRT	Cathode-ray tube
CTE	Central timing equipment
D/A	Digital-analog converter
D/D	Digital-digital converter
DAP	Digital autopilot
DC	Direct current
DEA	Display electronic assembly
DFG	Diode function generator
DRA	Discrete recovery area
DSKY	Display keyboard
DVM	Digital voltmeter
DWT	Dog wags tail
EAI	Electronic Associates, Inc.
ECA	Electronic control assembly
ECDU	Electronic coupling display unit
EDA	Electronic display assembly
EDS	Emergency detection system

ELS	Earth landing system
EMS	Entry monitor system
ETR	Expected time of recovery
FDAI	Flight director attitude indicator
FPI	Fuel pressure indicator
G&C	Guidance and control
G&N	Guidance and navigation
GA	Gyro assembly
GAO	Gimbal axis origin
GDC	Gyro display coupler
GET	Ground elapsed time
GMT	Greenwich Mean Time
GNCS	Guidance and navigation control system
GP	Gimbal position
GP/FPI	Gimbal position/fuel pressure indicator
GSE	Ground support equipment
HYDAC	Hybrid digital-analog computer
I/F	Interface
IC	Initial condition
ICDU	Inertial coupling display unit
ICP	Indicator control panel
IMU	Inertial measurement unit
IORA	Indian Ocean recovery area
IP	Inertial platform
IRIG	Inertial rate integrating gyro
ISS	Inertial subsystem
JSL	Jet select logic
L/D	Lift-to-drag ratio
LEB	Lower equipment bay
LES	Launch escape system
LOS	Line of sight
LM	Lunar module
LRW	Left rendezvous window
LSB	Least significant bit
LV	Launch vehicle
LVα	Launch vehicle angle of attack
MDC	Main display console
ME	Mission evaluator
MESC	Mission event sequence controller
MGA	Maximum middle gimbal angle

MIC	Memory interface connector
MN	Mach number
MNA	Main bus A
MNB	Main bus B
MPAD	Mission Performance and Analysis Division (NASA)
MSB	Most significant bit
MTVC	Manual thrust vector control
ND	Nondimensional
OCDU	Optical coupling display unit
OSS	Optical subsystem
PAC	Program analyzer console
P_c	Engine chamber pressure
PCM-A	Pulse code modulation—analog
PCM-E	Pulse code modulation—event
PF	Probe focus
PIPA	Pulse-integrating pendulous accelerometer
PLOS	Probe line of sight
PO	Probe offset
PPS	Pulses per second
RCS	Reaction control system
REFSMMAT	Reference stable member matrix (cos(P, I))
RJ/EC	Reaction jet/engine ON-OFF control
RMS	Root mean square
RTSS	Real time simulation system
SC	Spacecraft
SCS	Stabilization and control system
SCT	Scanning telescope
SDS	Scientific Data Systems
SECS	Sequence event control system
SLA	Spacecraft lunar module adapter
SM	Service module
SPS	Service propulsion system
SXT	Sextant
TBD	To be determined
TC	Translation control
TFF	Time to free fall
TFI	Time from ignition
TGO	Time to go
TIG	Time of ignition

TTI	Time to ignition
TVC	Thrust vector control
TVM	Television monitor (coordinate frame)
TVSA	Thrust vector servo amplifier
TWD	Tail wags dog
VG	Velocity gained